5-16-2022

Experimental Characterization and Manufacture of Polymer Nanocomposite Dielectric Coatings for High-Temperature Superconductor Applications

Jacob Ryan Mahon
Rowan University

EXPERIMENTAL CHARACTERIZATION AND MANUFACTURE OF POLYMER NANOCOMPOSITE DIELECTRIC COATINGS FOR HIGH-TEMPERATURE SUPERCONDUCTOR APPLICATIONS

by

Jacob Ryan Mahon

A Thesis

Submitted to the
Department of Mechanical Engineering
College of Engineering
In partial fulfillment of the requirement
For the degree of
Master of Science in Mechanical Engineering
at
Rowan University
April 29, 2022

Thesis Chairs: Wei Xue, Ph.D., Associate Professor, Department of Mechanical Engineering and Robert Krchnavek, Ph.D., P.E., Professor, Department of Electrical and Computer Engineering

Committee Members:
Francis Haas, Ph.D., Assistant Professor, Department of Mechanical Engineering
Behrad Koohbor, Ph.D., Assistant Professor, Department of Mechanical Engineering

Dedications

This thesis is dedicated to my parents, Keith and Cheryl Mahon, for their continuous support in my endeavors. They showed me how to work hard for the things I aspire to achieve and to never give up when things don’t go my way at first.

Acknowledgments

My deepest appreciation goes to my advisor, Dr. Wei Xue, for his extensive support and guidance during my time spent as a graduate student. Working with him has allowed me to find a passion for research and understanding that will follow me for the remainder of my engineering career. Additionally, through his experience and advice, Dr. Robert Krchnavek has allowed me to reach heights in academic research that I previously would have never thought possible.

I would not have reached this point without the community of support I have found over my years spent at Rowan University. I want to thank my friends and fellow graduate students, Nick Pagliocca, Nabil Jamhour, and Kemal Yakut for the memories made during our work in the lab. I also want to thank Chuck Linderman and the engineering support staff who provided their technical insight when I needed help solving mechanical design challenges. Additionally, I want to thank Tanner Coles and Ginger Harnack for their hard work as undergraduate research assistants on this project.

I am grateful to Kristen Lorentzen for always giving me work-life balance, perspective and the continued support I needed throughout this entire process.

Finally, I would like to thank the Naval Surface Warfare Center, Philadelphia Division and the Naval Engineering Education Consortium for supporting this research with the grant number NSWC IHEODTD N00174-17-1-0008. The experts in the Applied Superconductivity Team at NSWCPD were always available and willing provide helpful engineering support when I was in need.

Abstract

Jacob Ryan Mahon
EXPERIMENTAL CHARACTERIZATION AND MANUFACTURE OF POLYMER NANOCOMPOSITE DIELECTRIC COATINGS FOR HIGH-TEMPERATURE SUPERCONDUCTOR APPLICATIONS
2021-2022
Wei Xue, Ph.D. and Robert Krchnavek, Ph.D., P.E.
Master of Science in Mechanical Engineering

Increased implementation of high-temperature superconducting (HTS) power transmission has the potential to revolutionize the efficiency of electrical grids and help unlock a fully electric transportation infrastructure. Realizing the benefits of HTS systems has been impeded by a lack of available dielectric insulation materials that can 1) withstand the extreme cryogenic operating environment of superconductors and 2) demonstrate low temperature processing that is compatible with existing superconductor manufacturing methods. Solving this problem necessitates a high-performance dielectric material with multifunctional properties specifically suited for operation in HTS systems. A polyamide and silicon dioxide (PA/SiO_2) nanocomposite material with exceptional thermal stability has been developed as a solid dielectric coating solution. This study conducts mechanical, thermomechanical, and dielectric characterization efforts that explore multi-scale material property relationships in the nanocomposite to optimize it for this application. Additionally, an experimental manufacturing system is developed to provide a transition to large-scale processing of the nanocomposite coating material. The results of these efforts demonstrate a viable option to solve the material challenges impeding wider implementation of HTS power transmission and chart a path forward for the development of manufactured nanocomposite dielectrics.

Table of Contents

Table of Contents (Continued)

Table of Contents (Continued)

List of Figures

List of Figures (Continued)

List of Figures (Continued)

List of Tables

Chapter 1

Introduction

1.1 Background of High-Temperature Superconductor (HTS) Technologies

The potential for high-temperature superconducting (HTS) power transmission to impact an energy revolution of electric technologies has been compared to the impact fiber optics had on creating information superhighways that transformed communication [1]. Superconductors have the capability to carry current with negligible resistive losses when the superconducting material is operated below a critical temperature, magnetic field, and current density level [2]. In the case of HTS cables, the higher critical temperatures (up to 135 K) allow the use of widely available, efficient cryogenic coolants such as liquid nitrogen (LN_2) and gaseous helium (GHe) [3]. The compact, lightweight, efficient power transmission characteristics offered by HTS technologies have demonstrated 200× higher power/volume capacity with an approximate 10× reduction of transmission cable size and weight compared to standard copper conductor systems [4]. Efficient power transmission has been a key challenge delaying the increased integration of renewable energy technologies into existing energy grids and the development of a fully electric transportation infrastructure. Advanced HTS based transmission systems are a critical component to realizing renewable energy-based technologies as mitigating the detrimental impacts of CO_2 emission from existing technology becomes necessary for our future [5].

1.1.1 Applications of HTS Power Transmission Systems

The negligible electrical resistance of high-temperature superconductor materials cooled to cryogenic temperatures has revolutionary applications in both alternating current (AC) and direct current (DC) power transmission systems. In order to meet the needs of an economical and stable energy infrastructure in heavily populated areas, recent projects have investigated high current density transmission with three-phase AC HTS cables cooled by pressurized liquid nitrogen in the temperature range of 65 K - 77 K [6-8]. These AC cable systems require sophisticated terminations that mate phase conductors and dielectric layers from room temperature feedthroughs with the LN_2-cooled cryostat in a high-voltage environment, along with an array of refrigeration equipment including cryocoolers, mixing tanks, pumps, and an LN_2 storage tank [3]. Figure 1A shows one such HTS transmission termination installed by the Long Island Power Authority (LIPA) [9].

HTS cable systems also have excellent characteristics for DC current transmission in electric transportation applications [10]. Superconducting power transmission is a key element to realizing the development of machines and systems contained in all-electric aircraft [11]. Due to the weight and volume of conventional electric propulsion motors, generators, and power transmission systems, exceptional flight performance is not possible without the development of high power density superconducting technology [12]. Shown in Figure 1B, the turboelectric distributed propulsion system in the NASA N3-X concept aircraft can potentially achieve a 70% fuel burn reduction, performing power transmission via onboard superconducting cables and cryogenic power inverters [11, 13]. The same value is given to the weight and space savings of superconducting

machines onboard electric transport ships and naval vessels. Shown in Figure 1C, the world's first electric and self-propelled container ship, Yara Birkeland, recently departed for its maiden voyage and is proposed to cut 1,000 tonnes of CO_2 emissions and 40,000 trips by diesel powered trucks per year in Norway [14]. In addition, the U.S. Navy has found HTS cables on its vessels to be an appealing option for minimizing weight and mitigating operational losses in onboard power transmission. Recent developments in an advanced three-axis degaussing system for increased magnetic signature reduction of vessels provided a suitable opportunity for the development and testing of an HTS cable system, where system weight was reduced by 80% compared to copper conductors [15, 16].

Figure 1

Applications of HTS Power Transmission

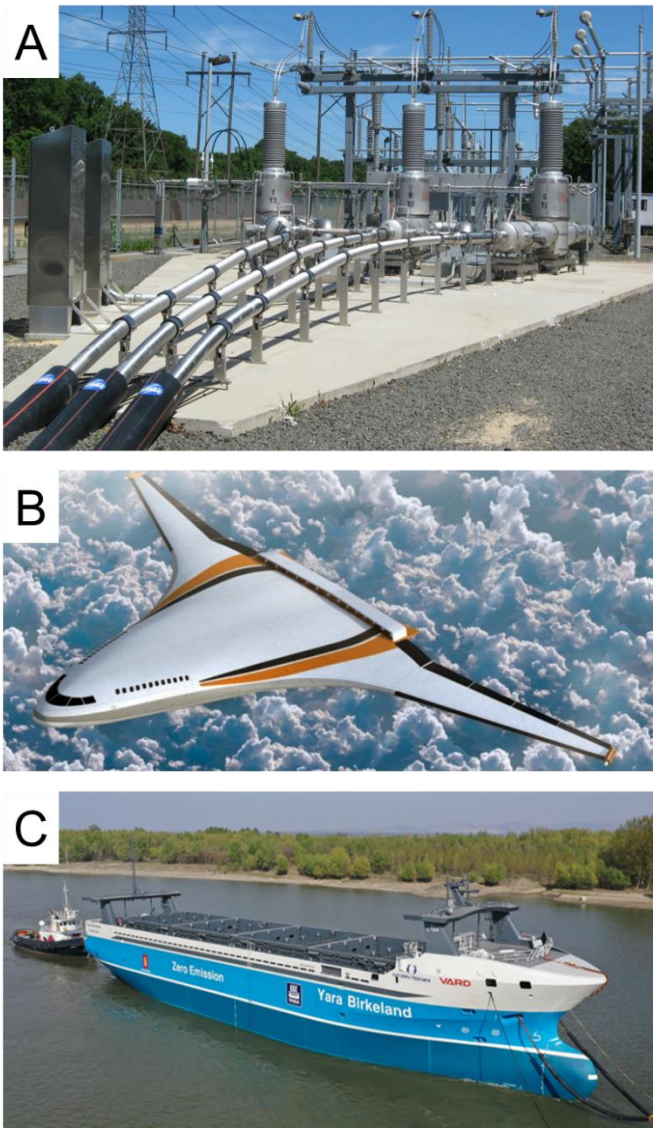

Note. Various applications of HTS power transmission systems. (A) HTS transmission termination in power grid [9]. (B) NASA N3-X concept electric aircraft [11]. (C) Yara Birkeland electric container ship [14].

1.1.2 HTS Power Transmission System Design Considerations

In most HTS power transmission applications, the current carrying layers in cables are comprised of wound superconducting tapes, which are fabricated through multistep processing operations, where superconducting films are mechanically formed or deposited on flexible metal substrates and laminated between buffer layers [17]. Shown in Figure 2A, Second Generation high temperature superconducting (2G HTS) tape is now the most frequently used commercial superconductor in high field magnets, motors, and transmission cables due to the improved mechanical properties and the reduced costs of manufacturing [18, 19]. In order to achieve the superconducting temperature state in cables, HTS tapes are cooled in a cryostat envelope to thermally isolate the HTS cable from the ambient environment [20-22]. The typical construction of a flexible cable cryostat consists of multiple concentric, corrugated, stainless steel tubes, where the annular region between the outermost tubes contains both vacuum and multilayer insulation (MLI) systems to minimize thermal heat loads on the cryogenic refrigeration system [21].

The refrigeration system circulates cryogenic coolants such as liquid nitrogen or helium gas into the former core, then returns them through the cryostat annulus on the superconductor surface [20]. Figure 2B shows laminated HTS tapes within a multi-phase AC HTS cable structure, where individual tape phase layers are wound around a central former and insulated from other phases by dielectric layers in a triaxial configuration. A superconducting shield layer is wound on the outermost layer of the cable conductors, where it serves to prevent the increase of AC loss due to magnetic fields when individual phase conductors interact with one another [23]. The dielectric insulation layers in this

configuration are a critical design point, as the mechanical, electrical, and thermal characteristics of these insulating materials can have a significant influence on the performance and stability of the superconductors [24-26].

Figure 2

HTS Transmission Cable Construction

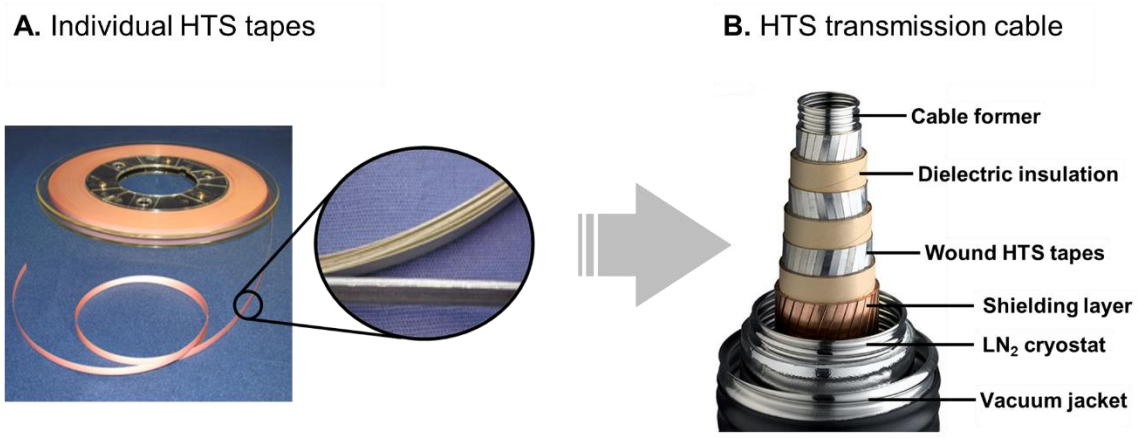

Note. (A) Second Generation high temperature superconducting (2G HTS) tape [27]. (B) Nexans three-phase AC HTS transmission cable [28].

The development of HTS materials made cryogenic cooling via inexpensive, widely available LN_2 cooling possible and dramatically influenced the development of many current superconductor applications [1]. However, the use of gaseous helium as a cryogenic coolant in HTS transmission cables has proven to be advantageous to the traditional LN_2 coolant [16, 29]. Basic driving forces behind HTS cable design include maximizing the current density of conductors, while limiting the resulting weight and

footprint of cable systems. Since the critical current of a superconductor is temperature dependent, using helium gas to cool superconductors to lower temperatures than the 63 K limit of liquid nitrogen systems can yield significantly greater power densities in the cable format [4, 30]. A typical commercial 2G HTS conductor operating at 20 K can carry six to eight times the current it can carry at 77 K [3]. The wider cooling temperature range of gas helium also benefits some military applications, where compact and lightweight power devices that offer a wide operating current density window are required [30]. Optimizing the relationship between the increased power requirements of a gas helium cryogenic refrigeration system at sub-62 K temperatures and the resulting increases in current density has found that the operating temperature to minimize both cable system weight and cost is roughly 50 K, where current density values are still threefold of those at 77 K [3, 15]. At a fixed current carrying value, this directly results in increases in efficiency and a reduction of cable system footprint. In addition to the limitations associated with the minimum cooling temperature, another major drawback associated with LN_2-cooling stems from the asphyxiation hazards related to its use in confined spaces, making it unfavorable for naval and aviation applications where a leak of lower density gaseous helium coolant would be significantly safer to personnel [16, 29].

1.1.3 Material Challenges Associated with Existing HTS System Design

The demand has increased for high-performance polymer dielectric materials with enhanced mechanical properties suited to the extreme operating environments required by superconductors [25, 31, 32]. The thermal contraction of a typical polymer insulation material that occurs due to the intense temperature gradient of the superconductor's cool

down cycle is significant, leading to mechanical failure and high-voltage electrical shorts at cryogenic temperatures [18, 33]. Figure 3 shows how the mismatch of cryogenic thermal contraction between the dielectric coating and superconductor material is the responsible mechanism for failure of the dielectric layer. To address this, LN_2-cooled HTS tapes and cable assemblies traditionally utilize lapped polymer tape dielectric layers of thermally stable materials such as Kapton™ polyimide or polypropylene laminated paper (PPLP) [34-36]. The lapped tape construction effectively reduces the failure of brittle polymers at cryogenic temperatures by increasing their degrees of freedom inside a dielectric jacket [20]. However, these systems are then required to permit the permeation of the cryogenic coolant into the insulation jacket around superconductors, allowing them to become part of the dielectric media.

Figure 3

Thermal Contraction in the Cryogenic Environment

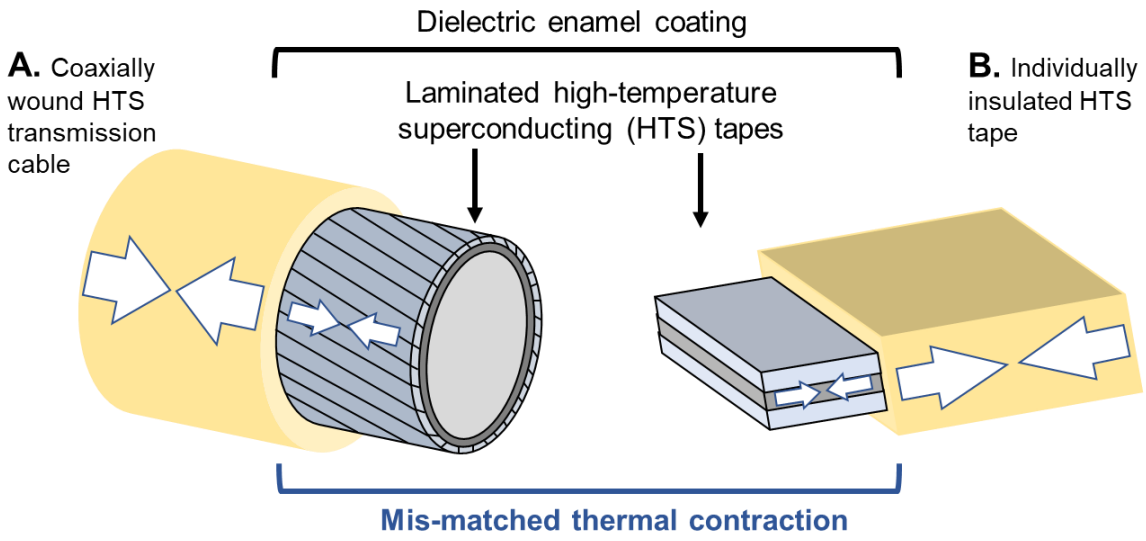

Note. The responsible failure mechanism for brittle dielectric coatings at cryogenic operating temperatures is a mis-matched coefficient of thermal expansion (CTE) between superconductor and dielectric materials.

Realizing the benefits that result from implementing gas helium cooling in HTS cables presents additional challenges in locating effective dielectric insulation materials and systems for the sub-62 K cryogenic environment. LN_2 cooling has been used cost effectively and generally without concern, because the relatively high dielectric strength of the fluid obstructs shorts through the cryostat, even at high voltages [29, 37]. However, when helium gas is introduced as coolant, its significantly lower dielectric strength does not permit permeation into existing dielectric tape jackets without risking shorts through the fluid from superconductors at high voltages [29, 30, 38]. A gas tight, solid dielectric

insulation layer is not only required for GHe-cooled systems, but would be preferred for LN_2-cooled systems as well. Bubble-trigged partial discharges, degradation, and complete dielectric breakdown in cryogenic liquids has been reported due to quenching from hot spots on conductor manufacturing imperfections or void spaces at liquid-solid dielectric layer interfaces [35, 37, 39]. In addition, failures of superconducting coils have previously been attributed to the contamination of the cryogenic liquid insulation space with conductive free metallic particles [39].

Therefore, the need exists for a suitable dielectric in the cryogenic operating environment that envelops conductive layers, while sealing against liquid and gas coolant permeation. Advanced materials such as Kapton™ polyimide possess coefficient of thermal expansion (CTE) values that closely match metallic and ceramic superconductors during cooling cycles and have been implemented as dielectric enamel coatings [40, 41]. However, despite their widespread use as a dielectric solution for the aerospace industry, these materials are not a catch-all for the variety of potential dielectric requirements associated with superconductor technologies. For instance, existing manufacturing techniques produce superconductor materials that are vulnerable to degradation or failure from excessive mechanical and thermal stresses during processing [18]. To enable wider implementation of superconducting power systems, polymer dielectrics must be identified that not only show exceptional thermomechanical behaviors in the cryogenic environment, but also have processing methods that are compatible with superconductor manufacturing practices [42, 43]. Accordingly, a detailed study of the potential dielectric thin film coatings for these applications is required, with a variety of experimental

methods to effectively characterize their thermomechanical and dielectric behaviors in the superconductor's operating environment.

1.2 Polymer Nanocomposites as High-Performance Dielectric Coating Materials

Polymer nanocomposite materials are an area of great significance due to the role of nanoparticle addition in improving one or more desired properties of a host material [44-47]. These materials have received renewed interest because when combined with modern material characterization and synthesis tools, long established nanoparticle preparation methods can be leveraged to engineer novel combinations of polymer hosts and reinforcement materials with resulting properties that are highly tunable [44]. Polymer nanocomposites can open new horizons for achieving multifunctional materials by choosing, arranging, and combining nanostructured components tailored for a specific application [48].

1.2.1 Nanomaterials as a Field of Interest for Coatings in Extreme Applications

The capacity for nanocomposites to make considerable improvements to a wide range of physical properties in host polymers gives them potentially limitless applications. Nanofiller reinforced materials have proven to be a viable option for applications requiring rugged polymeric coatings [49, 50]. For instance, epoxy coatings can act as a physical barrier and as a reservoir for corrosion inhibitors, reducing the corrosion of a metallic substrate subject to an electrolyte [49]. However, these effects can be undermined by their susceptibility to damage by surface abrasion and poor resistance to the initiation and propagation of cracks [49]. The incorporation of nanoparticles into

epoxy resins offers solutions to enhancing the integrity and durability of these coatings [51, 52].

Polymer nanocomposite materials have also found applications in capacitors and electric energy storage devices [53-56]. When brittle ferroelectric ceramics with high dielectric constant were combined with flexible polymers of low processing temperature, a high dielectric constant and breakdown field was achieved with improved volume efficiency and energy storage density [53-56]. These are highly desired properties of materials predisposed for applications in microelectronics and high-voltage industries. In addition, it was shown that the properties of the nanocomposites, i.e., transmittance, elastic modulus, response time, and dielectric constant, could be tuned by controlling the nanoparticle weight percent concentration [55]. This characteristic provides yet another degree of material property tuning for desired applications. With this array of possibilities, multifunctional materials can also potentially be leveraged to address the specific needs of high-temperature superconductor technologies.

1.2.2 Addressing Cryogenic Dielectric Material Challenges in HTS Systems with Polyamide/Silica Nanocomposite Thin Films

In the case of studying potential dielectric thin film coatings for applications in HTS power transmission, the purpose of investigating the use of functionalized nanoparticles is to influence and gain control over the CTE of the resulting nanocomposite material. In addition to this, a primary design requirement is that the processing of the nanocomposite dielectric coating material must be compatible with the manufacturing parameters used to develop 2G HTS tapes found in both individually insulated applications and in the coaxially oriented cable format. Epoxy resins have

previously been used in cryogenic systems such as superconducting magnets or cryogenic valve and tank applications [33, 42, 57]. However, the relatively large CTE that results in thermal stress at cryogenic temperatures limits their use as a cryogenic dielectric coating. One approach to improving CTE characteristics is tailoring the chemical and network structures of epoxy resins, but it is not so effective due to the intrinsic properties of polymer [57]. The alternative option of introducing lower CTE nanofiller particles into the polymer matrix has been widely demonstrated to improve the thermomechanical properties of the nanocomposite material [57-60]. Therefore, this technique demonstrates a solution that can potentially reduce the mismatch of cryogenic thermal contraction between dielectric coatings and superconductor materials, eliminating failures of solid insulation materials in HTS applications.

The unique thermal, physical, and electrical properties of polyamide-imide based materials has enabled them to become outstanding candidates for electrical insulation applications in extreme operating environments [60-62]. Thus, this class of polymers was located as the focus of multifunctional material development and characterization for a study of potential HTS dielectric coatings. Investigating various nanocomposite preparation methods for ease of processing, reliability, and compatibility with the manufacturing process of HTS tape products identified silica nanofiller reinforcement via sol-gel process as a potential path to a multifunctional dielectric material for this application [59, 63, 64]. Introducing silica nanoparticles with a lower CTE than the polyimide-based host and a relatively high dielectric strength into the polymer matrix opens the potential for improved thermomechanical properties of the insulation material, while maintaining acceptable dielectric strength [60, 65].

A polyamide and silicon dioxide (PA/SiO_2) nanocomposite is therefore proposed here as a viable option for a polymer insulation coating of high temperature superconductors with desired CTE matching characteristics. This solution addresses the concerns associated with dielectric failures of LN_2 and GHe cryogenic envelopes, while improving upon the poor cryogenic mechanical properties associated with traditional polymer coatings. The proposed dielectric nanocomposite material has the potential to address the multifunctional design requirements of cryogenic gas helium and liquid nitrogen cooled HTS power transmission systems, reducing failures of solid insulation layers and improving transmission performance.

1.3 Research Motivation and Objectives

As the necessity grows for clean, abundant, and reliable sources of electricity that will sustain economic growth into the future, the obligation for new ways to transmit and distribute electricity is increasing [1]. Using high-temperature superconducting systems to revolutionize the efficiency of power transmission can solve major energy conversion and distribution challenges that are currently plaguing the integration of renewable energy technologies into existing energy grids [4]. In addition, HTS power transmission is a key component to developing fully electric transportation modes and supporting infrastructures that perform better than fossil fuel-based systems, while eliminating sources of CO_2 emissions [5]. However, realizing these benefits comes with the need to address a variety of material challenges associated with existing HTS technologies, specifically with the fragility of thin film dielectric coatings in cryogenic cooled operating environments [25, 31, 33, 42, 66]. Upon solving these challenges, larger steps

can be taken towards implementing HTS power transmission systems in many of these critical applications.

To reduce the failures of existing HTS power systems and dramatically improve their transmission efficiencies through gas helium cooling techniques, the opportunity exists for the development of a multifunctional cryogenic dielectric suited to this unique application. A polyamide and silicon dioxide (PA/SiO_2) nanocomposite material has been proposed as a solid dielectric coating with improved resistance to thermal contraction and reduced mechanical stress in the cryogenic operating environment of HTS transmission cables. Therefore, a detailed characterization of the mechanical, thermomechanical, and dielectric properties of this candidate material is required to verify its theoretical properties, where a combination of experimental and computational methods are used. Accordingly, a variety of novel and fully customized experimental test systems must be designed, manufactured, and implemented in order to effectively depict the material behavior in the superconductor's operating environment. Establishing these tunable property relationships will result in the optimization of the weight percent concentration of silica nanoparticles required to achieve the desired final material properties. In addition, material processing and manufacturing methodologies must be established that are 1) compatible with existing HTS transmission system manufacturing and 2) scalable from test sample preparation up to full scale cable coating manufacturing systems. Ideally, the results of these characterization analyses and processing development efforts will produce a promising solution to providing effective dielectric materials for GHe and LN_2-cooled HTS cables with enhanced mechanical properties suited to their extreme operating environment.

1.4 Layout of Thesis

The next chapter of this study will detail the thermomechanical and dielectric characteristics of polymer nanocomposite materials used for rugged coatings in extreme applications. The selection of the specific polyamide host polymer for this application and its SiO_2 filler nanoparticles will be explained, along with a justification for the implementation of a nanocomposite in this application versus other options in the realm of multifunctional materials. Finally, the methods of sample preparation and coating process conceptualization will be covered. Chapter 3 of this study will describe the computational and experimental methods used to characterize the mechanical and thermomechanical properties of the polymer nanocomposite material. Then, the results will be analyzed to establish an understanding of these property relationships, unlocking the ability to optimize the material for implementation in the cryogenic operating environment.

Chapter 4 will contain details of various dielectric material property characterization efforts. Investigating these results will determine the dependence of the material's dielectric strength on its operating temperature. In addition, experimental testing conducted in a cryogenic gas helium environment will shed light on the impact of this potential HTS cooling medium on the dielectric strength of coatings. Finally, experimental methods will also be used to examine the changes in dielectric strength of the material that may occur due to it being coated in on a cylindrical conductor surface, rather than in planar coated thin film forms. Chapter 5 will report on the design considerations and experimental manufacturing efforts towards developing a feasible transition to large scale processing of this material. Lastly, Chapter 6 will conclude the

results of the various characterization efforts conducted here and combine them with the experimental manufacturing efforts. The chapter will provide this polymer nanocomposite as a solution for an effective cryogenic dielectric material and discuss the opportunity for additional future works in this study.

Chapter 2

Selection and Preparation of Nanocomposite Dielectric Materials

2.1 Background of Polyamide/Silica Nanocomposite Dielectric Materials

The HTS dielectric insulation system developed here must 1) effectively seal against permeation from cryogenic cooling fluids during operation, 2) show an improved dimensional stability during thermal loading that reduces the mismatch of CTE between different cable materials, 3) exhibit material processing characteristics that are compatible with superconductor manufacturing methods, and 4) maintain sufficient dielectric strength for use in high-voltage applications. The unique combination of properties required for the potential coated insulation materials to be functional in the extreme cryogenic operating environment of HTS systems and compatible with HTS tape manufacturing necessitates a larger degree of material property tuning than most traditional polymer coatings can offer. This study will leverage the characteristics of polymer nanocomposites that enable them to be engineered for highly specific resulting properties [67, 68]. When nanoscale filler materials with desired properties are added to a traditional polymer, their interfacial interaction zones with the polymer can dramatically influence the thermal, mechanical, and electrical properties of the composite on the macroscopic level [68-70]. Because of this, recent studies have capitalized on the promising advantages of nanodielectric materials in the area of electrical insulation [67, 71]. Specifically for this application, SiO_2 nanofillers in polyamide-based coatings have been shown to generate a low CTE and high thermal stability for the bulk material [58-60].

2.1.1 Locating the Polyamide Host Polymer

Due to their strong interchain interactions, aromatic polyimides are an exceptional class of high-performance polymers with thermomechanical stability, dielectric strength, solvent resistance, and high mechanical strength [40, 72]. Figure 4 graphs the linear thermal expansion of various materials used in HTS cable construction and highlights the thermomechanical failure mechanisms of common dielectric coatings caused by a mismatch of CTE with a dissimilar substrate material [73]. Polyimide is one of the only available dielectric materials that nearly matches the CTE of the 300 series stainless steels employed in hollow tube cable formers and the Bi-2223 Bismuth strontium calcium copper oxide (BSCCO) superconductors used in first generation powder-in-tube (PIT) HTS tapes [3]. Polyimide enamels with uniquely low CTE values have been used for rugged, heat-resistant dielectric coatings in the aerospace industry, but their poor solubility and non-melting characteristics make processing operations difficult [72, 74].

Figure 4

Thermal Expansion of Solids for HTS

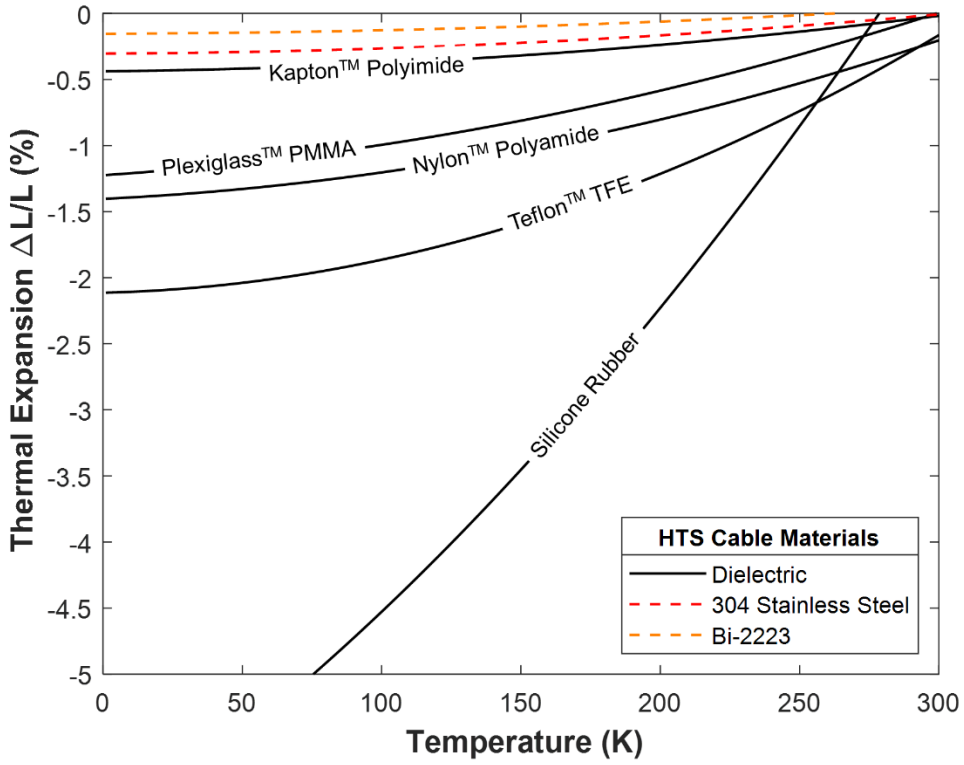

Note. Thermal linear expansion percentage of common dielectric polymers in comparison to HTS tape and HTS cable construction materials. Thermal expansion data are selected from [73].

Ideally, the desirable properties of polyimide could be leveraged for the cryogenic applications in HTS cable systems, but the imidization reaction and thermal annealing processes require temperatures far greater than 200 °C and HTS tapes become vulnerable to delamination from excessive thermal stresses during processing temperatures greater than roughly 150 °C [3, 18, 42]. Therefore, achieving the low temperature curing of a

polyamic acid solution to generate aromatic polyamide enamels without high-temperature processing became a focal point in this study. To answer this problem, Dupont Pyre-M.L.® thermoset varnish was located as a commercial polyamic acid (PAA) precursor to polyimide enamel coatings that could potentially be cured at lower temperatures, without the need for the thermal imidization and annealing steps [41, 74]. The Pyre-M.L.® poly(pyromellitic dianhydride-co-4,4′-oxydianiline) amic acid was acquired in solution with 80% N-Methylpyrrolidone (NMP) and 20% aromatic hydrocarbon [75]. Following solvent evaporation and thermal curing below 150 °C, the resulting thin film displays equivalent properties to the Nylon^{TM} polyamide curve plotted in Figure 4 [72, 73, 76]. By achieving the desired low temperature processing, some of the exceptional thermal stability of the polyimide is sacrificed. Therefore, a truly multifunctional composite material using a dissimilar filler is needed to optimize the thermomechanical and dielectric properties for applications in HTS systems.

2.1.2 Achieving Desired Properties with Polyamide/Silica Nanocomposites

Nearly all commercial examples of polymer-based nanocomposites to date have revolved around introducing nanoscale fillers into polymers and capitalizing on the effect of filler properties to enhance performance of the composites [42, 77, 78]. Matrices of lower CTE nanoparticle reinforcement are used to improve the thermal stability of polymer nanocomposites and introducing SiO_2 particles has repeatedly been demonstrated as an effective path to accomplishing this [76, 79-83]. The wide reporting and reliability of the in-situ sol-gel processing methods used to develop SiO_2 matrices are critical for this application, since large scale processing of multifunctional materials is often already difficult without the additional need to ensure compatibility with HTS tape

manufacturing systems [84, 85]. Specific to this proposed PA/SiO_2 dielectric application, the relatively high CTE of pure polyamide (80×10^{-6} K^{-1}) has the opportunity to be significantly reduced by that of the SiO_2 nanoparticles (2.32×10^{-6} K^{-1}) and crucially, they both demonstrate comparable dielectric strengths as insulators in various applications [73, 80, 86, 87]. It is widely accepted that introducing any defects including nanoparticles of dissimilar materials into a bulk polymer can negatively impact the resulting dielectric strength [48, 67]. However, the comparable dielectric strength of SiO_2 nanoparticles with polyamide and the role of nanoscale interfacial regions in avoiding unfavorable changes to bulk polymer properties can potentially reduce negative impacts to the overall dielectric strength of the nanocomposite [67, 88, 89].

The dramatic macroscale property changes of nanoscale reinforced polymer composites result from the formation of a radial interphase region of higher density polymer formed in the vicinity of individual particles [90, 91]. Microscale silica particle composites, which also benefit from the interfacial interactions of the filler material, have been widely employed in commercial coatings such as Loctite Stycast® high-viscosity encapsulant, which is filled with silica powder to provide a low thermal expansion that approaches that of copper [73, 78, 92]. However, when silica particles are introduced at the nanoscale, the same volume of filler broken into smaller particles creates a higher radius of curvature, greater surface area for polymer interaction, and therefore, more polymer in the interfacial region within the bulk material [93]. These increases in interfacial polymer volume resulting from decreases in particle diameter are demonstrated in Figure 5. The interfacial region surrounding the particles is dominant in a nanocomposite, whereas it is insignificant for the conventional microcomposite [67].

Due to this increased control over the bulk mechanical properties of a polymer, significantly larger property improvements can be made at lower concentrations of reinforcement material and greater property tuning characteristics are achieved [67, 90, 94]. This particle diameter relationship becomes increasingly significant in this dielectric application, because the desired thermomechanical characteristics can be achieved at lower SiO_2 nanoparticle concentrations, with smaller defects in the bulk material and larger regions of dense polymer, potentially resulting in smaller impacts on the overall dielectric strength. Therefore, the proposed PA/SiO_2 nanocomposite dielectric material addresses each of the challenges imposed by its implementation as a dielectric coating in HTS systems and warrants further investigation to experimentally characterize the material in this study.

2.1.3 Polymer Nanocomposite Interfacial Morphology

The mechanisms of the interaction zones located between nanoparticle reinforcement materials and the host polymer are highly complex. Polymer chains can be mechanically bound in immobile layers and/or chemically bonded to the nanoparticle in this region, depending on particle diameter, interparticle distances, and materials selected [67, 93]. The volume of the interfacial region and the mechanisms behind the densely constrained polymer chains within can directly impact the resulting mechanical and dielectric properties of the bulk system [95-98]. Due to changes in the crystalline structure of polyamide near interfaces within the PA/SiO_2 nanocomposites, polyamide chains are considered to be radially bonded to the nanoparticle surface within a larger multi-core model of the interfacial region [67, 68, 99, 100]. Figure 5 shows the proposed multi-core and barrier model of the dense polyamide interfacial region. Polymer chains

are bonded to the surface of the SiO_2 particle, then immobilized in an orderly bound space due to crystalline properties of the polymer, and finally loosely constrained in an outer region that is coupled with the second layer [99, 100]. The morphology of the interphase region is also proposed to enable a superimposed electrical double-layer. This double-layer is formed due to the distribution of mobile charge carriers and the existence of electron traps throughout the interphase [67, 101]. This decreases the density and energy of carriers as well as their conductivity, resulting in a localized enhancement of electrical breakdown strength [67, 101]. Therefore, the interfacial morphology of PA/SiO_2 nanocomposites demonstrate characteristics that not only support confinement of the polymer to reduce the CTE of the matrix, but also potentially prevent excessive reduction of dielectric breakdown strength at larger concentrations of SiO_2 particles.

Figure 5

Morphology of Particle-Polymer Interfacial Regions in Nanocomposites

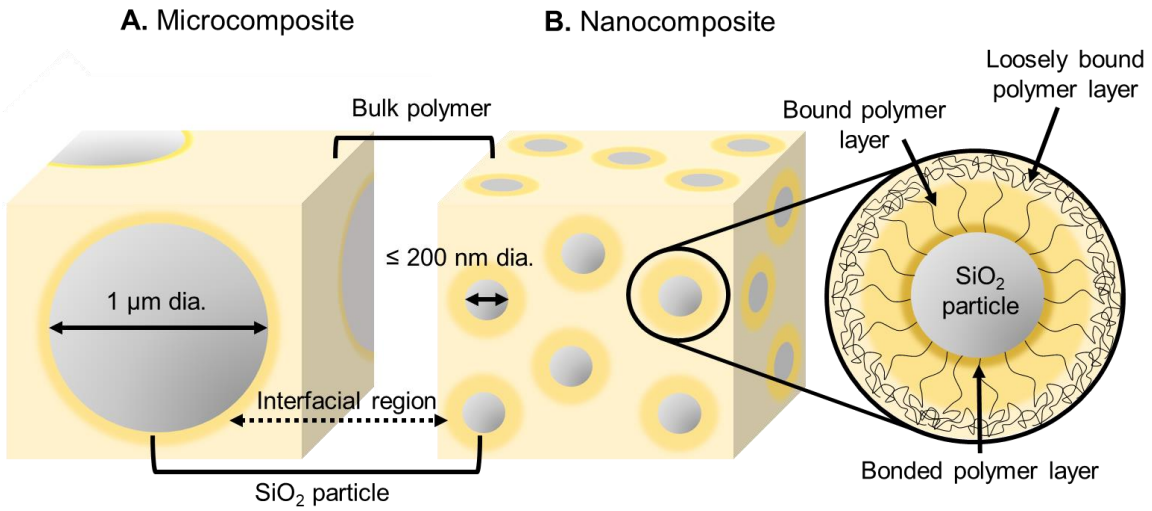

Note. Comparison of PA/SiO_2 particle-polymer interfacial regions between a microscale composite (A) and a nanoscale composite (B). The structure of polyamide chains in the interfacial regions of silica nanoparticles reported by [49, 67, 93, 99, 102] is detailed at the right.

2.2 Methods of Preparing Polyamide/Silica Nanocomposite Materials

Dip-coating is a basic manufacturing method of choice to accomplish thin film deposition and curing of the nanocomposite dielectric material on the flat surface substrates of individual HTS tapes, as well as on the cylindrical surfaces of formed HTS cable assemblies. In addition, free standing thin film samples must be developed by spin coating glass slides to enable thermomechanical and dielectric characterization experiments. To accomplish this, a PA/SiO_2 nanocomposite precursor solution must be

prepared in a such a way that it remains homogeneously dispersed in the fluid medium during processing and avoids macroscopic gelation that would hinder the repeatable preparation of samples [103]. Following the coating of a substrate with the precursor solution, solvent evaporation and thermal curing steps must yield a solid dielectric enamel without exceeding the 150 °C temperature threshold where delamination of 2G HTS tapes can occur [3, 18, 42].

2.2.1 Implementing a Sol-Gel Process

Sol-gel methods are a well explored path to synthesizing composite organic-inorganic materials made at relatively low temperatures, through which hydrolysis of the constituent molecular precursors and subsequent polycondensation lead to a glass-like form [89]. The Stöber process is regarded as the simplest and most effective route to prepare monodisperse silica nanospheres inside of a polymer solution [84, 104]. The process, which has been widely used to develop catalysts, pigments, pharmaceuticals, and coatings for electronics, can be easily modified to suit the industrial manufacturing of PA/SiO_2 dielectric coatings for superconductors [85, 89]. This study successfully leverages the Stöber process to obtain well dispersed colloidal silica nanoparticles that are mixed with a polyamide precursor solution and cured to prepare PA/SiO_2 thin films.

The generation of SiO_2 nanoparticles in the Stöber process hinges on the hydrolysis and condensation reactions of a silicon alkoxide in the presence of water, which provides the solution of precursors with the necessary supersaturation for the development of particles in suspension [105, 106]. The process also employs an alcohol solvent to improve the miscibility of the sol-gel system and incorporates an acid catalyst

for the hydrolysis reaction [106, 107]. The Stöber precursors utilized in this work were tetraethyl orthosilicate (TEOS), deionized water (DI water), ethanol (EtOH), and hydrochloric acid (HCl). The sol-gel is created by mixing the four reagents in a 2:1:1:1 molar ratio of DI water, TEOS, EtOH, and HCl [106, 108]. The precursors are mixed at 300 RPM for 30 minutes, covered with paraffin film and placed in an ice bath to mitigate evaporation of any precursor mass due to the exothermic reaction. As detailed in Figure 6, the formed sol-gel suspension of nano-silica is then mixed into the Pyre M.L.® polyamic acid precursor solution for 4 hours at 30 RPM to enable effective particle dispersion without causing air bubbles to form in the viscous material. Finally, the viscous PAA and sol-gel suspension is spin coated onto glass slide substrates for free standing thin film samples or dip-coated onto stainless steel electrode substrates for on-cable dielectric performance measurements. Various experiments were conducted by previous contributors to this study in developing the mixing times and methods utilized for the polyamide nanocomposite suspension preparation, with the results detailed here [108].

Figure 6

Preparation of PA/SiO_2 Nanocomposites

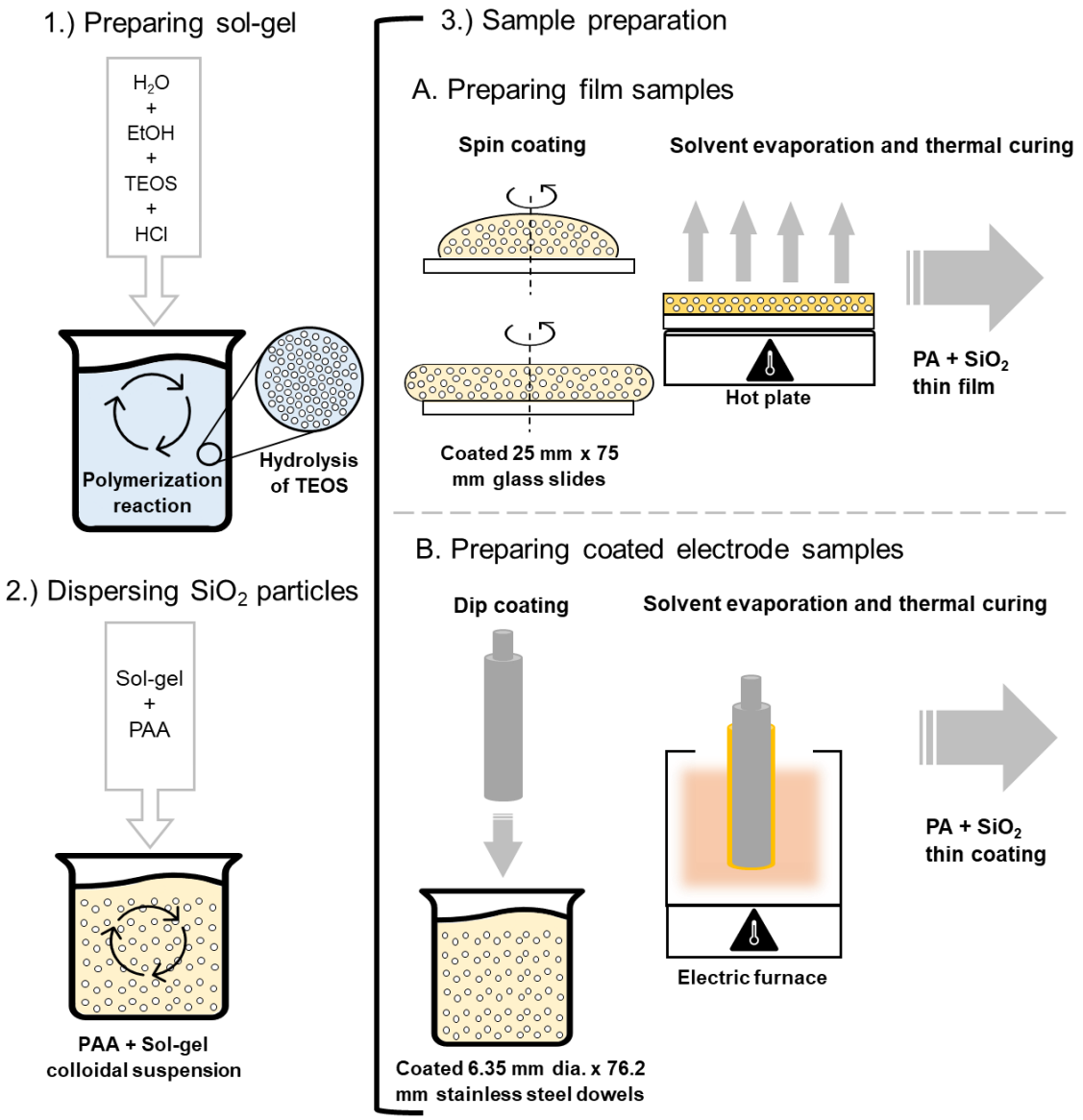

Note. Processing methods used for precursor development, substrate coating, and thermal curing of PA/SiO_2 nanocomposite dielectric thin film samples.

A spectrum of various weight percent concentrations (0%, 2%, 4%, 6%, and 8%) of SiO_2 nanoparticles in samples was prepared for a comparative study of material properties. It was experimentally verified that the commercial polyamic acid precursor contained 15 weight percent polyamide and the sol-gel contained 18 weight percent SiO_2 particles after thermal curing [108]. Then, the molar ratios of the precursors were converted to the weight percent ratios of 11.03% DI water, 14.09% EtOH, 63.73% TEOS, and 11.15% HCl [108]. Therefore, with a given starting mass of polyamic acid precursor, the required initial sol-gel mass and the masses of its precursor constituents could be determined for a desired SiO_2 particle weight concentration in the composite.

2.2.2 Thermal Curing Processes

Completing thermal curing operations on polymer nanocomposite suspension coated substrates is the final step to developing samples for experimental characterization. The curing steps must remain compatible with superconductor manufacturing methods by 1) not exceeding the temperature threshold upon which damage to superconductors can occur and 2) exhibiting characteristics that are scalable to the larger processing operations through which HTS systems are currently manufactured. Parametric studies were utilized to develop the multi-step, low temperature curing process required for solidification of the nanocomposite enamel coating material shown in Figure 7 [108]. Figure 8 shows the completed PA/SiO_2 thin film and coated electrode samples. The cured slide and dowel coatings have an average thickness of 20 μm and 17 μm, respectively.

Figure 7

Thermal Curing Profile of Polyamide

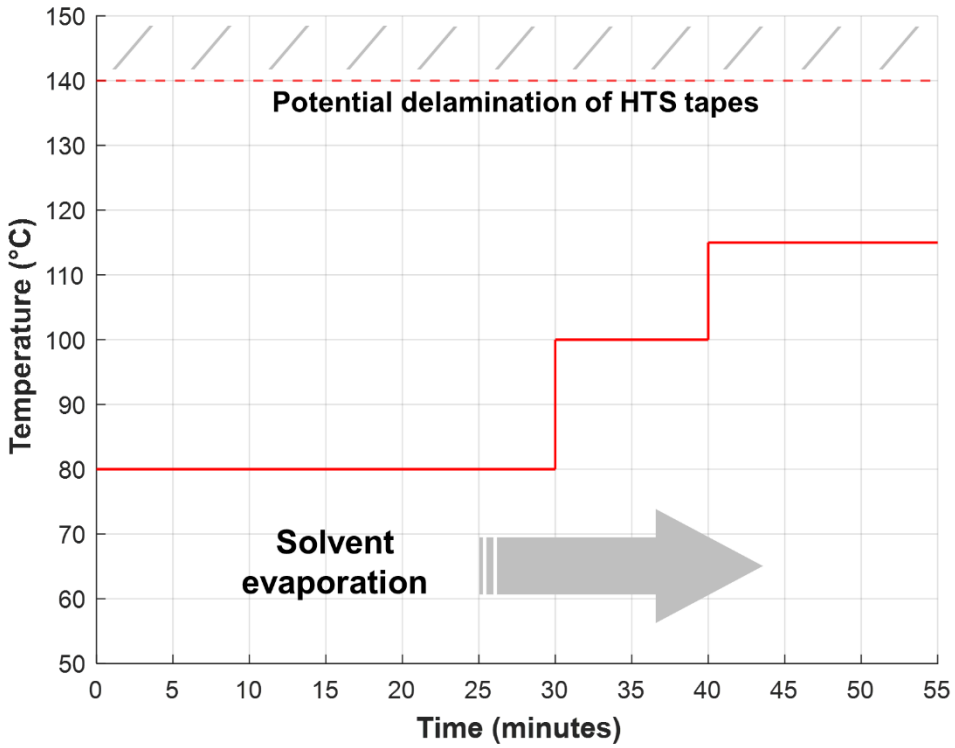

Note. Step profile of curing time and temperature used to prepare PA/SiO_2 dielectric enamel coatings.

Figure 8

PA/SiO_2 Nanocomposite Test Samples

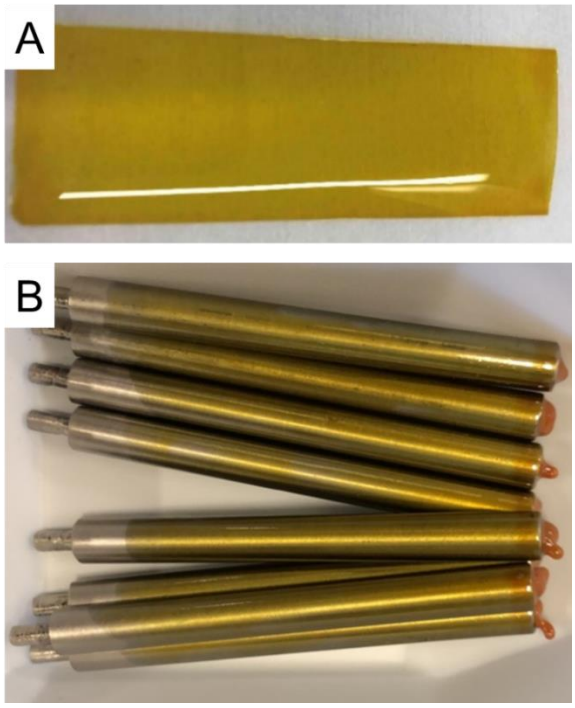

Note. PA/SiO_2 thin film samples (A) and PA/SiO_2 coated electrode samples (B).

Thermogravimetric analysis (TGA) is often utilized to identify mechanisms that improve the thermal stability in polymer coating materials by measuring the changes in their mass with temperature [83]. This study must verify that all solvents are evaporated from the nanocomposite coating and a thermally stable polyamide matrix is developed from the precursor solution using the temperature step profile shown in Figure 7. Shown in Figure 9, a TA instruments Q600 SDT thermogravimetric analyzer was used to heat pure polyamide thin film samples from 25 °C to 800 °C at a rate of 10 °C/minute, under a constant nitrogen gas flow of 100 ml/min. The fully cured curve in Figure 9 successfully demonstrates that a thermally stable polyamide host material is created from the

temperature step profile used in processing, as no changes in sample mass are present before approaching 150 °C. In order to comparatively observe the sample mass evaporation process, the prebaked polyamide curve was created from a sample that had only been previously heated at 80 °C for 10 minutes. As labeled in Figure 8, solvents in this sample had not fully evaporated and sample mass was not stable before 150 °C. Both curves verify that the thermally dependent imidization reaction occurs roughly between 150 °C and 250 °C, where the samples are converted from polyamide into polyimide [109]. Before the onset of thermal degradation, the thermally stable region of polyimide that extends past 500 °C demonstrates why this class of high-performance polymers is widely used as a dielectric material in extreme operating environments [40, 72, 110].

Figure 9

Thermogravimetric Analysis

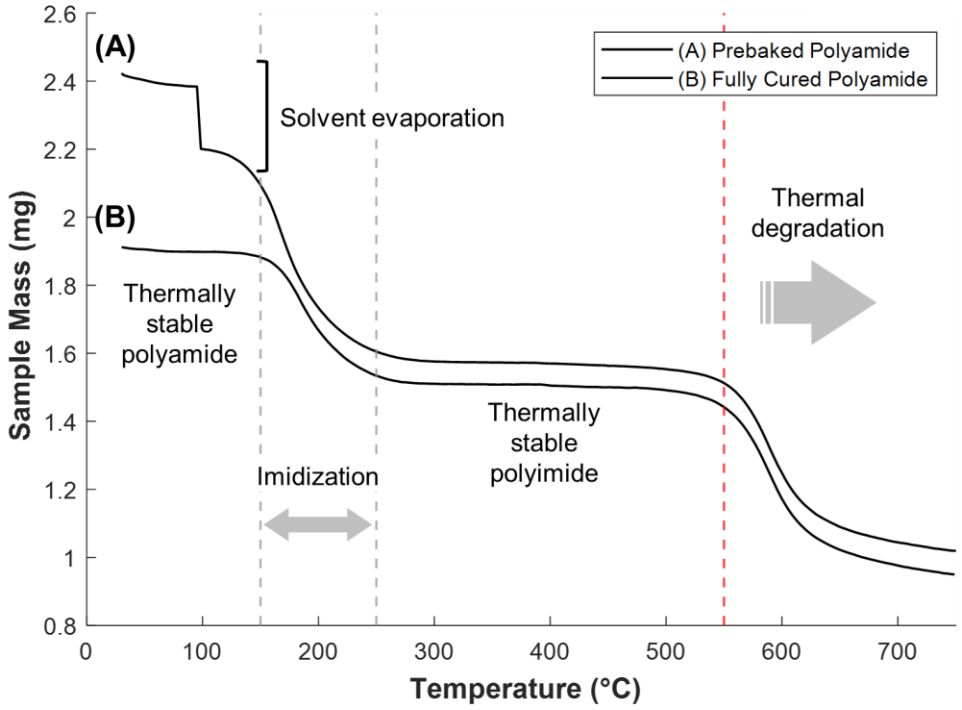

Note. Thermogravimetric analysis of (A) a prebaked polyamide thin film sample and (B) a fully cured sample during heating from 25 °C to 800 °C at a rate of 10 °C/minute, under a constant nitrogen gas flow of 100 ml/min.

2.2.3 Investigating Sample Morphology via Scanning Electron Microscopy (SEM)

Scanning electron microscopy (SEM) is widely utilized as a characterization technique to identify the structures of composite materials at the nanoscale [48, 67]. Following the preparation of PA/SiO_2 thin film samples, SEM imaging with an FEI Apreo system was used to identify the formations of SiO_2 nanoparticles within the polymer host, as well as generally characterize their morphological features. Dielectric

materials are often challenging to image with SEM systems because charges from the electron beam rapidly accumulate on their surface and physically deteriorate the material. Techniques such as backing sample viewing stubs with conductive carbon tapes, lightly sputtering gold coatings on sample surfaces, and covering samples with copper tapes adjacent to the viewing area were employed as tactics to mitigate charge accumulation on the surfaces of PA/SiO_2. Figure 10 shows various images of a 6% weight concentration of SiO_2 nanoparticles in the polyamide host. The images of particles ranging from 50 nm to 200 nm in diameter verify that the preparation methods used in this study are effective in producing spherical, well dispersed, predominantly agglomeration-free particle matrices. These characteristics are critical to maximizing the volume of radial interphase region throughout the bulk of the material and therefore gaining the greatest possible material property benefits from the introduction of nanoparticles.

Figure 10

SEM Imaging of Polyamide / 6 wt. % Nanocomposite Sample

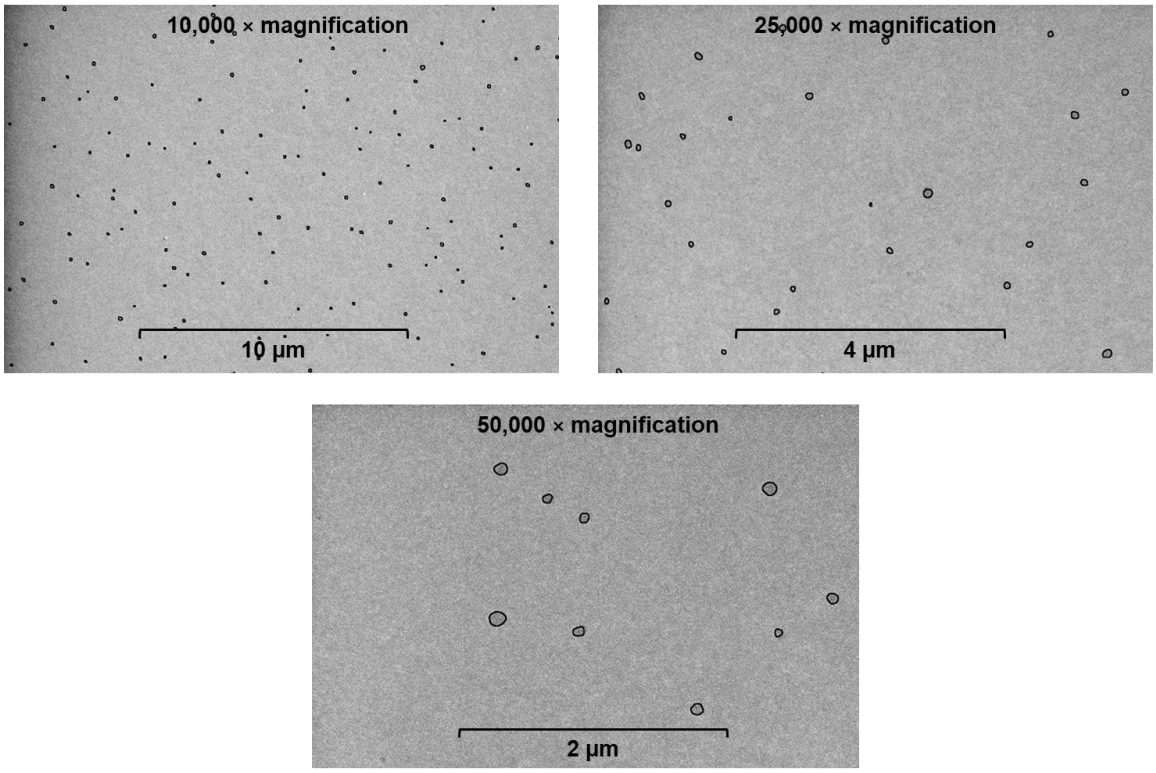

Note. SEM images of a 6 wt. % SiO_2 nanoparticle matrix generated by the Stöber process in the polyamide host.

Additional SEM characterization efforts were conducted on PA/SiO_2 nanocomposite samples to verify that the structures identified visually as nanoparticles were in fact comprised of silica. An Oxford Instruments energy-dispersive X-ray spectroscopy (EDS) accessory for the SEM system features an additional detector that measures characteristic X-rays emitted by a given element when higher energy electrons fall to the ground state to replace excited, escaped electrons [111]. Figure 11 shows elemental maps of an SiO_2 particle matrix generated from a 3-hour long sol-gel mixing

period, which permitted significantly larger particle growth. The elemental maps of silicon and carbon are created from K-alpha emission line signals generated when a high energy electron transitions to the innermost K shell of the characteristic atom [111]. The clustered structures depicted in the silicon signal successfully represent individual particles as localized elemental concentrations. However, perhaps due to the direct bonding interaction of the polymer at the nanoparticle surfaces within the material, the carbon signal shows little differentiation across its map. The challenges faced in imaging dielectric materials are especially present when attempting to generate successful EDS maps, as the beam voltages often accelerate electrons directly through or past the small nanoscale structures.

Figure 11

Energy Dispersive X-ray Spectroscopy (EDS) of Nanoparticles

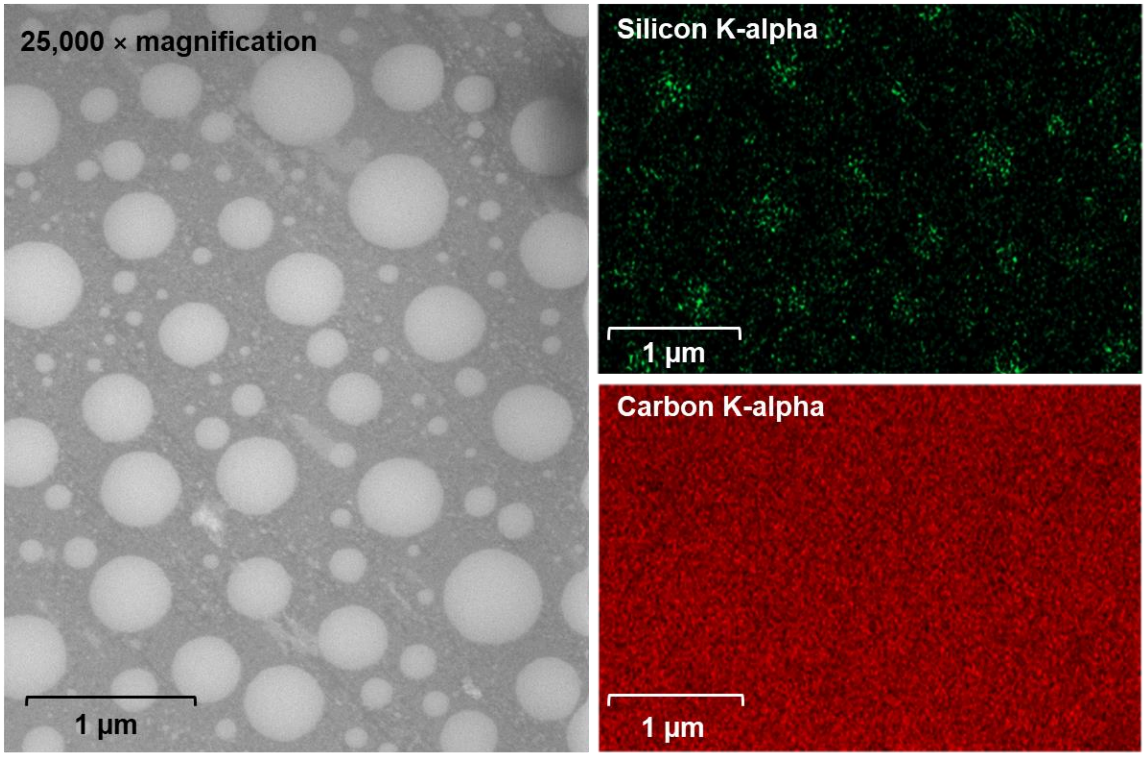

Note. SEM image (left) and EDS elemental maps (right) of a 6 % SiO_2 nanoparticle matrix.

Figure 12 details the efforts in establishing effective boundaries to several key parameters used to produce SiO_2 particle matrices and characterize their impacts to the nanoparticle structure in the Stöber process. Implementing the Stöber process to generate relatively low weight percent concentrations of silica nanoparticles is widely reported and using the preparation methods described here, the uniformly dispersed morphology of individual particles begins to degrade at and above 8 % weight concentrations of SiO_2 [69]. The chain-like formations of silica particle agglomerations can be seen at the top of

Figure 12. In addition, the mixing parameters used in the sol-gel and composite preparation steps are also highly influential in the resulting structures. When the sol-gel precursors are mixed for longer than ~1 hour, the nanoparticles are permitted to grow larger than desired for maximizing the volume of interfacial regions. When the nanocomposite suspension is mixed for greater than the experimentally determined 4-hour period, uniform dispersion is again degraded, but now in the form of individual nanoparticles grouping together in pockets. Both of these changes in morphology can be seen in the middle and bottom SEM images in Figure 12. Experimentally determining the sensitivity of these parameters in the sample preparation method provides critical insight for addressing potential challenges associated with scaling up to manufactured coating production.

Figure 12

Influences of Preparation Parameters on Nanocomposite Matrix

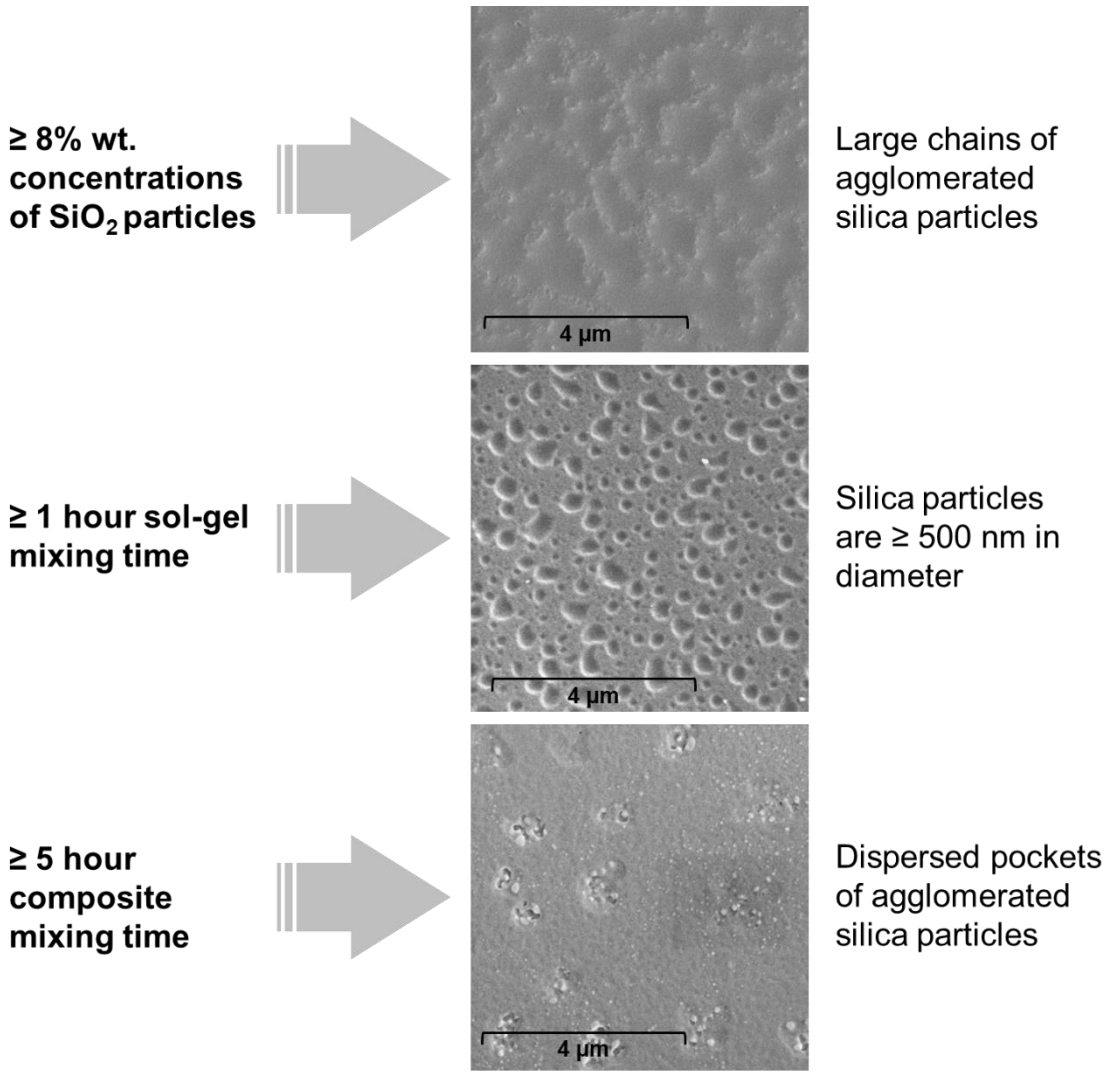

Note. Sensitivity of Stöber process parameters demonstrated by SEM images of various disturbances in the well dispersed morphology of SiO_2 nanoparticle matrices.

Chapter 3

Characterization of Thermomechanical Properties

3.1 Experimental Techniques for Mechanical and Thermomechanical Studies

Investigating the mechanical properties of the nanocomposite is a critical step in this study to verify that SiO_2 particle addition effectively reduces the CTE of the bulk material without excessively decrementing the other material properties such that it cannot be implemented as a manufactured dielectric coating. The true multifunctionality of the silica nanoparticle reinforcement lies in its potential to overcome the drawbacks of traditional agents of polymer confinement by improving thermomechanical properties while simultaneously maintaining, if not improving, toughness and strength [67, 91]. Accordingly, both thermomechanical analysis and mechanical testing are conducted here to establish property relationships between thermal-dimensional stability, mechanical strength, and the weight percent concentration of nanoparticle reinforcement in a given sample.

Testing thin film dielectric enamel samples generally less than 50 μm in thickness requires novel techniques, fixtures, and specialized procedures for preparation, handling, and loading into test frames [112]. The thermomechanical analyses conducted here implement specialized fixtures to accommodate thin film samples with the testing system. For mechanical testing, previous studies have used indirect methods such as depth sensing indentation, bulge testing, and microbeam bending to extract mechanical properties of the material when thin film samples were especially brittle or delicate to handle [113]. However, tensile testing can directly indicate material properties under

conditions that are analogous to axial stresses on thin dielectric coatings during operation [114]. Also, tensile testing permits using sample dimensions that are required for representative volume elements when testing composite materials [115]. Therefore, novel methods and apparatus were developed in this study to address unique design considerations associated with the testing of cryogenic dielectric materials. In accordance with the ASTM D882 standard, these considerations included preparing samples consisting of strips of uniform width and thickness, preventing sample slippage under tension relative to the grips, and appropriately compensating for the toe region at the zero-strain point of tests [116].

3.1.1 Thermomechanical Analysis Techniques

Thermomechanical analysis (TMA) is an exceptional tool for providing valuable characterization information on the thermal stability of highly filled or highly crosslinked polymeric materials [117]. The TA Instruments Q400EM Thermomechanical Analyzer, shown in Figure 13, was implemented with a thin film tension setup for thermal expansion measurement to verify that nanocomposite samples showed improved resistance to dimensional changes across a given temperature gradient. In addition, the thermomechanical tests compared the neat polyamide film with the SiO_2 nanocomposites to establish the degree to which increasing weight percent concentrations (2%, 4%, 6%, 8%) impacted the thermal stability of the material. Thin film samples (4 mm wide × 20 mm long) were cut from the surface of coated glass microscopy slides and loaded into clamp fixtures that suspended the samples in an environmental test chamber. The clamp fixtures were assembled in a 13.6 mm gauge block that ensured sample gauge lengths were repeatable between individual tests.

Figure 13

Thin Film Test System for Thermomechanical Analysis

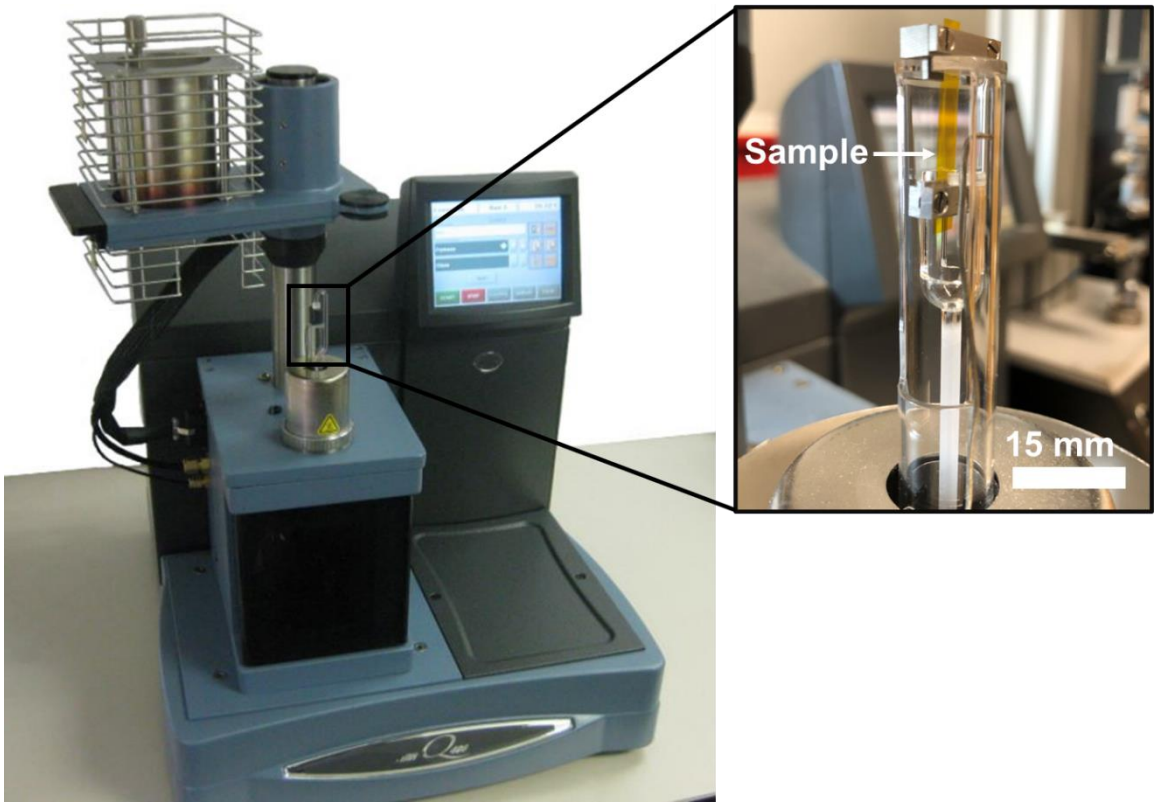

Note. TA Instruments Q400EM Thermomechanical Analyzer with thin film tension setup for thermal expansion measurement.

In each test, the temperature of the environmental test chamber was ramped up from 25 °C to 125 °C at a rate of 5 °C/min, under a constant nitrogen purge gas flow of 80 ml/min, while the sample was loaded with a constant force of 0.25 N. Linear thermal expansion in the direction of the loading force was measured with a Linear Variable Differential Transducer (LVDT), which converts the linear motion of the moving stage into a corresponding electrical signal. Figure 14 shows a diagram of the environmental

test chamber conditions used in these experiments, which were conducted in triplicate for the neat film and each weight percent concentration of the nanocomposite.

Figure 14

Detail of Environmental Testing Conditions for TMA

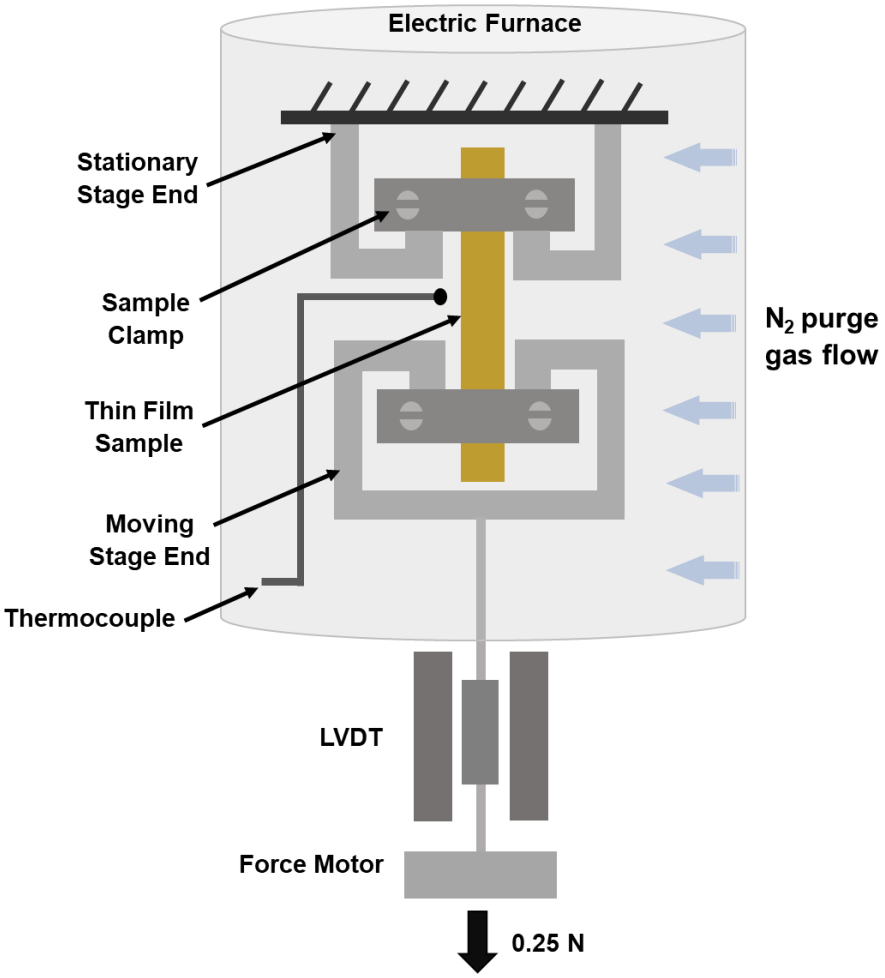

Note. Environmental test chamber conditions of the TA Instruments Q400EM Thermomechanical Analyzer used in the experiments of this study.

3.1.2 Design and Implementation of Mechanical Testing Systems

To effectively characterize the behaviors of PA/SiO_2 nanocomposite materials in the operational environment of high-temperature superconductors, one objective of this study was to test samples in the presence of cryogenic coolants in addition to at room temperatures. A survey of existing tensile testing systems designed for mechanical characterization at cryogenic temperatures indicated that the instruments were either benchtop assemblies using liquid nitrogen filled containers with no control over sample cooling profiles, or complex environmental chambers with cryogenic fluid refrigeration and heating elements to modulate temperatures [118-120]. The primary issue associated with the use of the existing benchtop apparatuses was the lack of precise control over sample cooling profiles during liquid nitrogen immersion, which often resulted in thermal shocking of the test samples [121]. When combined with the high brittleness of thin film dielectric samples, significant measurement errors could occur. The other test system options required a substantial initial investment in cryogenic fluid refrigeration systems with highly specific capabilities for testing materials. These challenges called for an alternative approach that could 1) facilitate cryogenic tensile testing of thin film samples with an adequate level of control over environmental conditions and 2) be easily integrated with conventional mechanical testing tools for effective, efficient characterization of properties. To meet these requirements, a cryogenic tensile testing system that provided a practical, cost-effective solution for conducting reliable and repeatable tests on thin film samples was designed and implemented. The accuracy and applicability of the designed apparatus was demonstrated by integrating it into a

conventional test frame and using it to obtain repeatable stress-strain data in LN_2 cooled environments.

A liquid nitrogen-cooled, cryogenic environmental testing apparatus was developed specifically for testing thin film dielectric materials. The system was designed to be easily integrated into an existing Shimadzu AGS-X load frame with a 10 kN load cell capacity, but also with the option to be used with other conventional tensile test frames. The test frame design concept is shown in Figure 15. The design contains 6.35 mm thick waterjet cut 304 stainless steel plates, upon which two custom fabricated stainless-steel grippers are mounted. The bottom section of the test frame, where the bottom grip is fixed, has a stationary base and the top grip is fixed to a pull-rod that moves with the crosshead of the load frame. The serpentine geometry of the test frame design improves upon existing experimental apparatus by eliminating the need for a feed-through from the conventional load frame to the bottom grip that seals against LN_2 leakage [122].

The environmental chamber vessel consists of a 1000 mL off-the-shelf vacuum insulated flask, used to minimize the evaporation of liquid nitrogen once the vessel is sealed. A polylactic acid (PLA) 3D printed top cap uses an elastomer gasket to seal the environmental chamber. It also contains the feedthrough ports for two thermocouple wires (see Figure 15 B), as well as a fill port with fill tube to pour in liquid nitrogen coolant after the chamber is sealed. This full assembly can be seen in Figure 16A. The long fill tube shown in Figure 16 B is implemented to eliminate any possible exposure of the thin film sample to liquid nitrogen and avoid the potential for thermal shock. If complete sample immersion in liquid nitrogen at -200 °C is desired, the sealed chamber

can be filled up to a thermocouple positioned above the sample (see Figure 15 A). However, for thin film applications where mild cooling profiles are generally desired for investigating temperature-dependent stress-strain responses, the chamber can be filled to a lower level using thermocouple 1 as a level indicator and thermocouple 2 for monitoring the sample temperature.

Figure 15

Design of LN_2-Cooled Environmental Tensile Testing Chamber

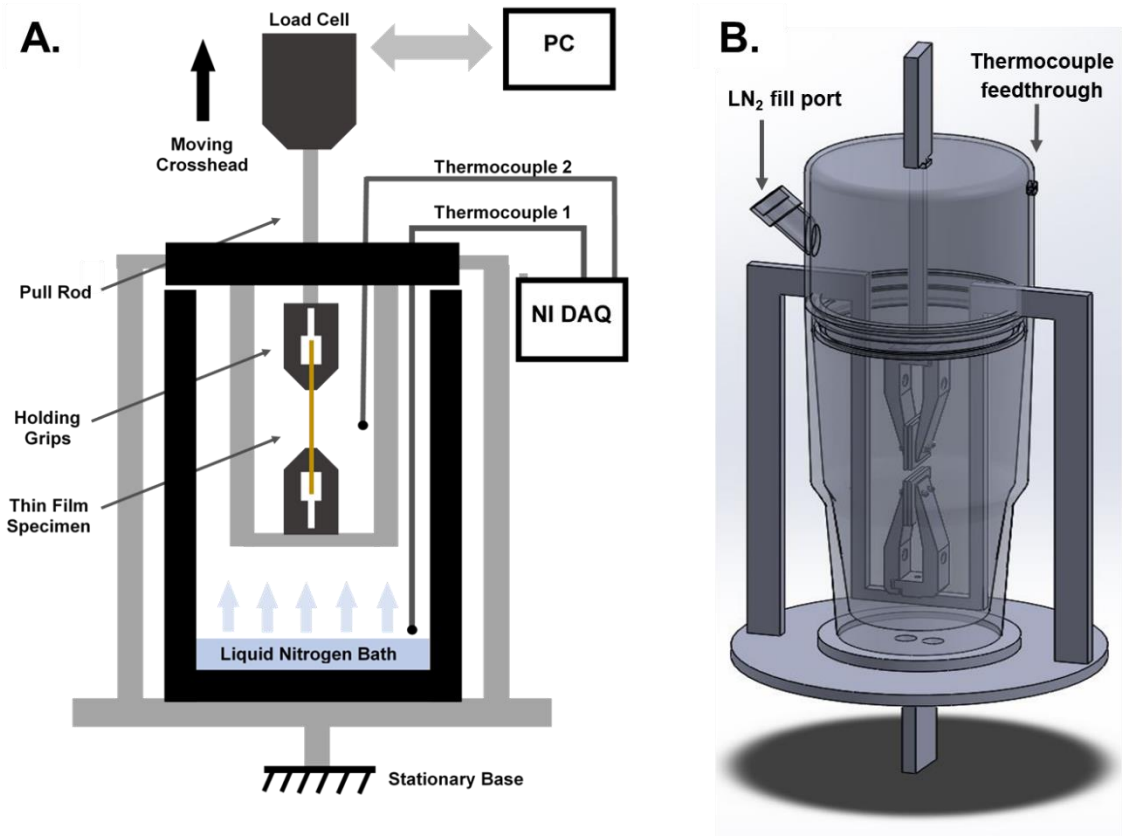

Note. (A) Conceptual design and (B) CAD model assembly of the environmental tensile testing chamber.

Stainless steel tabs mounted to the stationary and moving ends of the apparatus prototype shown in Figure 16 are inserted directly into the existing grippers of the conventional load frame. As reported by other research groups, initial tests showed that manually tightened serrated grips, which apply a pressure on the sample ends, may lead to sample slippage if the pressure is insufficient, or damage to the sample near the grips if the pressure is too high [123]. In some cases where mechanical gripping is not possible, adhesives are used to fasten brittle samples to a testing apparatus [124]. However, to overcome this challenge while enabling efficient sample loading and unloading, the custom grippers shown in Figure 16 C were fabricated. The grippers use parallel plates that maximize surface area and static friction to safely grip thin films without damaging them or allowing slippage to occur, as per ASTM D882. In order to address potential concerns in frame bending and grip slip between the main fixture and the test frame, a 2D Digital Image Correlation (DIC) study and finite element simulations of a thin film test of Kapton^{TM} polyimide were used to verify that the deformations of the fixture during mechanical tests were minimal. The results of these studies can be seen in Appendices A and B.

Figure 16

Assembly of Cryogenic Thin Film Tensile Testing System

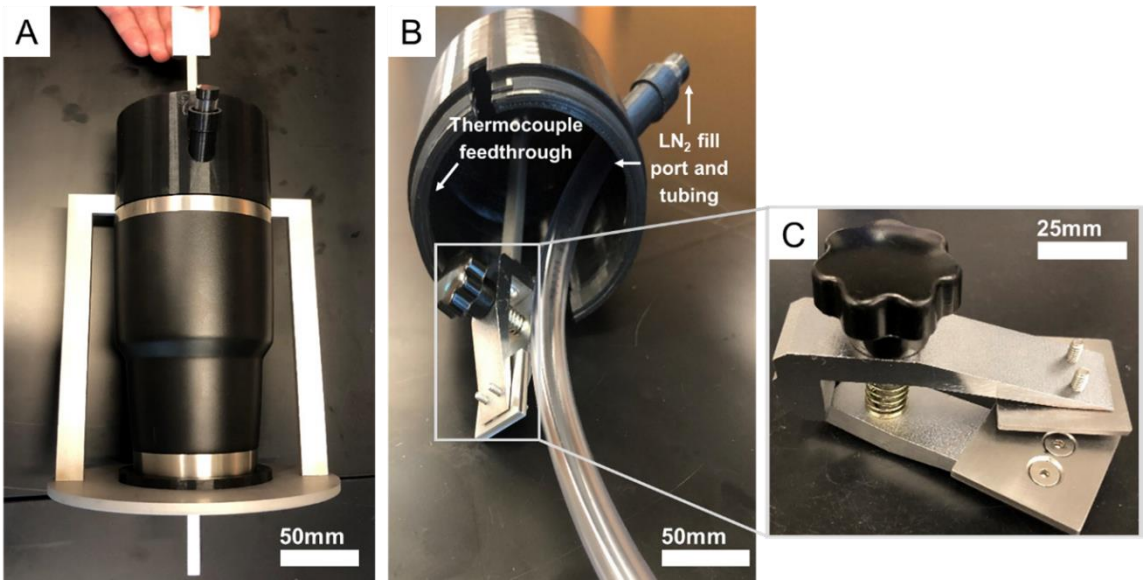

Note. (A) Assembly of the environmental test chamber apparatus, with (B) top cap with feedthrough ports, and (C) parallel-plate grippers for mitigating slippage of thin film samples during cryogenic tests.

The experimental setup used for characterizing the tensile mechanical response of PA/SiO_2 thin film is presented in Figures 17 A and 17 B for room temperature and subzero temperature conditions, respectively. Three samples for each weight percent concentration and temperature condition were cut from glass slides, then measured before testing. Each sample had a gage length of 25 mm, allowing it to extend out from the rear edge of each grip. Samples were loaded to have slack at the beginning of each test to prevent any tearing when tightening the grips. For the testing, true stress, σ, defined as the ratio of the tensile load, P, to the instantaneous cross-sectional area, A, was used. The

cross-sectional area was determined using volume consistency. Similarly, the logarithmic definition of strain (i.e., true strain, ϵ) was used as the metric for strain.

Figure 17

Experimental Setup of Thin Film Tensile Testing System

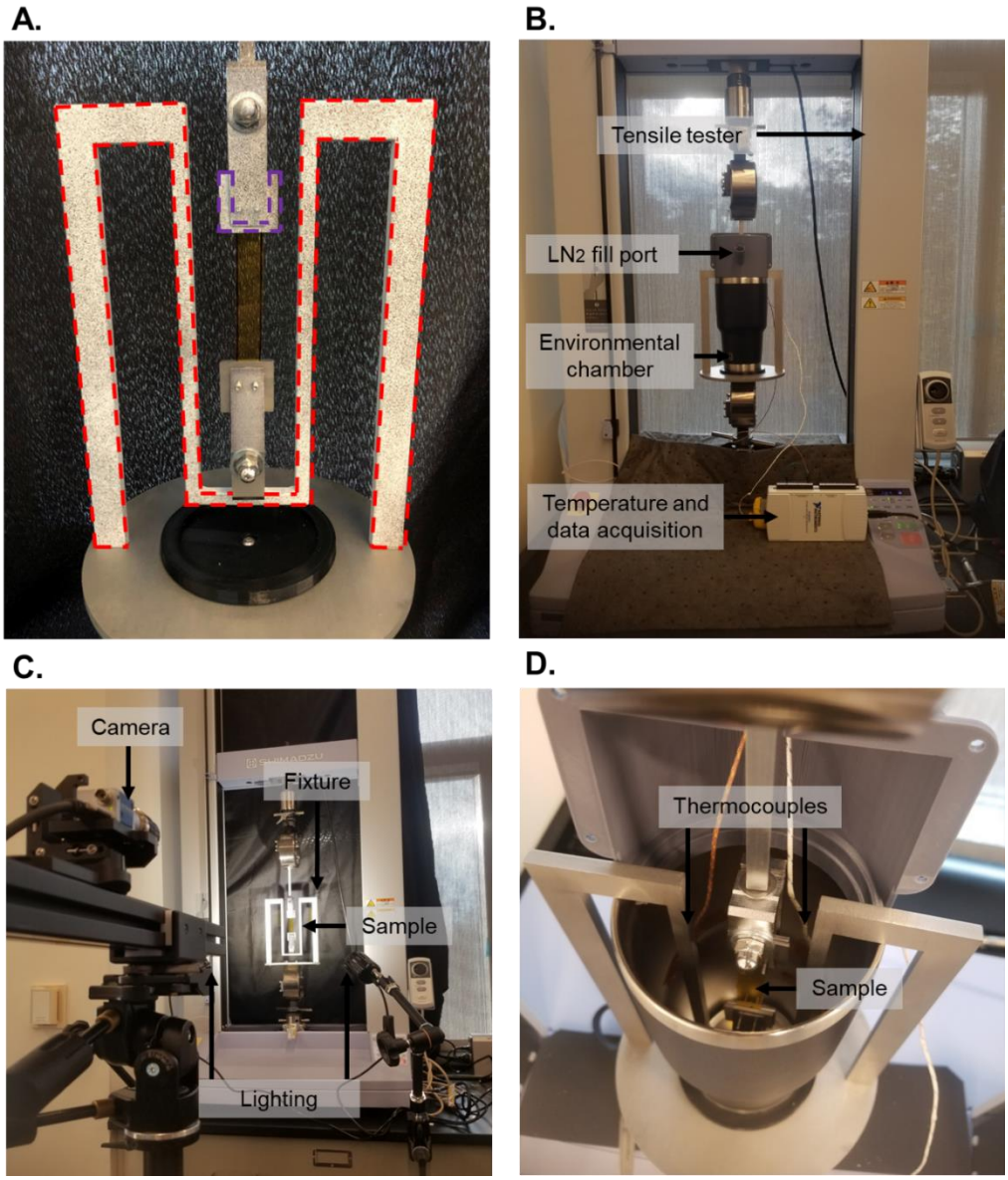

Note. (A) The base fixture with the region of interest for DIC marked in red dashed lines and the region of interest for the top grip marked with dashed purple lines. (B) The complete apparatus configured for cryo-temperature testing. (C) The experimental setup for DIC. (D) A loaded sample in the cryogenic environmental chamber.

The base of the environmental chamber shown in Figure 17 B was filled with LN_2 from the inlet at the top of the apparatus, where it is fed directly to the bottom of the chamber. The LN_2 fill level was checked with a second thermocouple whose values were not recorded. The samples were not submerged in LN_2 in these experiments, as they become too brittle for reliable testing. For thermal stabilization of the sample and the chamber, a 5-minute cool-down period between LN_2 filling and tensile testing was allowed to ensure a repeatable, quasi-steady state temperature in the environment. Though the apparatus could approach a stable testing temperature that is measured at the center of the test specimen, a vertical temperature gradient can potentially exist along the length of the specimen. Loading the samples in slack was a critical step for mitigating these effects by decreasing the vertical dimension of the samples during cooling. A loaded sample with attached thermocouples in the environmental chamber is shown in Figure 17 D. Room temperature conditions were recorded using an infrared thermometer (ETEKCITY, Lasergrip 1080) at the start of each test for later use in Appendix B simulations. Figure 18 plots the variation in three of the low temperature tests, where temperature profile data was collected at a rate of 4 Hz using a National Instruments data acquisition system. As shown in the Figure, the temperature repeatedly approaches -90 °C at the initiation of tests within a 10 % error band.

Figure 18

Temperature Profile of LN_2-Cooled Tensile Tests

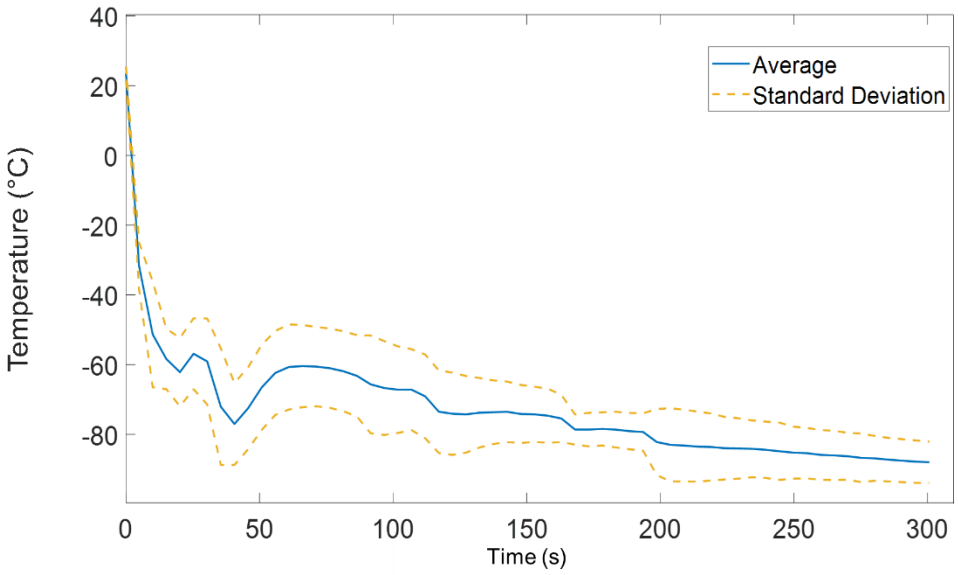

Note. Test-to-test variability of the experimental cooling profile inside the environmental chamber and during the cool-down period.

3.1.3 Techniques for SEM Characterization of Particle-Polymer Interfaces

Plasma etching is frequently utilized as a tool for surface modification of thin polymer films. Through various mechanisms, controlled etching processes are completed on certain phases of a material through interactions with precise bonds [48, 125-127]. In this study, a Plasma Prep III™ Solid State Low Temperature Etcher was implemented with the goal of exposing the PA/SiO_2 system to a plasma treatment, where the different etching rates of the two distinct materials can help reveal the embedded nanoparticles in an inner cross section of the sample beneath the surface [126]. An oxygen glow discharge

was produced in a mild vacuum chamber by excitation and subsequent ionization of the gas through radio frequency (RF) power [128]. Specifically for the study, at a chamber pressure of roughly 200 mTorr, the coated slide samples were subject to a 50 psi oxygen carrier gas flow excited by 50 W of RF power for a 1-minute duration. Since oxygen gas plasmas are known to be highly reactive, various chemical and physical mechanisms such as chemical reactions, ion bombardment, dissociation of chemical bonds, and resulting temperature effects are involved in the interactions between the oxygen plasmas and the samples. These mechanisms have been employed with the objective of revealing an inner cross section of the nanoparticle matrix for SEM imaging [125, 127, 129]. The resulting SEM imaging on structural effects in the samples could then potentially be used to hypothesize about material properties in the regions where particle-polymer interfacial mechanics are dominant and relate them to the results of the thermomechanical studies.

3.2 Analysis and Discussion of Results from Mechanical and Thermomechanical Studies

The results of the mechanical and thermomechanical characterization efforts in this section are critical to establishing an understanding of material property relationships for the polymer nanocomposite. These separate material properties and the trend of each property with respect to the weight percent concentration of SiO_2 nanoparticles were utilized to locate an optimal material for implementation in the cryogenic operating environment of HTS power transmission systems.

3.2.1 Establishing Tunable Thermomechanical Property Relationships

Figure 19 shows the results from the thermomechanical analyses, where various weight percent concentrations of PA/SiO_2 nanocomposite films were subject to a 25 °C to

125 °C temperature ramp test under a constant, uniaxial tension of 0.25 N. Tests were conducted in triplicate for each concentration shown. Similar to what has been reported in various other studies, the addition of lower CTE SiO_2 nanoparticles to the polyamide host reduces the bulk material's response to the thermal load, effectively improving the thermal dimensional stability of the material [57, 76, 83, 130]. The 6 wt. % concentration of the material maximizes this effect, with a thermal stability improvement of 30%. Figure 20 compares the thermal dimensional response of a neat polyamide sample with a 6 wt. % PA/SiO_2 nanocomposite. This data can be utilized to calculate the resulting linear CTE (see Equation 1) for comparing various concentrations to literature values of other materials [73]. The calculated CTE of the neat polyamide tested here is 62×10^{-6} K^{-1}, while the 6 wt. % PA/SiO_2 nanocomposite reduces this to 38×10^{-6} K^{-1}. This nanocomposite shows improved thermomechanical performance over Kapton™ polyimide itself ($\alpha_{\text{Kapton}} = 46\times10^{-6}$ K^{-1}) and significantly reduces its CTE mismatch with dissimilar HTS cable materials ($\alpha_{\text{304 Stainless}} = 15\times10^{-6}$ K^{-1}) [40, 73, 131]. As shown in Figure 19, the enhanced thermomechanical performance begins to diminish at the 8 wt. % nanocomposite concentration. This correlates with the uniformly dispersed morphology of sol-gel prepared particles degrading at and above 8 % weight concentrations.

$$\alpha = \frac{1}{L}\frac{dL}{dT} \tag{1}$$

Where:

α = coefficient of linear thermal expansion

L = length, mm

T = temperature, K

Ftabl

Figure 19

Average Thermal Expansion of PA/SiO_2 Concentrations

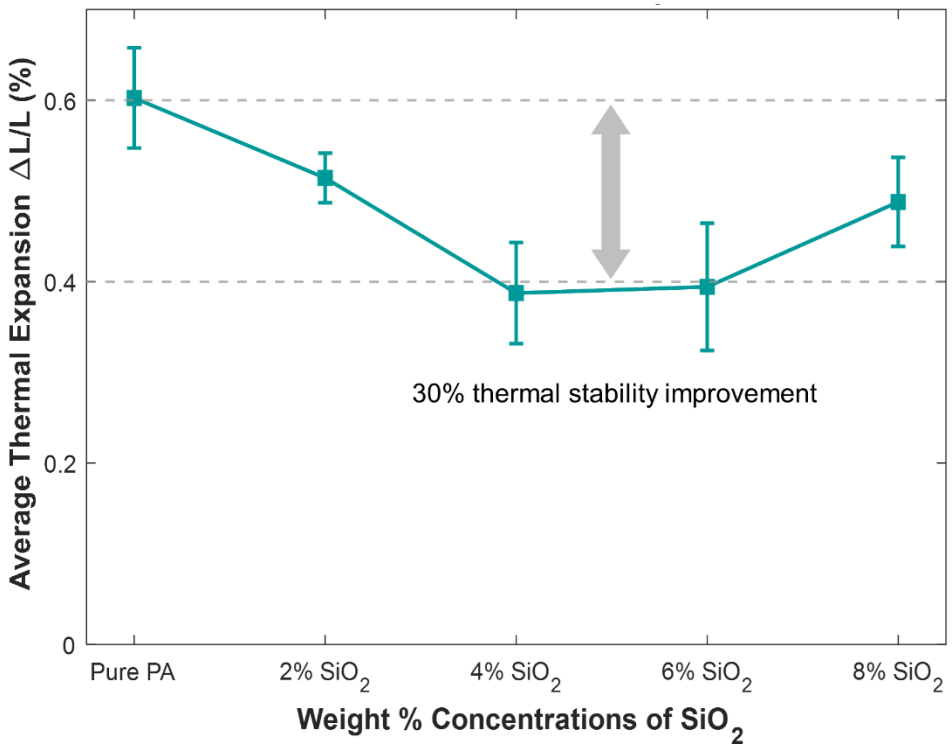

Note. Results from thermomechanical analyses show the average linear thermal expansion of 0%, 2% 4%, 6% and 8% PA/SiO_2 nanocomposite samples following a 25 °C to 125 °C temperature ramp test.

Figure 20

Thermal Response of PA/SiO_2 Thin Films

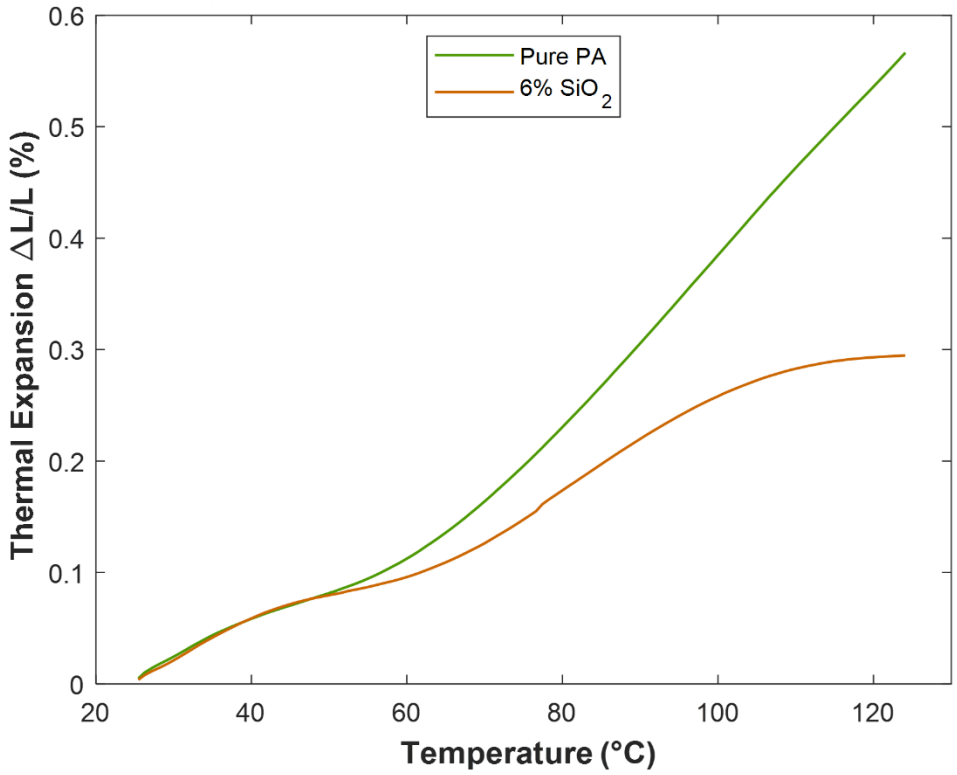

Note. The linear thermal response of a pure PA sample compared to that of a 6% PA/SiO_2.

In order to provide a metric for assessing the strength of SiO_2 nanoparticle bonding to the polyamide matrix, and the influence of imperfections in the material, a model can be implemented to predict the ideal elastic modulus of the nanocomposite at room temperature. Equation 2 is the simplest form of a rule of mixtures model for predicting the ideal elastic modulus in a two-phase particle reinforced system [132, 133]. The model uses the weighted contributions of material properties from the SiO_2 and polyamide at given concentrations [134]. This method neglects reduced stiffening due to imperfections at nanoparticles interfaces and assumes perfect bonding. Therefore, it is

expected that the recorded experimental elastic modulus will be lower than calculated estimates.

$$E_c = E_m \Phi_m + E_f \Phi_f \quad (2)$$

Where:

E_c = Elastic modulus of nanocomposite, MPa

E_m , E_f = Elastic moduli of matrix and filler, MPa

Φ_m , Φ_f = Volume fractions of matrix and filler

The stress-strain curves for various weight percent concentrations of the PA/SiO_2 samples at both room and cryogenic temperatures are shown in Figures 21 and 22, respectively. Figures 23 and 24 show the average elastic modulus and ultimate tensile strength for the samples in both temperature conditions. A summary of these properties can be found in Table 1. Tests were conducted in triplicate for each concentration shown. At room temperature, as shown in Figure 21 and reported by other studies, increasing the concentration of the SiO_2 nanoparticles to 6 wt. % improves the tensile mechanical properties of the bulk material [58, 135-138]. Generally, at room temperature, this trend is attributed to the increases in total interfacial volume with low weight percent concentrations of well bonded particles in the matrix [93]. The higher Young's modulus and ultimate tensile strength are results from increasing the volume of locally stiffer interfacial regions [58, 136, 138, 139].

As shown in Figures 23 and 24, the 6 wt. % concentration shows a 16% increase in elastic modulus and a 33% increase in ultimate tensile strength when compared to the neat polyamide film. For the 6 wt. % concentration, the Appendix C rule of mixtures calculation estimated an elastic modulus of 3,317 MPa and the experimentally obtained value was significantly lower at 2,141 MPa. Most particle reinforced composite materials will show experimental values which are lower than rule of mixtures estimates due to the nature of imperfections at individual particle interfaces [132, 140]. Other studies have shown 80% reductions from rule of mixtures estimates to experimentally recorded values at higher concentrations, so this result is expected [132]. Based on other studies, the trends of mechanical property improvement shown in the experimental data will continue to increase with SiO_2 content until reaching a maximum concentration upon which degradation of these properties will occur [141]. With the results presented, it appears that this maximum was not reached due to limitations of the sol-gel process, where the desired nanoparticle matrix morphology broke down at concentrations greater than 6 wt. %.

Figure 21

Mean Stress-Strain Response at Room Temperature

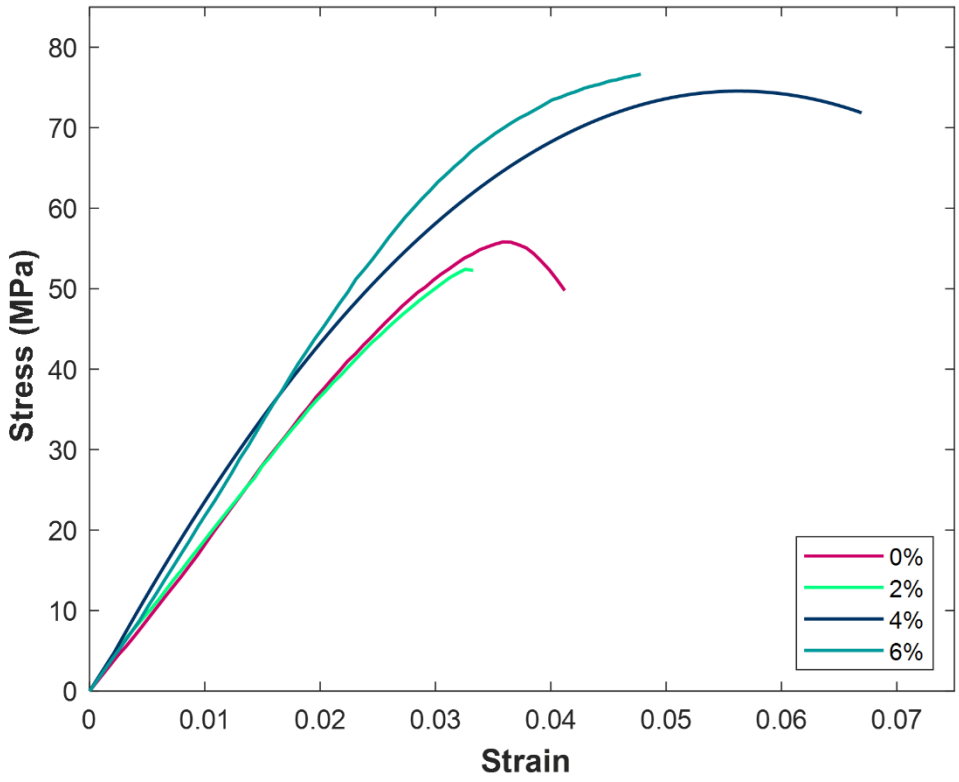

Note. Room temperature tensile testing stress-strain responses of 0%, 2%, 4%, and 6% PA/SiO_2 nanocomposite samples.

Figure 22

Mean Stress-Strain Response at Cryogenic Temperature

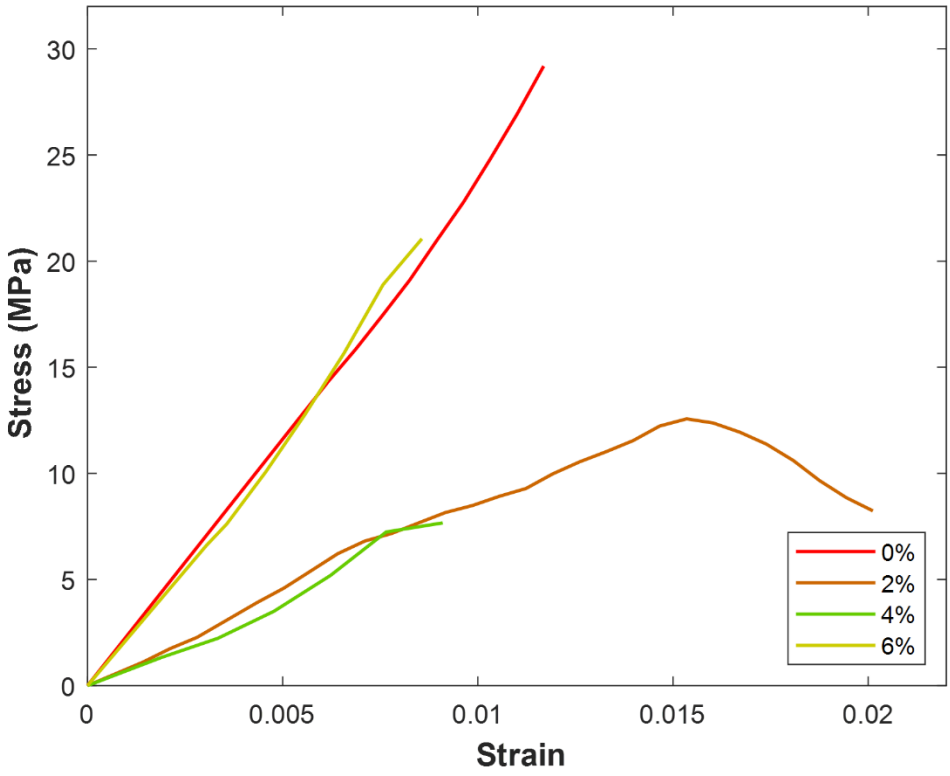

Note. Cryogenic temperature tensile testing stress-strain responses of 0%, 2%, 4%, and 6% PA/SiO_2 nanocomposite samples.

Figure 23

Comparison of Elastic Modulus

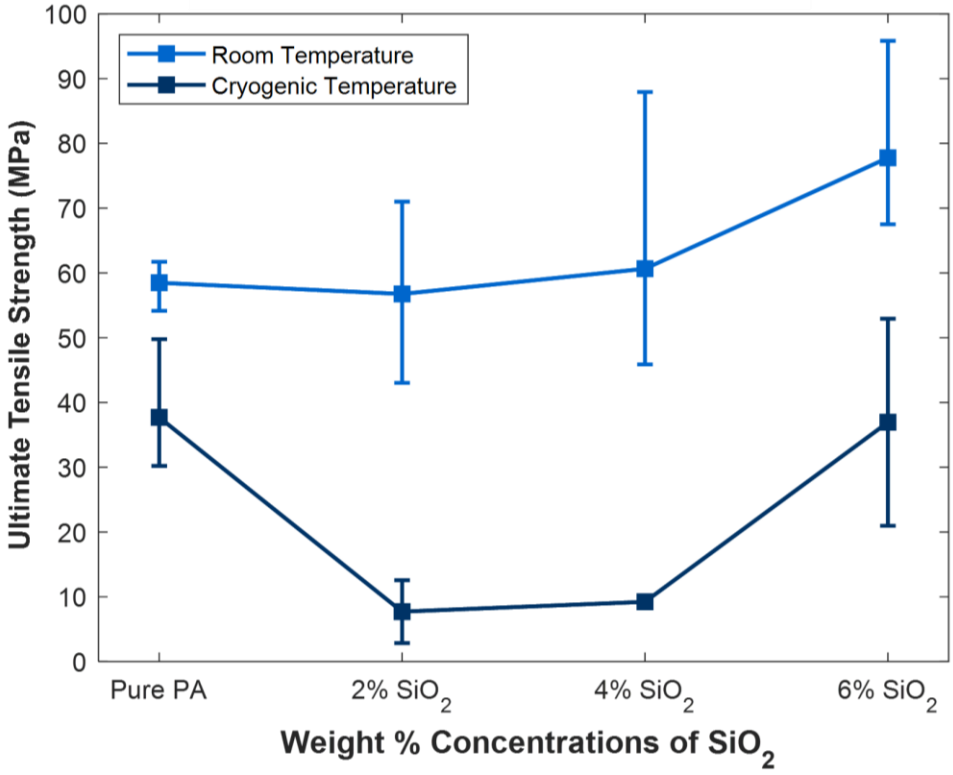

Note. Variation of elastic modulus with 0%, 2%, 4%, and 6% PA/SiO_2 nanocomposite concentrations, at both room and cryogenic temperature environments.

Figure 24

Comparison of Ultimate Tensile Strength

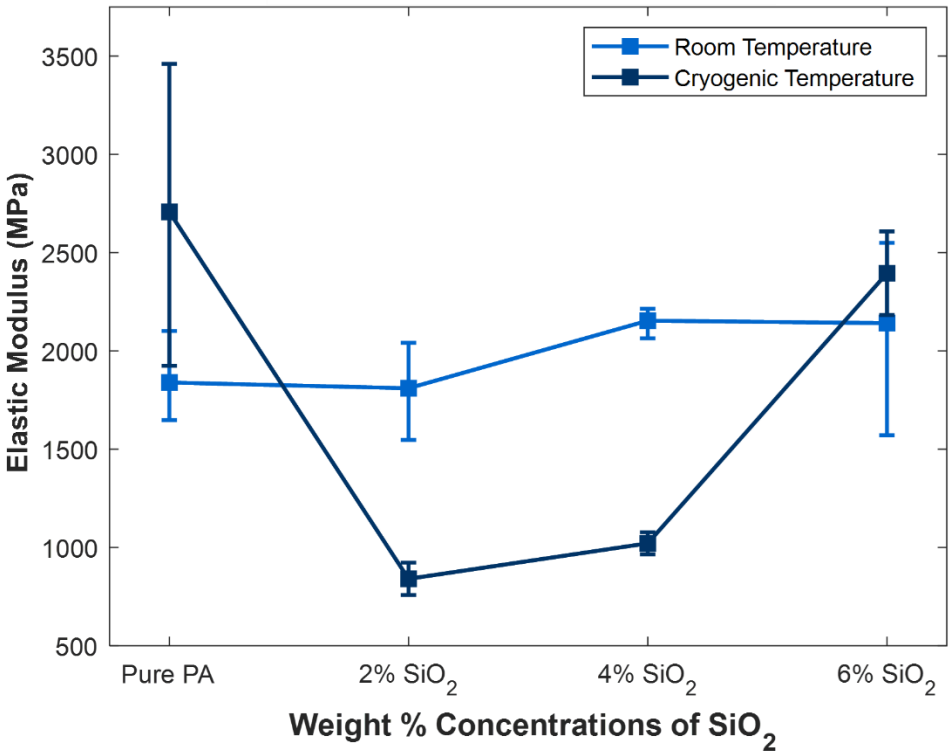

Note. Variation of ultimate tensile strength with 0%, 2%, 4%, and 6% PA/SiO_2 nanocomposite concentrations, at both room and cryogenic temperature environments.

Table 1

Summary of Tensile Properties from Concentrations of PA/SiO_2 Nanocomposites

	Concentration of SiO_2	Elastic Modulus (MPa)	Ultimate Tensile Strength (MPa)
Room Temperature	Pure PA	1,839	58
	2 wt. % SiO_2	1,810	57
	4 wt. % SiO_2	2,109	74
	6 wt. % SiO_2	2,141	78
Cryogenic Temperature	Pure PA	2,707	38
	2 wt. % SiO_2	840	7.7
	4 wt. % SiO_2	1,021	9.2
	6 wt. % SiO_2	2,395	37

At room temperature, the addition of rigid nanoparticles in a polymer induces stress concentrations and alters the local stress state to favor significant increases in local plastic deformation, verified by the room temperature results in Figure 21 and Table 1 [67, 139, 142]. At imperfections such as void spaces in the polymer or at the interfaces of individual particles, the plastic deformation in the adjacent matrix develops into microcracks upon continued deformation [48]. Then, when microcracking begins to propagate, other toughening modes that can help dissipate global strain energy start to take effect. Figure 25 shows 3 potential toughening modes for strain energy dissipation by 1) pinning and arresting crack propagation over rigid particles, 2) continuously deflecting crack propagations around particle interfacial regions, and 3) allowing plastic deformation around stiff interfacial regions to de-bond pinned particles [67, 139, 143, 144]. The greatest toughness increments seen in nanocomposites have first been attributed to the capabilities of plastic void growth mechanisms and then to particle de-bond in dissipating strain energy under tension [145].

Figure 25

Toughening Mechanisms to Dissipate Strain Energy

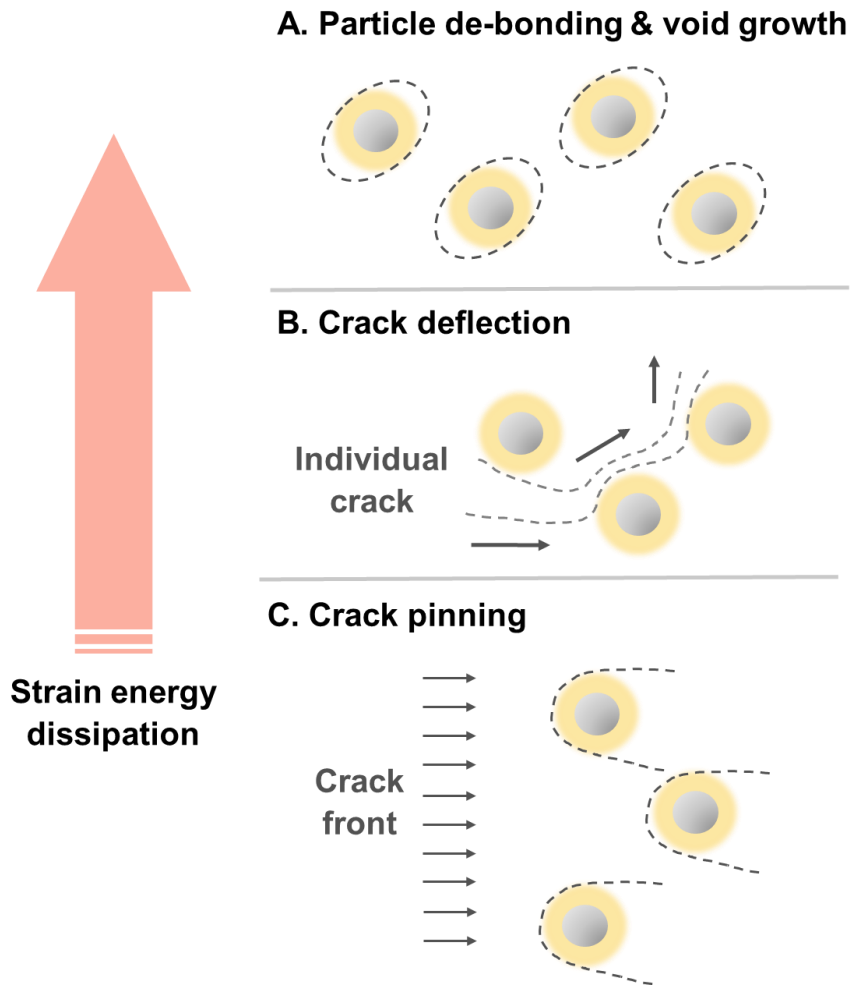

Note. Fracture toughening mechanisms in polymer nanocomposite films under tension.

The mechanical behaviors of the PA/SiO_2 nanocomposites in the LN_2-cooled testing environment are far more complicated. From the neat films to the 2% and 4% concentrations, elastic modulus and ultimate tensile strength decreased as much as 69% and 79%, respectively. Following this, upon reaching the 6% concentration, both

parameters nearly returned to their neat polyamide values. This behavior is unexpected, as bulk material stiffness and fracture toughness are expected to increase in the nanocomposites as well as in the neat films due to the subzero testing conditions [130, 146]. In reality however, the relationships between temperature and the elastic–plastic tensile failure mechanisms of polymer nanocomposites are complex, likely also depending on factors such as bond strengths between the matrix and nanoparticle materials used [136, 143].

Despite wide reporting of strong bonding mechanisms between polyamide and SiO_2 nanoparticles, the selection of nanocomposite filler and matrix materials with highly dissimilar thermal behaviors is likely responsible for the cryogenic testing environment's impact on the decremented ultimate strength of the 2 wt. % and 4 wt. % concentrations [49, 97, 99, 147]. Other studies have reported that due to the significant differences in thermal contraction between silica nanoparticles and the polymer matrix, compressive stress from the polymer causes significant additional loading at individual particle interfaces [130]. Therefore, it can be hypothesized that particle de-bonding and failure propagation via void growth can occur at significantly lower tensile stress at low temperature due to the heightened pre-stressed condition of nanoparticle interfacial regions. In addition, if the thermally pre-stressed particle interfaces are de-bonding at lower tensile stress, the initiation of cracks at interfacial voids can occur earlier and propagate more easily through the brittle material, reducing the effectiveness of crack pinning or deflection mechanisms. Consequently, the pre-stressed particle-polymer interfaces also lower the Young's modulus of the 2 wt. % and 4 wt. % concentrations in the cryogenic environment. This mechanism could limit the bulk material's strength at a

low loading until a sufficiently high concentration of nanoparticles effectively distributes the thermal stress between individual interfacial regions, restoring both Young's modulus and ultimate tensile strength. Figures 26 and 27 show photographs and SEM images of failures from the tensile tests. The SEM imaging of cryogenic tensile test failures shown in Figure 27 verifies the significant reduction of global plastic deformation in failed samples subject to cryogenic cooling.

Figure 26

Images of PA/SiO_2 Thin Film Tensile Failures

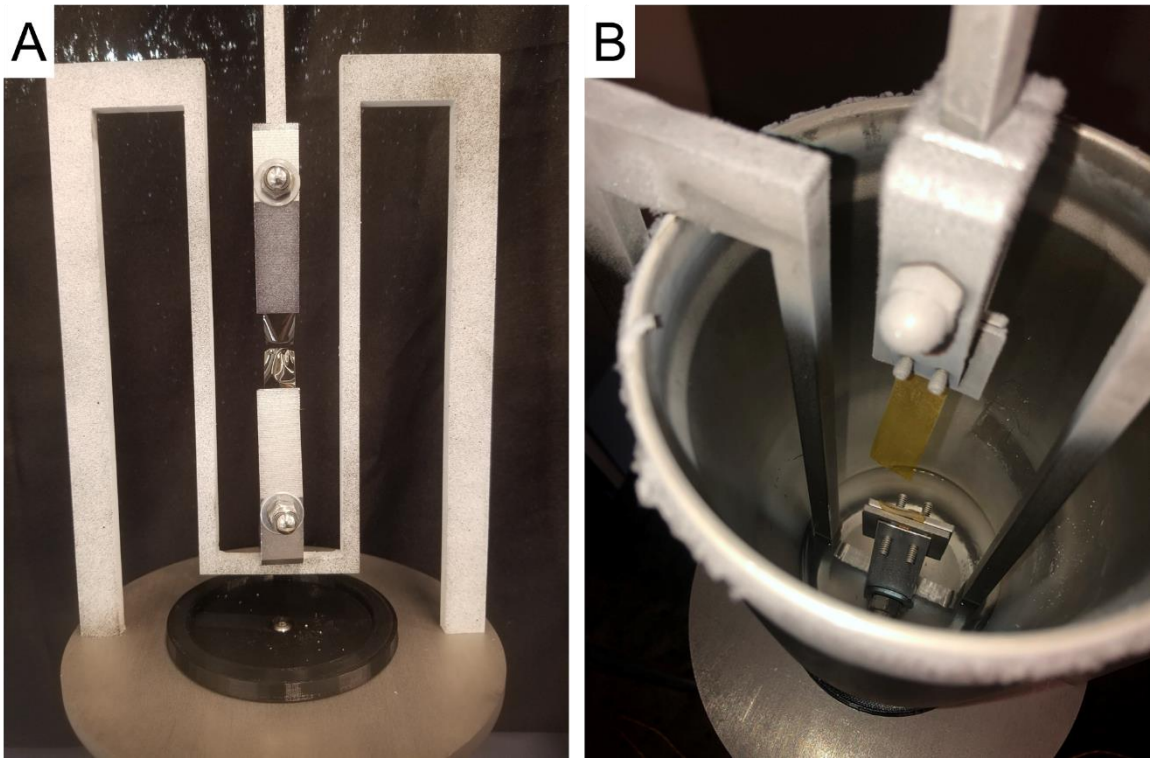

Note. Images of failed nanocomposite samples from room temperature (left) and cryogenic temperature (right) tensile tests.

Figure 27

SEM Images of Temperature Dependent Tensile Failures

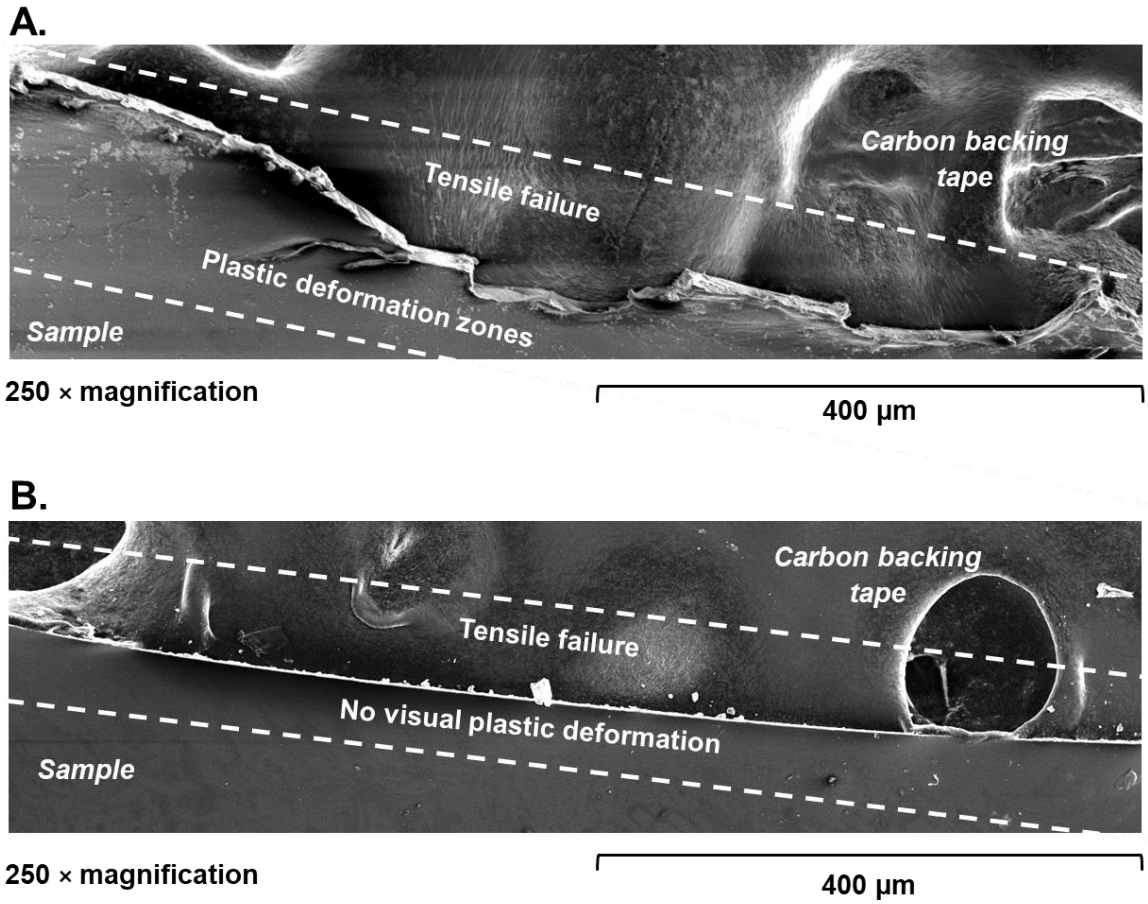

Note. SEM images of failed nanocomposite samples from room temperature (top) and cryogenic temperature (bottom) tensile tests.

To shed light on the hypothesis that increasing the concentration of SiO_2 nanoparticles by small amounts could allow a significant recovery of the material's mechanical properties, calculations were completed to estimate the quantity and volume of nanoparticle interfacial regions that occurred at different concentrations. The density of the nanocomposite was determined from the known densities of polyamide and SiO_2.

Then, the mass, volume, and number of 125 nm diameter SiO_2 particles in a 20 um^3 nanocomposite matrix of a given wt. % concentration could be determined. Using literature estimations of a 40 nm radial thickness in interfacial regions surrounding particles, the total volume fraction of SiO_2 and interfacial area could be determined for different concentrations in the nanocomposite (See Appendix D) [99]. As shown in Table 2, the total volume fraction of SiO_2 and interfacial regions increases from 3.9% (174 particles) at the 2 wt. % concentration, up to 11.8% (524 particles) at the 6 wt. % concentration.

The significantly greater volume fraction of particle-interphase regions within the model shown in Figure 5 at the higher concentration permits the prospect that thermal stress is more evenly distributed throughout the matrix, potentially preventing the weakening of particle-polymer bonding due to low temperatures. However, it is acknowledged that a study focusing on the detailed fracture toughness of this polymer nanocomposite, using methods such as compact tension (CT), tension, flexure, and dynamic mechanical analysis (DMA) is required to verify this proposition [139]. For the purpose of this study, the results showing improved room temperature performance and comparable cryogenic temperature performance at the 6 wt. % concentration nanocomposite demonstrate exceptional multifunctionality. The low temperature processed PA/SiO_2 nanocomposite's thermomechanical stability exceeds other industry dielectric coating options, while maintaining the mechanical properties of the neat polyamide material in low temperature operating conditions. The exceptional mechanical performance of the 6 wt. % concentration studied here makes it optimal for potential implementation as a cryogenic dielectric coating for HTS power transmission systems.

Table 2

Volume Fractions of Nanoparticle and Interfacial Area for PA/SiO_2 Nanocomposites

Concentration of SiO_2	# of Particles in 20 μm^3	Fraction of SiO_2 Volume to Total Volume	Fraction of Particle and Interface to Total Volume
2 wt. % SiO_2	174	0.89%	3.9%
4 wt. % SiO_2	349	1.79%	7.9%
6 wt. % SiO_2	524	2.68%	11.8%

3.2.2 Exploring the Particle-Polymer Interfacial Mechanics of Plasma Etched Nanocomposites with SEM Characterization

The SEM image shown on in Figure 28 A is from a 6 wt. % PA/SiO_2 coated slide sample that was plasma etched with a 50-psi oxygen carrier gas flow excited by 50 W of RF power for a 1-minute duration. Because the reactions between the oxygen plasma and the polymer matrix can significantly weaken the C-C bonds in the polymer chains, the chemical etching mechanism is dominant, and volatile products are generated as a result [48, 125, 148]. In addition to this polymer bond weakening mechanism, the sample temperature can reach as high as 50 °C due to the continuous surface bombardment of reactive plasma species [125]. It is suggested that the combination of these effects could have weakened polymer bonding at the interfaces with SiO_2 particles in the sample and the mild thermal expansion / contraction of the coated slide surface can result in the de-bonding of the SiO_2 particles from the matrix. Most significantly, the SEM image appears to demonstrate the very mechanics of matrix confinement performed by SiO_2 particles in response to the combined chemical and thermal processes. Upon thermal expansion of

weakened interfacial polymer regions during the etching process, the polymer confinement mechanisms of the SiO_2 particles likely acted as crosslinks to temporarily impede thermal dimensional response from the bulk material [48]. Then, following sample etching and cooling, the imaging appears to demonstrate that a heterogenous stress state existed between the confined bands of polymer linking individual particles and other bulk regions of uninfluenced polymer. Figure 29 shows this heating-cooling effect on the sample surface, which forced plastic deformation of the confined regions and led to localized delamination of those regions from the bulk composite material. At the nano scale, this allowance for plastic deformation zones, filler de-bonding, and void growth is widely reported to contribute to enhanced fracture performance of the macro scale system [145, 149, 150].

The internal stresses induced by both particle-polymer and coating-substrate interfaces subject to thermal expansion and contraction are highly complex, but the development of localized deformation via strain bands during the de-bonding of particle reinforcement is reported in other literature [151, 152]. A finite element model was created using the static structural module in ANSYS™ Workbench to demonstrate the formation of heterogenous strain band networks in composite materials subject to uniaxial tension. The PA/SiO_2 composite thin plate model on the Figure 28 B is constructed of 27,550 elements and 114,902 nodes, with multizone hex dominant meshing on both particle reinforcement and the matrix material. The model contains anisotropic Silicon particles of 62.5 µm and 125 µm diameters, with a PA 6 matrix material. A fixed boundary condition was applied on the bottom surface and 25 N of axial tension in the y-axis was uniformly distributed along the top face. The mapped equivalent

elastic strain shows circumferential patterns of lower strain bands that stretch outward from the perfectly bonded interfaces and develop into a network of polymer confinement between particles. Individual particle de-bonding is likely a result from the adjacent higher magnitude regions of strain, which extend in the direction of uniaxial tension from interfaces. It is critical to note the limitations of the finite element model, as it is scaled 17× larger than the actual PA/SiO_2 nanocomposite matrix and the mechanisms dominating interfaces of particle-polymer composites at this microscale are still a topic of research [151]. Even though many different continuum mechanics models developed for microcomposites have been used to predict the elastic modulus of polymer nanocomposites with significant differences in the physical sizes of fillers, this model can only reliably be used to visualize and compare deformed structures with mapped regions of strain in particle reinforcement [81, 99]. The chemical and mechanical phenomena that characterize SiO_2 nanoparticle bonding to the polyamide host are significantly more complex than mechanics observed in both microcomposites and the perfect bonding used in the model. However, both the finite element model result and the SEM image shown in Figure 28 demonstrate similar structures of strain heterogeneity existing in well bonded, rigid particle reinforcement of stressed matrices. The localization of plastic deformation demonstrated here and the subsequent relaxation of the matrix stress state that can occur are critical factors repeatedly attributed to improved mechanical performance in polymer nanocomposite materials [48, 58, 67, 139, 142].

Figure 28

Static Structural Simulation of Plasma Etched Thin Film

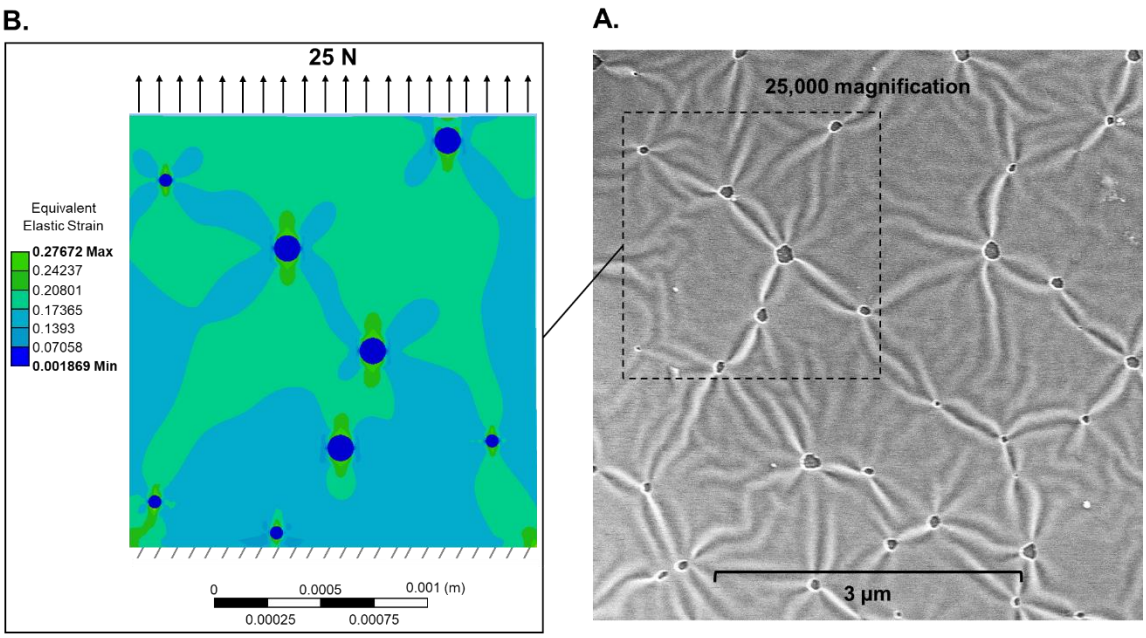

Note. SEM imaging of plasma etched 6 wt. % PA/SiO_2 sample (right) with ANSYS™ Workbench model of a scaled 2D particle reinforced matrix in uniaxial tension (left).

Figure 29

Effect of Plasma Etching Cycle on PA/SiO_2 Matrix

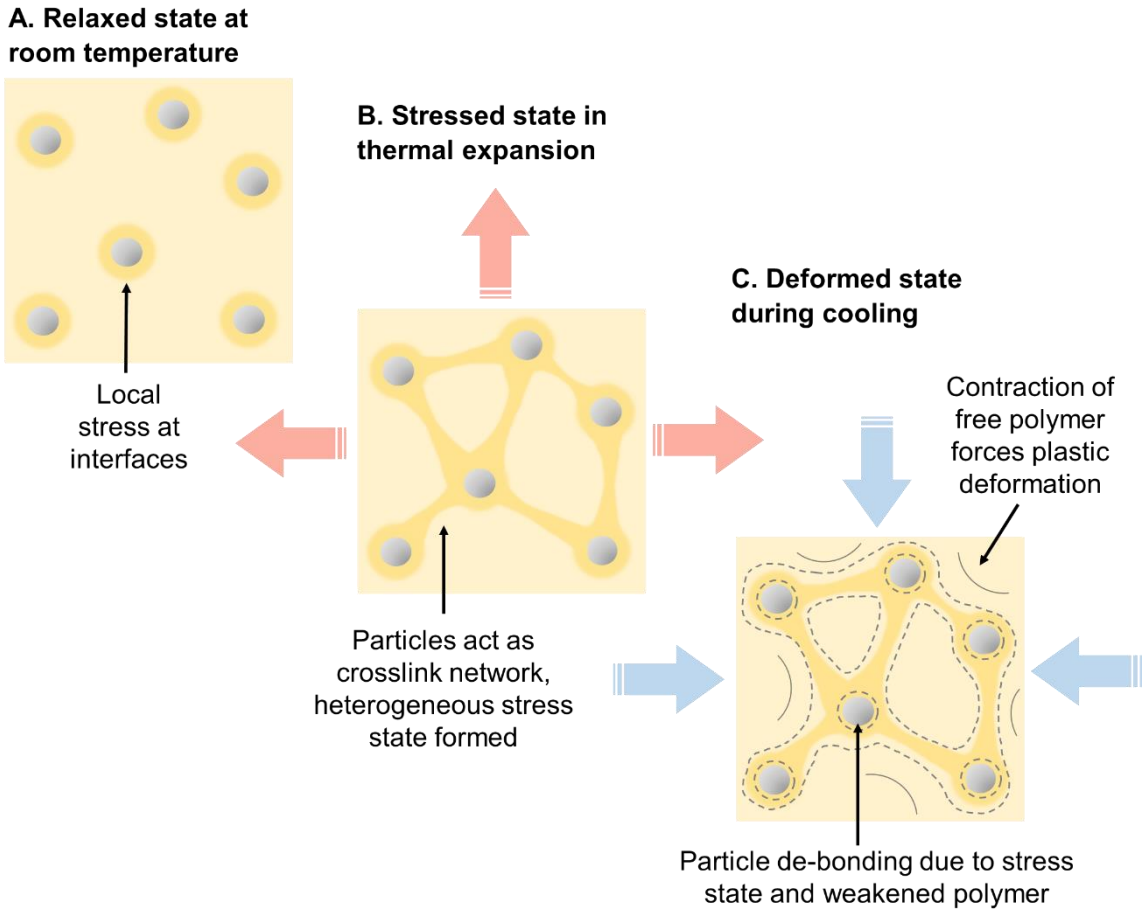

Chapter 4

Characterization of Dielectric Properties

4.1 Experimental Techniques for Evaluating Dielectric Performance

Despite evidence that the proposed PA/SiO_2 nanocomposite insulator demonstrates exceptional thermomechanical stability without the decrement of mechanical properties, its bulk electrical breakdown characteristics are the most significant parameter of electrical engineering design in this study [153]. Polyamide based coating materials are well known for their excellent dielectric properties, but introducing any defects such as particle fillers of dissimilar materials into a bulk polymer can negatively impact the resulting dielectric strength [48, 61, 62, 67]. A critical parameter in implementing this truly multifunctional coating material is leveraging its dominant particle-polymer interfacial properties to maintain adequate dielectric breakdown performance of the bulk material. Other studies have demonstrated that because the charge transport characteristics of a material are closely related to morphology, its dielectric breakdown properties can be tailored by the addition of nanoparticles [94, 153-155]. The complex morphology of a polymer nanocomposite combines with factors such as sample dimensions, temperature, pressure, humidity, and mechanical stress to influence the governing mechanisms of electrical failure [153, 156]. Therefore, dielectric tests in the cryogenic operating conditions of HTS cable systems, in multiple fluid mediums and in different cured coating forms were required for a thorough characterization of the PA/SiO_2 nanocomposite.

4.1.1 Dielectric Testing in Ambient and LN_2-Cooled Air Conditions

The thin film DC dielectric breakdown tests conducted here used an electrode system to electrically stress samples with the application of an increased direct voltage until the current passed through the sample via internal breakdown. The dielectric breakdown strength, a function of the breakdown voltage and sample thickness (in kV/mm), is the resulting acceptance criteria used to evaluate the dielectric properties of the material [156, 157]. 25 mm × 25 mm free standing thin film samples with an average thickness of 20 μm were cut from the surfaces of glass slides for ease of repeatable testing in large quantities and comparative study between multiple weight percent concentrations of SiO_2 particles.

Figure 30 details the room temperature (300 K) and LN_2-cooled cryogenic temperature (92 K) setups for testing in standard atmospheric air conditions. Conducted in accordance with ASTM-D3755 standards, the tests involved placing a thin film sample between two brass electrodes [156]. To mitigate inaccurate breakdown voltage measurements caused by 1) contact surface air gaps, 2) foreign debris on the contact surfaces, or 3) moisture accumulating on the contact surfaces, the top electrode placed a 50 gram mass on the sample to ensure a firm electrode-sample contact and both electrode surfaces were polished between tests. The pairs of 6.35 mm diameter electrodes loaded with samples were housed in 3D printed fixtures for efficient and repeatable testing processes. In accordance with the ASTM standard, a Vitrek 955i high potential (hipot) tester applied voltage across the sample which increased at a rate of 500 V/s, until a 50 mA current was detected by the return electrode, signifying the sample had internally failed [156]. The function was terminated and the hipot electrode was discharged at 10

kV if no failure occurred. Due to the 3 kV/mm dielectric strength of dry air, this safety mechanism ensured that arcing through the ambient air could not occur at lower failure voltages with the selected sample dimensions [158]. In addition, the 50 mA return electrode current measurement setting was selected as a medium between unwanted tripping due to low current partial discharge and higher current causing excessive damage to the sample during failures [156]. Following all dielectric failures, the samples were visually inspected to verify the presence of a pin hole where the breakdown occurred.

Shown in Figure 30, the room temperature benchtop testing fixture incorporated a single electrode pair for testing individual samples. The fixture was safely isolated from unwanted shorts via a rubber mat and a Plexiglass™ shield. A liquid nitrogen dewar probe was implemented to test samples in cryogenic temperature conditions, where four 304 stainless steel electrode pairs were incorporated for testing multiple samples in one cycle. A type-K thermocouple was located at the end of the dewar probe. After measuring the level of LN_2 in an open dewar, the apparatus was lowered until the location of the samples was less than 3 cm from the liquid surface, without actual immersion. The dielectric test was initiated on each of the four samples when the thermocouple reading of sample temperature reached a quasi-steady state of 92 K after roughly 30 minutes. A grounding wire was bolted into the LN_2 dewar and connected to the safety ground terminal on the hipot tester, effectively isolating the system.

Figure 30

Air Dielectric Testing of PA/SiO_2 Thin Films

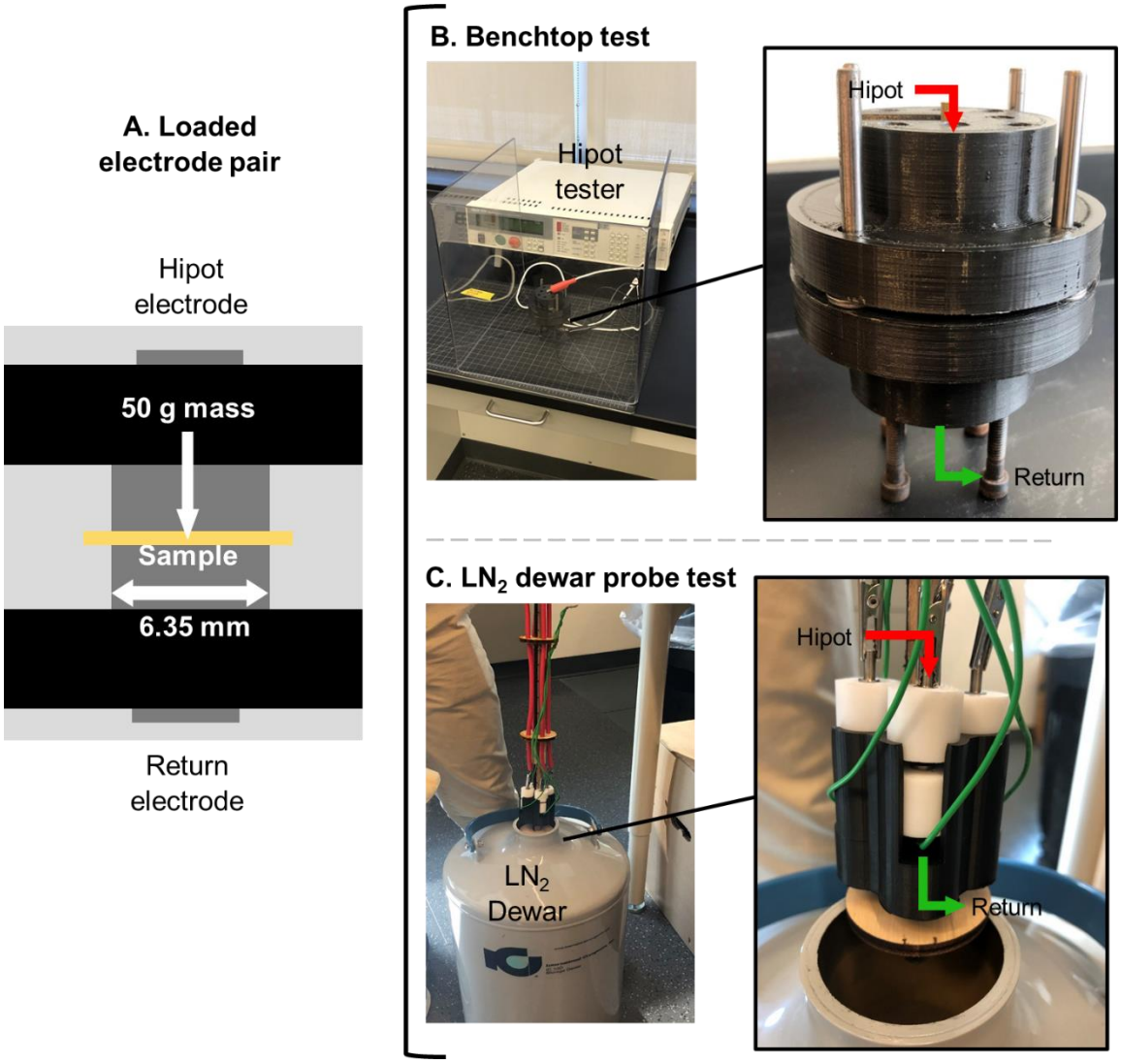

Note. 300 K and 92 K air dielectric breakdown test setups for free-standing thin films.

The Figure 30 apparatus can be implemented to characterize the property relationships between dielectric strength, weight percent concentration of SiO_2 particles, and temperature. However, the free-standing thin film samples used for convenient

preliminary testing do not accurately reflect the additional mechanical stresses that can be induced in thin coatings during their curing on cylindrical substrates [156]. Since the mechanical condition influences breakdown behavior, additional testing is required to characterize the dielectric properties of the nanocomposite material as manufactured on cylindrical conductors in HTS power transmission cables [159]. Figures 31 and 32 show the dielectric test setups for PA/SiO_2 electrode samples in room temperature (300 K) and LN_2-cooled cryogenic temperature (92 K) ambient air environments. The 6.35 mm diameter coated stainless steel dowel samples serve as the return electrode for the testing. They are intersected by a perpendicular hipot electrode, which increases the applied direct voltage until the current passes through the coating. The coating thickness at the point of dielectric failure is determined by halving the difference in measured diameters between the coated and uncoated surfaces of the electrode samples. Following assembly of the fixtures shown, the dielectric tests are conducted in accordance with ASTM-D3755 standards using the same conditions as described in the thin film tests.

Figure 31

300 K Air Dielectric Testing of PA/SiO_2 Coated Electrodes

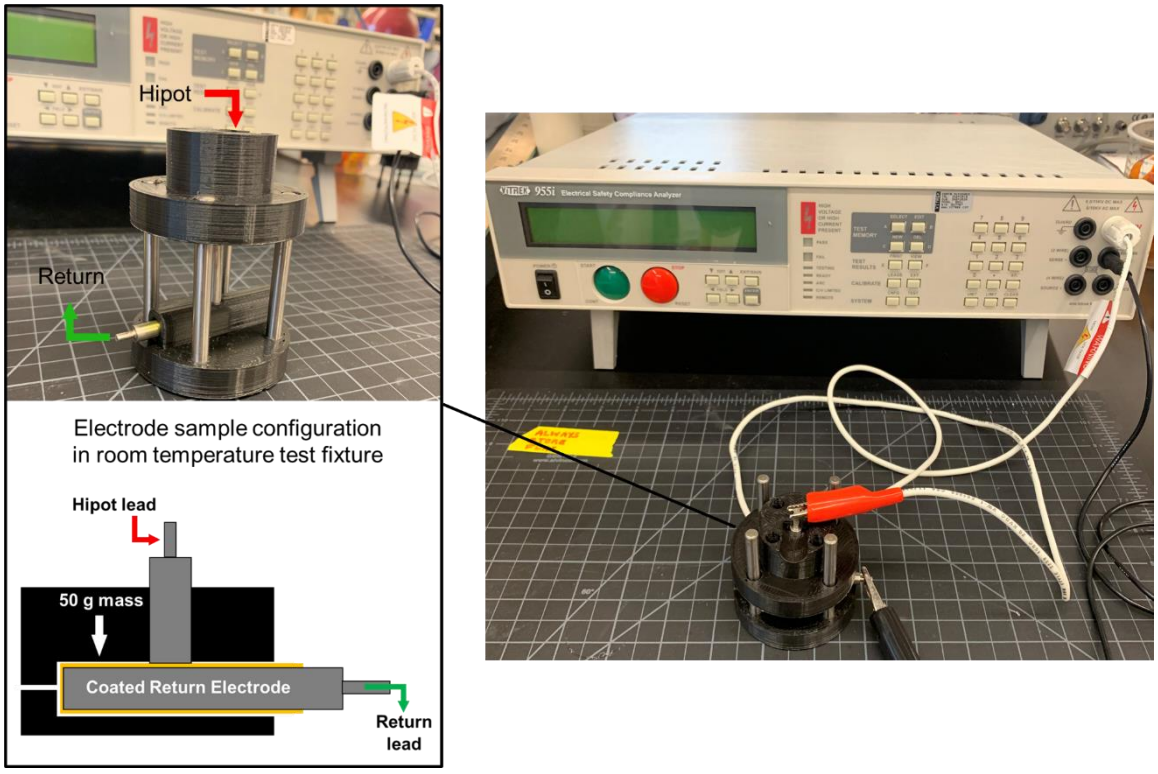

Note. 300 K air dielectric breakdown test setup for single coated electrodes.

Figure 32

92 K Air Dielectric Testing of PA/SiO_2 Coated Electrodes

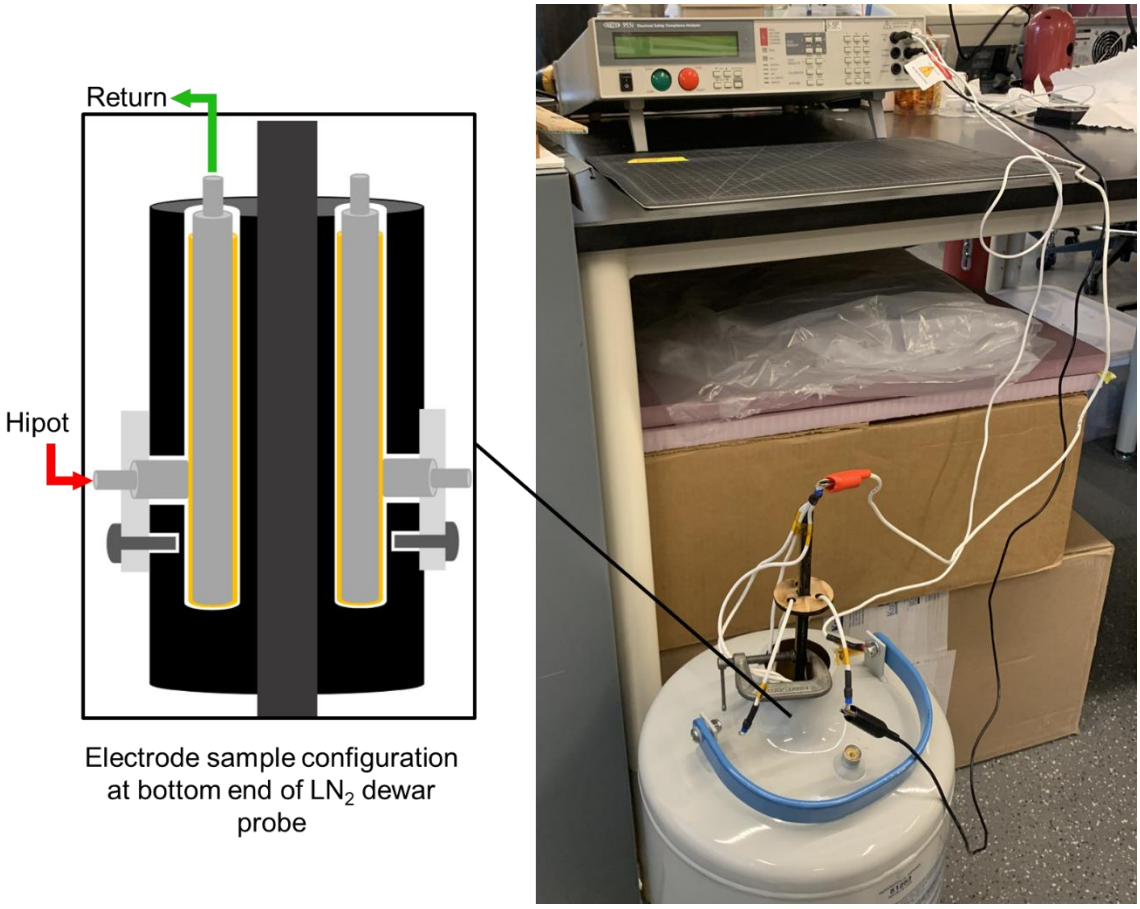

Note. LN_2 dewar probe containing sets of 3 coated electrodes for 92 K air dielectric breakdown testing.

4.1.2 Cryogenic Gas Helium Environmental Test Chamber Development

Due to the dependency of insulation material's dielectric properties on factors such as the ambient fluid medium and temperature, characterization tests generally must be conducted under the same operating conditions as the cable system [156, 160]. In addition, the interface between the solid insulating material and the fluid medium can act as the weak point in an electrical insulation system, resulting in flash overs. Therefore, a

cryogenic gas helium environmental chamber and novel testing system were developed in this study to conduct the DC dielectric testing from the previous section in the operating environment of GHe-cooled HTS transmission cable systems. The grand engineering challenges found in the design, fabrication, and operation of the cryogenic helium cooling system implemented for high-voltage dielectric testing of PA/SiO_2 thin films will be presented in the following sections. As a general overview, the development of cryogenic test systems requires cryostat thermal design, pressure vessel mechanical design, system construction, electrical wiring design, unique temperature measurement techniques, and integration of the material testing system into the environmental envelope [161, 162].

A cryogenic helium gas refrigeration system was loaned for the purposes of this study from the U.S. Naval Surface Warfare Center, Philadelphia Division. Therefore, the conceptual design of the cryogenic dielectric testing system was formed around the parameters and methods found in HTS transmission cable systems implemented on U.S. Navy vessels that used gas helium cooling in the 50 K operating range, charged from 100 to 150 psi [15, 16]. These charge pressures were selected due to the increased cooling capacity of cryogenic gas helium with pressure, but this is also conducive to avoiding unwanted shorts through the fluid medium around thin film samples during dielectric testing. Paschen's Law depicts a proportional relationship between fluid medium pressure and breakdown voltage above ambient pressure, where the maximum discharge distance for DC breakdown in a 100 psi, 300 K helium environment is just 1.5 mm [163, 164]. Therefore, the same thin film sample dimensions could be used in the gas helium testing as the ambient air testing, without concerns regarding unwanted shorts.

The primary challenge associated with the development of this experiment was the design of an environmental dielectric test chamber to pair with the performance of the available cryogenic helium refrigeration system. Shown in Figure 33 A, the cryogenic helium refrigeration system implemented a Gifford–McMahon (GM) closed loop cryo-cooler, which eliminates the costs of a continual liquid helium supply for experiments [73]. The cycle employs a gas helium compressor connected in series with to a cryogenic cold head [165]. The cold head contains a reciprocating displacer and rotary valve system that rapidly expand the circulating flow of helium gas, achieving cryogenic temperatures on its outer surfaces [165]. The Cryomech AL300 GM cold head shown in Figure 34 is implemented here and employs two stages [166]. The first stage reaches temperatures in the range of 40–80 K, serving as a thermal anchor for a radiation shield that surrounds the second-stage cold head, capable of achieving temperatures as low as 25 K [73, 162]. The refrigeration capacity curve of the GM cryocooler system is shown in Figure 34.

As shown in Figure 33, the end of the cold head in the GM refrigeration loop is mounted inside a vacuum insulation chamber, upon which a heat exchanger for coolant helium piping from an external 100 psi supply is fixed. A Sterling Cryogenics gas helium circulation fan shown in the Figure 33 and Figure 34 B is mounted in-line with the heat exchanger, providing a volumetric flow rate of 2 m^3/hr under a pressure head of 45 m, while operating at 300 Hz [167]. In this fashion, the circulation fan and heat exchanger system are capable of operating a 50 m long HTS transmission cable cryostat section at 150 psi in a closed loop [15]. For this experiment, the environmental test chamber shown at the right of Figure 33 was connected to the refrigeration system via Technifab vacuum jacketed flex hoses, providing cryogenic helium coolant flow to the dielectric testing

apparatus contained within. Two pressure relief devices, labeled R1 and R2 in Figure 33, vent the helium coolant supply at 150 psi and the vacuum spaces if any positive pressure enters them.

Figure 33

Cryogenic Helium Refrigeration System for Dielectric Tests

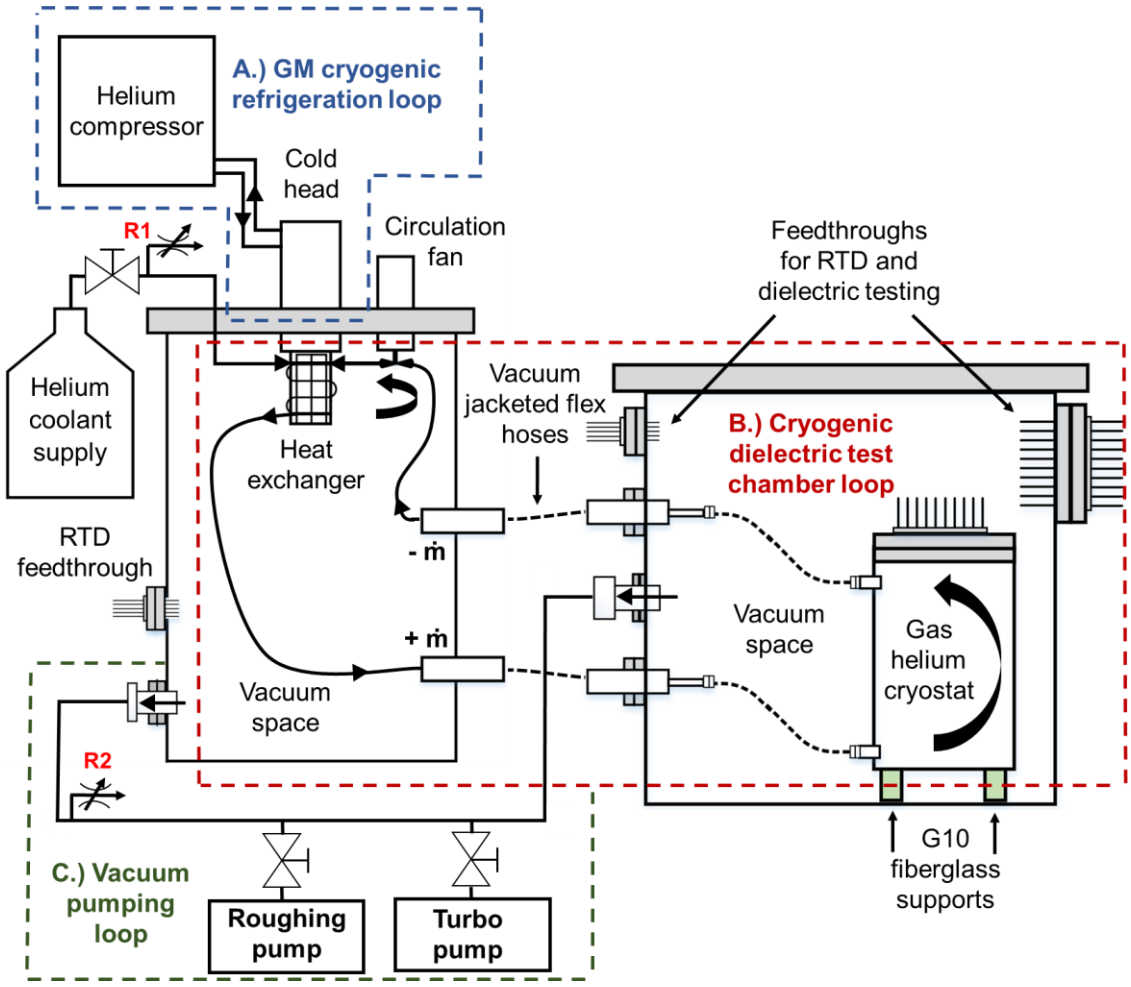

Note. Schematic of the cryogenic gas helium refrigeration system (left) and its integration with the environmental dielectric testing system (right).

Figure 34

Gifford-McMahon Cycle Refrigeration Cycle

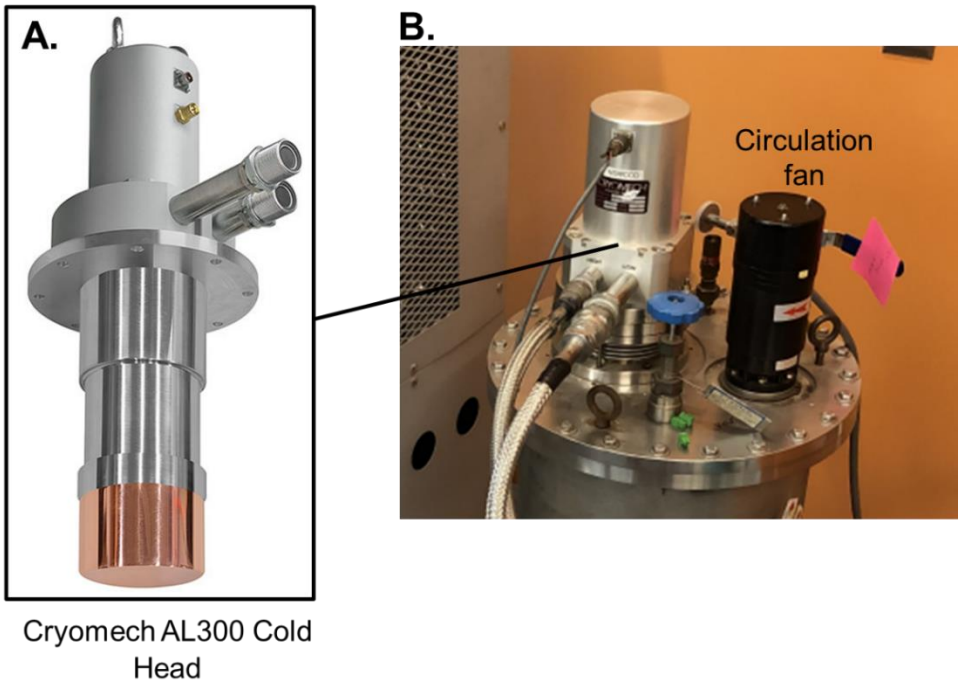

Note. Cryomech AL300 cold head (A) used the cryogenic gas helium refrigeration system (B) [166].

The main functionality of the two cryostat chambers shown in Figure 33 is to minimize the thermal heat loads from external ambient temperatures that would otherwise exceed the refrigeration capacity of the cryocooler. The chambers also needed to incorporate penetrations to permit the transfer of helium gas coolant, wiring for the dielectric test system, and temperature measurement wiring. Gas convection and conduction, the largest components of heat load on the system, are effectively eliminated by using a vacuum space as a high-performance insulator [168]. Oil-sealed mechanical pumps can significantly mitigate the thermal conductivity of the gas by easily producing

a vacuum level of 1×10^{-3} torr, but operating in the sub-LN_2 temperature range requires turbomolecular pumping capabilities that handle the gas loads due to water desorption from chamber walls at significantly lower pressures [168]. Pressures in the range of 1×10^{-7} to 1×10^{-8} torr are required to assume negligible heat is transferred by the residual gas [169]. For the refrigeration chamber, these vacuum levels are achieved via a Leybold Turbolab^{TM} 90 roughing and turbomolecular combined pumping station, shown in Figure 33 C, which pumps the 118.6 L volume of the refrigeration chamber to an ultimate pressure of 6×10^{-8} torr. When pumping the 207.6 L volume of the dielectric test chamber, an additional Welch 8917 oil-sealed mechanical pump with an ultimate pressure of 1×10^{-4} torr was added to the system to improve its pumping capacity in the higher-pressure roughing range.

In addition to eliminating the sources of through-gas heat transfer, thermal conduction from the ambient environment is mitigated by using low conductivity solid connections to the cryogenic environment and thermal radiation is mitigated using multilayer insulation (MLI) reflective blankets [161]. During the conceptual design process of the environmental test chamber, the conductive and radiative heat loads were determined and compared with the Figure 35 refrigeration capacity curve of the cryocooler, ensuring that cryogenic operating temperatures could be achieved. The total conductive heat load, a function of cross-sectional area, length, and material thermal conductivity, was calculated using Equation 3 for various connections [169].

Figure 35

Cyromech AL300 Capacity Curve

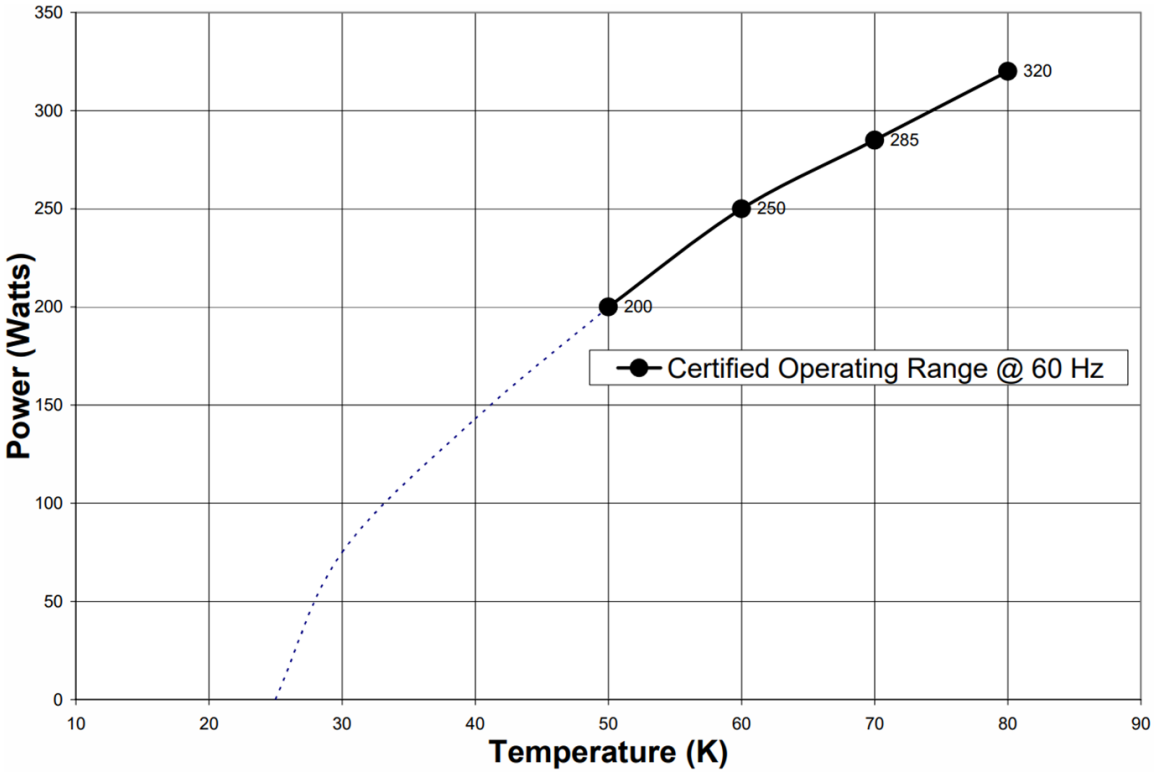

Note. Refrigeration capacity (W heat load) versus cooling temperature for the Cryomech AL300 [166].

$$H = \frac{A}{L}\int_{T_1}^{T_2} k\, dt \tag{3}$$

Where:

H = conductive heat load (W)

A = cross sectional area of the conducting element, cm^2

L = length of the conducting element, cm

k = thermal conductivity, W/cm K

T_1 = the colder temperature, K

T_2 = the warmer temperature, K

Detailed in Appendix E, the integrals of thermal conductivity over the operational temperature gradient of the environment test chamber were determined by plotting experimental values and estimating the resulting area graphically [73, 170]. The sources of total conductive heat load in the design of the environmental chamber were G10 fiberglass rods supporting the environmental test chamber (3.38 W), 18 AWG wiring required for the dielectric test system (3.42 W) and bayonet style connections for gas helium transfer between the chambers (45.48 W). The design of the low conduction bayonet style connections is detailed in Figure 36, which maximizes the length of the conductive heat transfer path and minimizes its cross section, allowing high efficiency transfer of cryogenic fluids.

Figure 36

Bayonet Connector Equipped Conflat Flanges

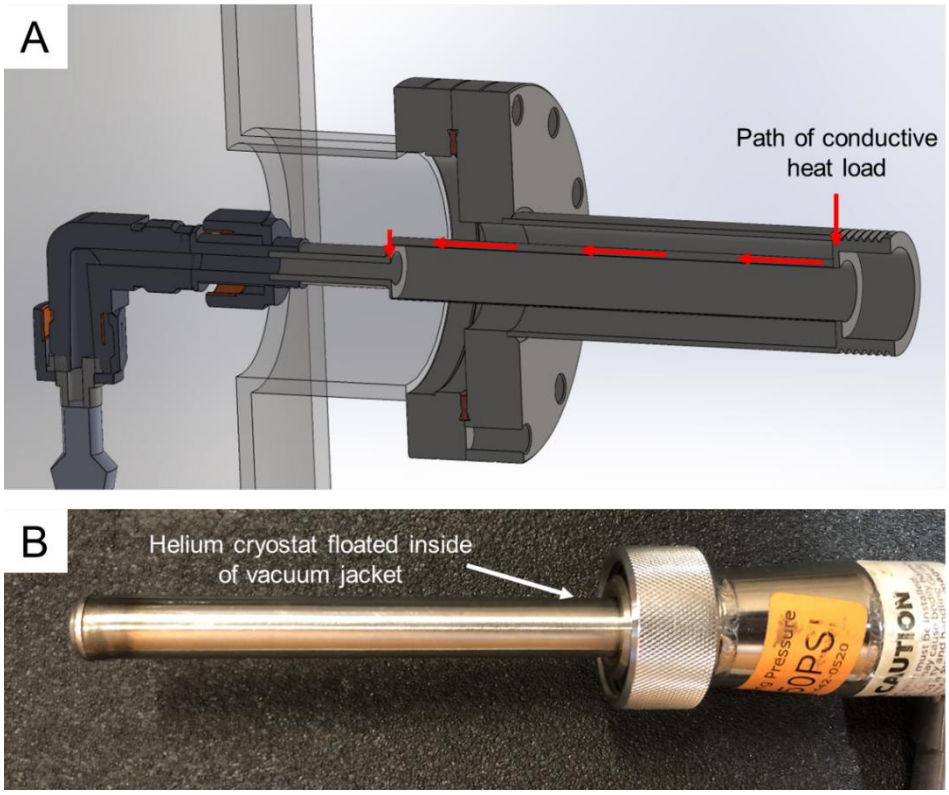

Note. Design of female (A) and male (B) Technifab bayonet connections for low conduction gas helium transfer into the environmental test chamber.

In order to reduce the heat load due to radiative heat transfer, cryogenic systems typically implement MLI, which uses stacks of low-emittance metalized sheets paired with low-conduction spacers [171]. The spacers layers in the MLI prevent the low-emittance shields from directly contacting, but they themselves contact the aluminized layers, allowing moderate levels of conduction through the insulation stack [171]. Therefore, the MLI performance is modeled by the Equation 4, as a function of conductive and radiative heat flux across the insulation stack with the number of two-part

layers selected [169, 171, 172]. Using the values of the aluminized Mylar® and 100% polyester mosquito netting obtained for in-house fabrication of custom MLI blankets, Equation 4 was then plotted as a function of number of MLI layers in Figure 37. Based on the plot, in order to achieve adequate thermal insulation and feasible manufacturing time, a design parameter of 15 MLI layers was selected for the custom insulation blankets covering the cryogenic piping and pressure vessel surfaces inside the environmental test chamber. Various methods for in-house MLI fabrication were studied and the blankets shown in Figure 38 were developed by fastening individual layers together with polyethylene clothing tag fasteners [173, 174]. As shown in Equation 4, thermal conduction through the thickness of the MLI is highly sensitive to compression (increased MLI density) [171]. The clothing tag fasteners effectively bind the blankets together, while allowing significant freedom of individual layers to move along their length without being compressed.

$$q = q_c + q_r = \frac{C_c N^{2.56} T_m}{n}(T_h - T_c) + \frac{C_r \varepsilon_o}{n}(T_h^{4.67} - T_c^{4.67}) \quad (4)$$

Where:

q = total heat flux transmitted through the MLI (mW/m^2)

q_c = conductive heat flux transmitted through the MLI (mW/m^2)

q_r = radiative heat flux transmitted through the MLI (mW/m^2)

C_c = conduction constant

C_r = radiation constant

T_h = hot side temperature (K)

T_c = cold side temperature (K)

T_m = mean MLI temperature (K)

ε_o = MLI shield-layer emissivity at 300 K

N = MLI layer density (layers/cm)

n = number of facing pairs of low-emittance surfaces in the MLI system

Figure 37

Total Heat Flux Transmitted Through Layers of MLI

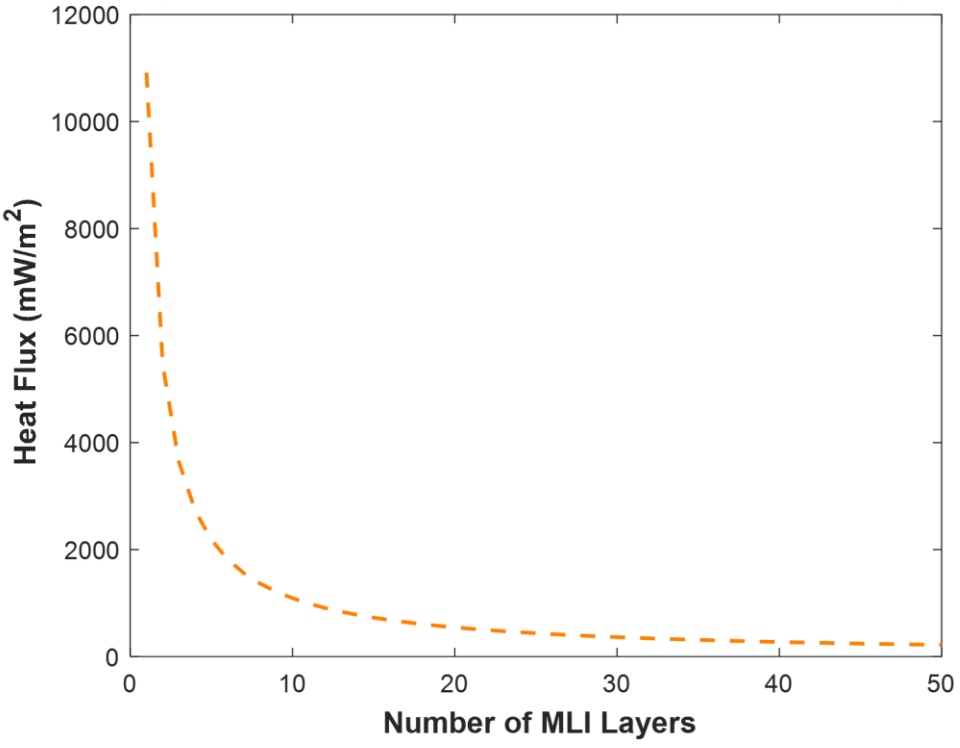

Note. Heat flux (mW/m^2) plotted as a function of the number of layers in an aluminized Mylar and polyester MLI blanket, obtained from Equation 4.

Figure 38

Fabrication of Multi-Layer Insulation (MLI) Blankets

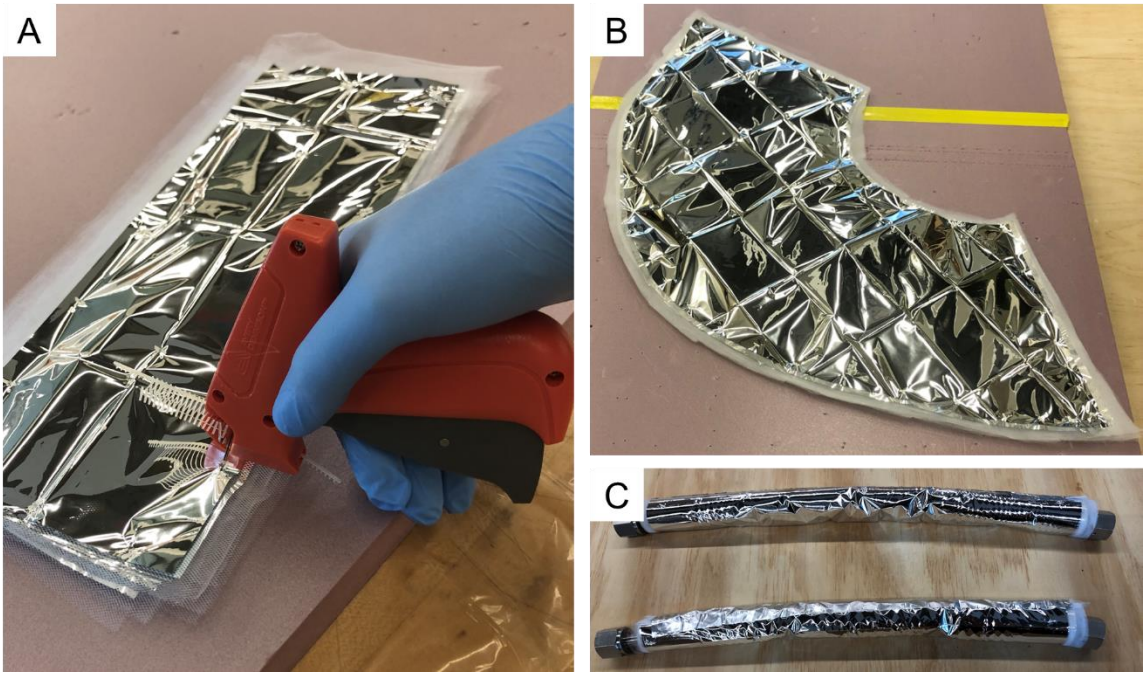

Note. Aluminized Mylar and polyester MLI blanket fabrication (A) and application for the cryogenic pressure vessel (B) and gas helium transfer hoses (C).

The total heat load due to conduction of the environmental test chamber on the cryogenic refrigeration system is 52.28 W. Convective and through gas conductive heat loads can be considered negligible, as long as acceptable ultimate vacuum pressures are achieved [169]. In addition, the design of MLI insulation blankets outlined above can theoretically achieve a > 90% reduction in radiative loads from the external ambient environment. Finally, the actual available heat capacity of the cold head is lower than the values recorded in Figure 35, due to potential conductive losses in its mounting design or in the internal piping of the refrigeration chamber. Considering these factors, the system leaves adequate margins to successfully test in the operating environment of GHe-cooled

HTS cables, with a reported 225 W of available cooling capacity at a helium temperature of 55 K.

Following this conceptual thermal design process, the physical CAD model shown in Figure 39 was developed for the system. A custom configured vacuum insulation chamber for the test system was designed in-house and fabricated by an outside vendor. The chamber is constructed of rolled 304 stainless steel plate, incorporating a configuration of 6 external ports for helium gas transfer, vacuum pumping, temperature sensor wiring, dielectric test wiring to the cryostat, and user access to the system. Cryogenic helium piping is completed with Swagelok VCR® fitting equipped flex hoses, which are rated for cryogenic applications where both internal positive coolant pressure and an external vacuum environment is required [175]. Access to vacuum ports and cryogenic spaces is provided by 304 stainless steel ConFlat (CF) flanges with copper gaskets rated to the ultra-high vacuum (UHV) range. The large copper wire seal flange at the top of the vacuum chamber permits easy access to the cryogenic pressure vessel for loading and unloading samples during testing. MLI blankets cover the inner pressure vessel and all through penetration paths to minimize radiative heat loss. A pressure relief device set to 20 psi is connected to the vacuum pumping line, as additional precautions must be taken when operating positive pressure devices inside of a closed, unrated vacuum chamber. Finally, a Penningvac Transmitter PTR 90 N vacuum gauge uses both the cold cathode ionization principle and a MEMS-Pirani sensor to effectively measure vacuum pressures down to the UHV range [176].

Figure 39

CAD Model of Cryogenic Helium Dielectric Test Chamber

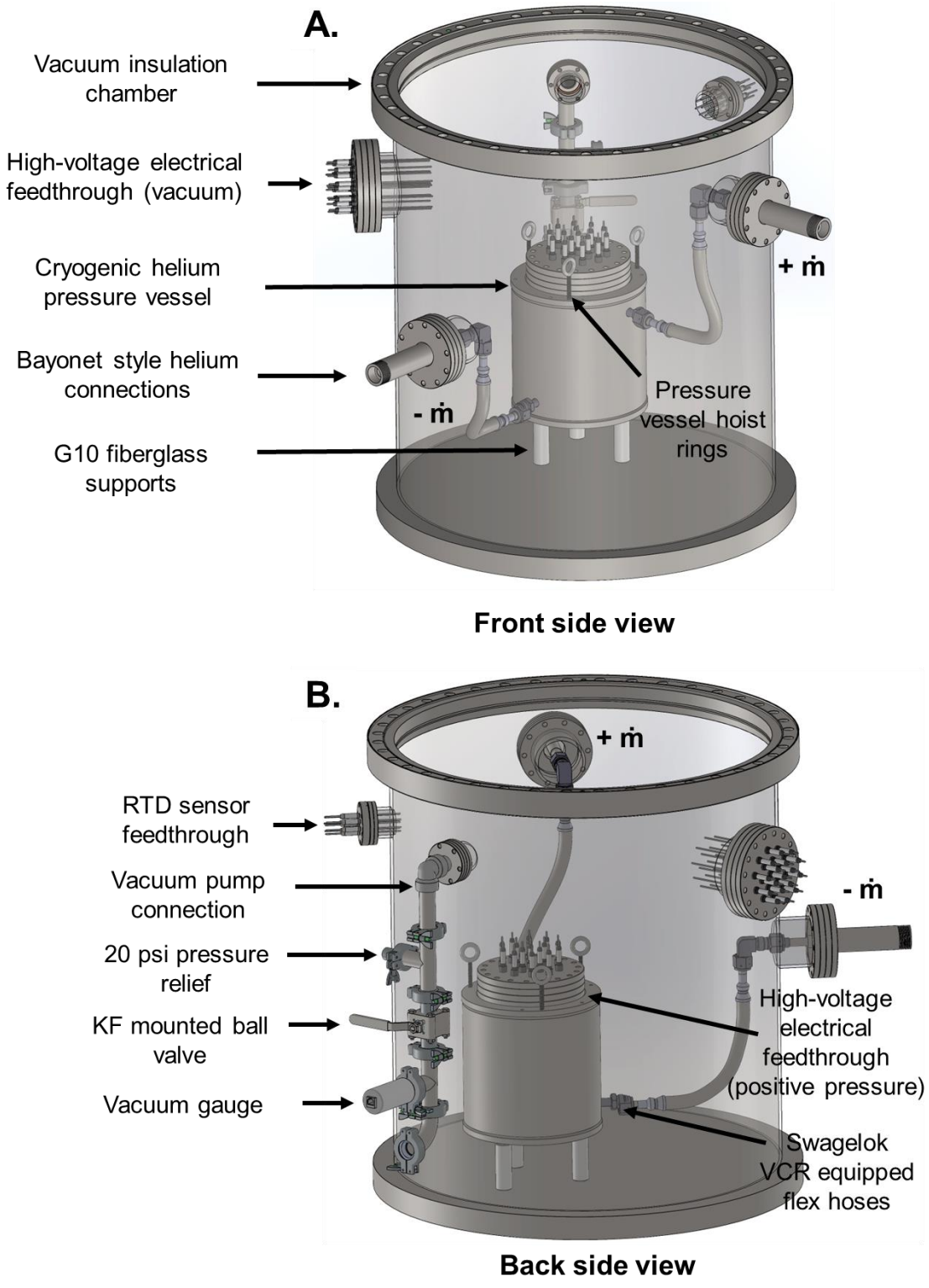

The cryogenic environmental pressure vessel contained within the vacuum chamber is a 304 stainless steel pipe weldment equipped with VCR® connections for helium circulation and a 6.75” diameter ConFlat flange port for access to the dielectric test system (See Figure 40). Due to their increases in strength while maintaining ductility and impact toughness at cryogenic temperatures, the wrought austenitic stainless steels selected for construction of this system are used extensively for low temperature equipment [177]. The pressure vessel design calculations shown in Appendix F determined the hoop and longitudinal stresses in the chamber wall, as well as the average shear stress along the gas tungsten arc welds (GTAW) for the flat end plates [178]. Based on the selected dimensions, the maximum stress component (τ average = 41.3 MPa) gave the vessel a design safety factor of 5 while operating at 150 psi. The Grade 8 Steel, 5/16”-24 thread hex bolts selected for use with the ConFlat access flange also provided a safety factor several orders of magnitude greater than required for these operating conditions. Despite these calculations, a major design challenge for the access flange was created by the requirement for vacuum service under simultaneous cryogenic positive pressure. Reputable manufacturers who can provide components that are rated for vacuum service, and are either ASME B31.3 listed or have a published maximum allowable working (positive) pressure currently do not exist [179]. Based on limited reports of ConFlat flanged fittings implemented as unlisted components in pressure / vacuum systems for other cryogenic applications, it was determined that the system could undergo additional hydrostatic pressure testing following welding and assembly to verify its safety for use [179].

Figure 40

Image of Cryogenic Helium Dielectric Test Chamber

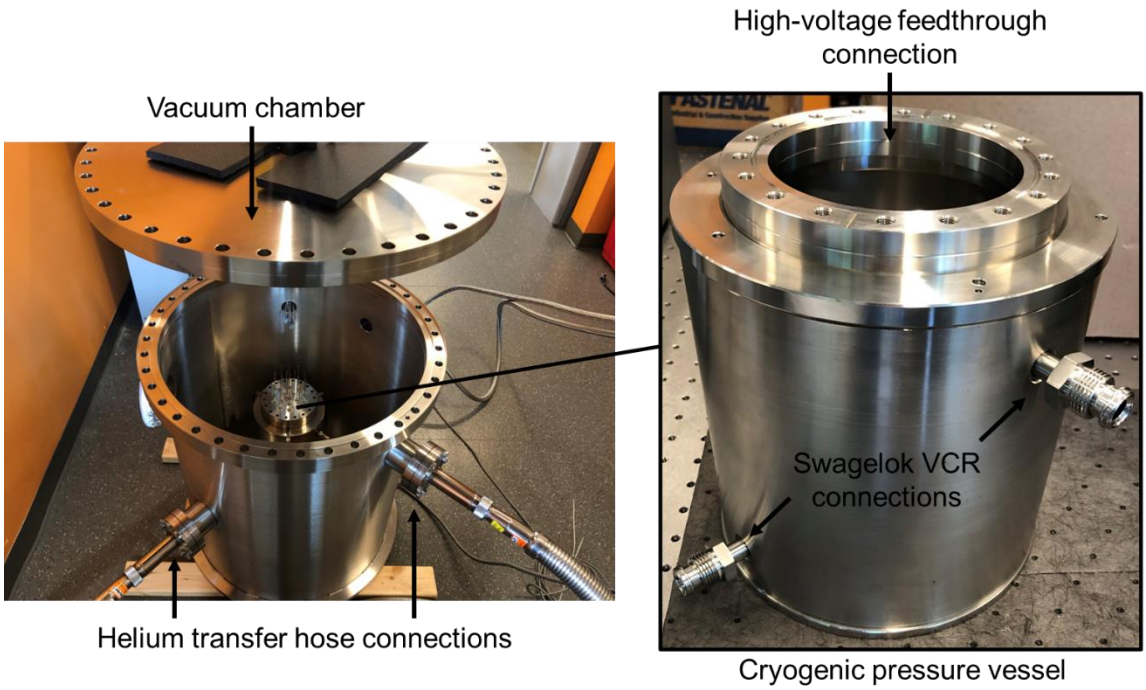

Note. Cryogenic pressure vessel contained in a vacuum insulation chamber for gas helium cooled dielectric tests.

The hydrostatic pressure testing to ensure the safety of the pressure / vacuum system with a ConFlat flange mounted electrical feedthrough was conducted in accordance with ASME Section VIII Division 2 code [180]. The hydrostatic test pressure of the system shown in Figure 41 was 1.43× the maximum allowable working pressure (MAWP) or 150 psi. The system pressure was raised gradually until the designated test pressure was achieved and this was maintained for 10 minutes before inspection for any leaking [180]. After successful inspections, these components were heated in a vacuum

furnace at 100 °C for two hours to bake them out for vacuum service. Following all design, fabrication, assembly, and testing, the cryogenic helium dielectric test system is shown in Figure 42.

Figure 41

Hydrostatic Pressure Testing

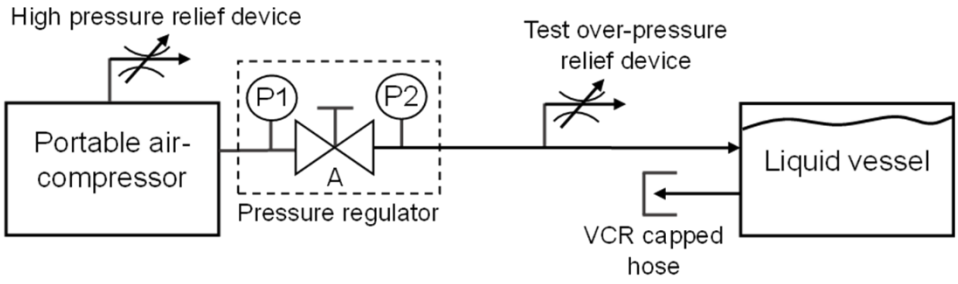

Note. Schematic of hydrostatic pressure testing completed on the cryogenic helium pressure vessel.

Figure 42

Assembly of Cryogenic Gas Helium Dielectric Test System

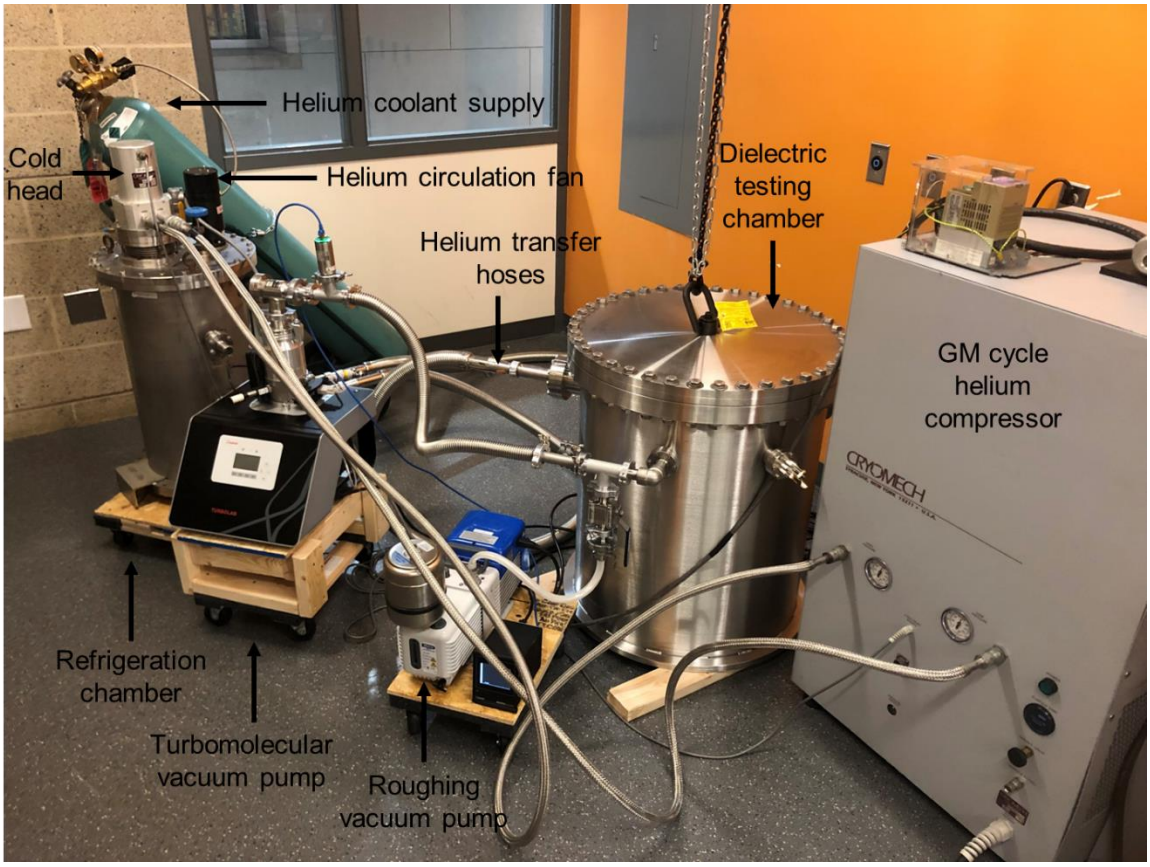

Note. Image of the assembled cryogenic dielectric testing system for PA/SiO_2 thin film samples.

4.1.3 Dielectric Testing in Pressurized Cryogenic Gas Helium Conditions

The two custom ConFlat flange-mounted, high-voltage electrical feedthrough assemblies for this system were designed in-house and fabricated by outside vendors, enabling a dielectric test rig to operate with the Vitrek 955i hipot tester for DC testing in the cryogenic helium environment. Figure 43 shows a simplified wiring schematic of the dielectric testing configuration, where the hipot leads for electrode pairs housing samples

use individual pins and all return leads share a common pin. In this manner, the external hipot tester could remain connected to a single return pin on the vacuum feedthrough while switching to different hipot pins to test different samples. Ground connections to the hipot tester are made on the walls of the cryogenic helium pressure vessel and vacuum chamber for safety in the event of unwanted shorts during the tests. A Lakeshore Cryotronics Silicon Diode resistance temperature detector (RTD) is connected through a separate feedthrough flange for temperature measurement of the environmental chamber at steady state test conditions. It uses a four-lead measurement scheme, with an excitation current of 10 μA to eliminate potential measurement error due to lead wire resistances [181].

Figure 43

Wiring Diagram for Cryogenic Helium Dielectric Test Chamber

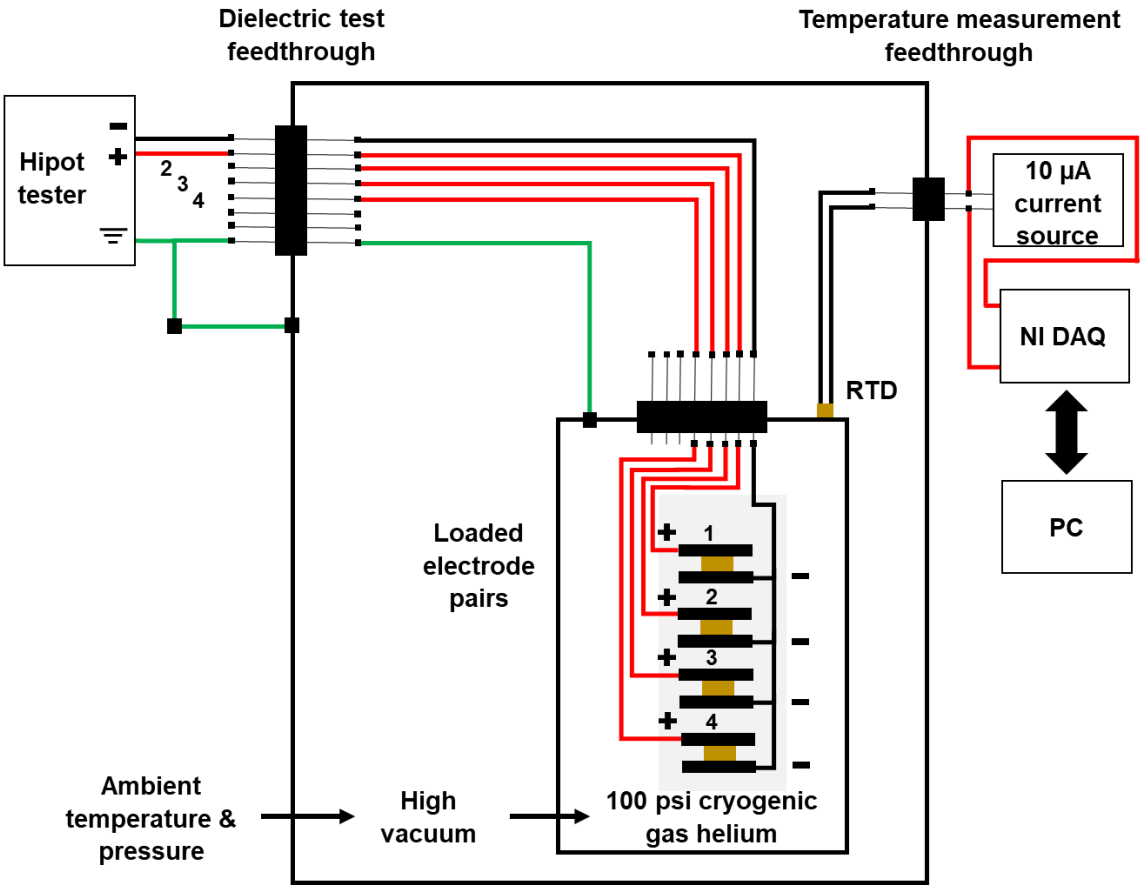

The dielectric testing fixture shown in Figures 44 and 45 was designed and fabricated in-house to incorporate stainless steel electrode pairs for testing 15 thin film samples in one cool-down cycle of the refrigeration system. The fixture contains stacked pucks with radial bores that house the pairs of electrodes. Return electrodes, located on the inner radii, meet in the center of the pucks for the common return wiring, while individual hipot electrodes are inserted and wired from the outside. Due to the

exceptional dielectric strength, thermal dimensional stability at cryogenic temperatures, and ease of machining operations, Teflon^{TM} polytetrafluoroethylene (PTFE) was the material selected for individual electrode housings and puck fixtures. 18 AWG silicone sheathed wires with stainless steel clip connections used for electrode and feedthrough pin wiring increased the ease of fixture assembly between tests. Figure 46 shows the wiring in the vacuum space from the pressure vessel to the external feedthrough where the connections to the hipot tester were made.

Figure 44

CAD Models of Gas Helium Dielectric Test Rig

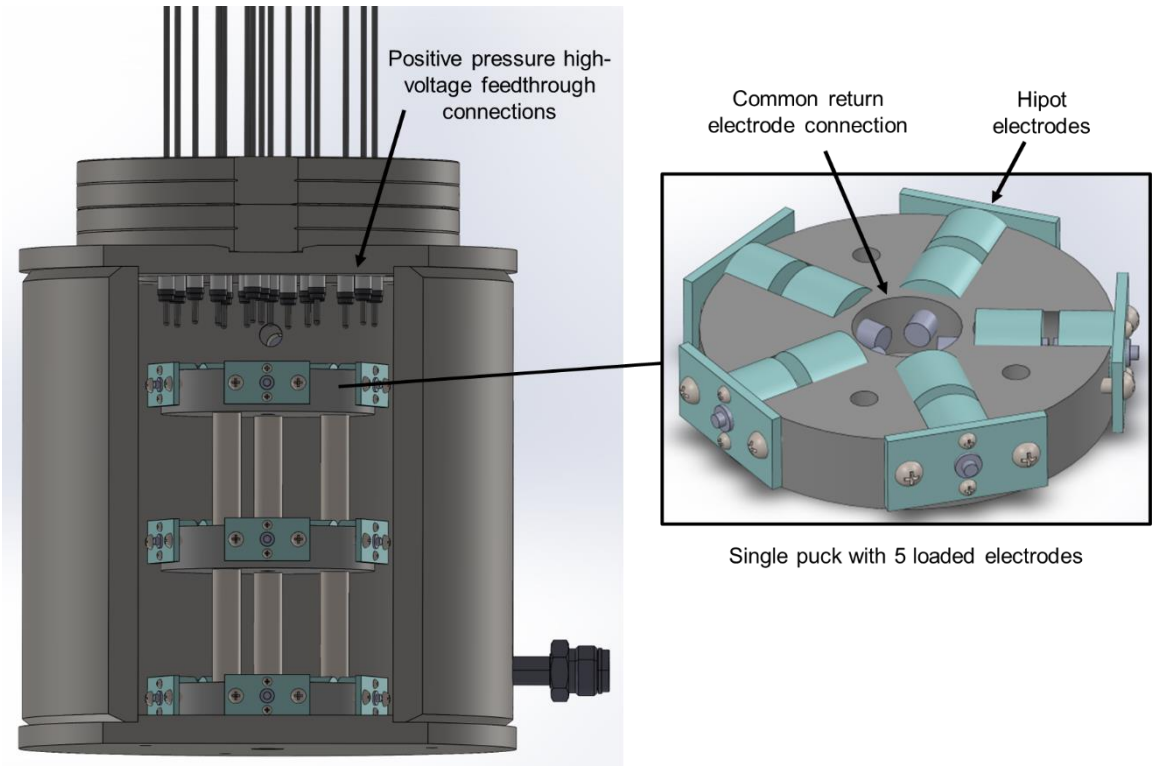

Note. CAD model of the dielectric testing rig within the cryogenic gas helium vessel.

Figure 45

Install and Wiring of Gas Helium Dielectric Test Rig

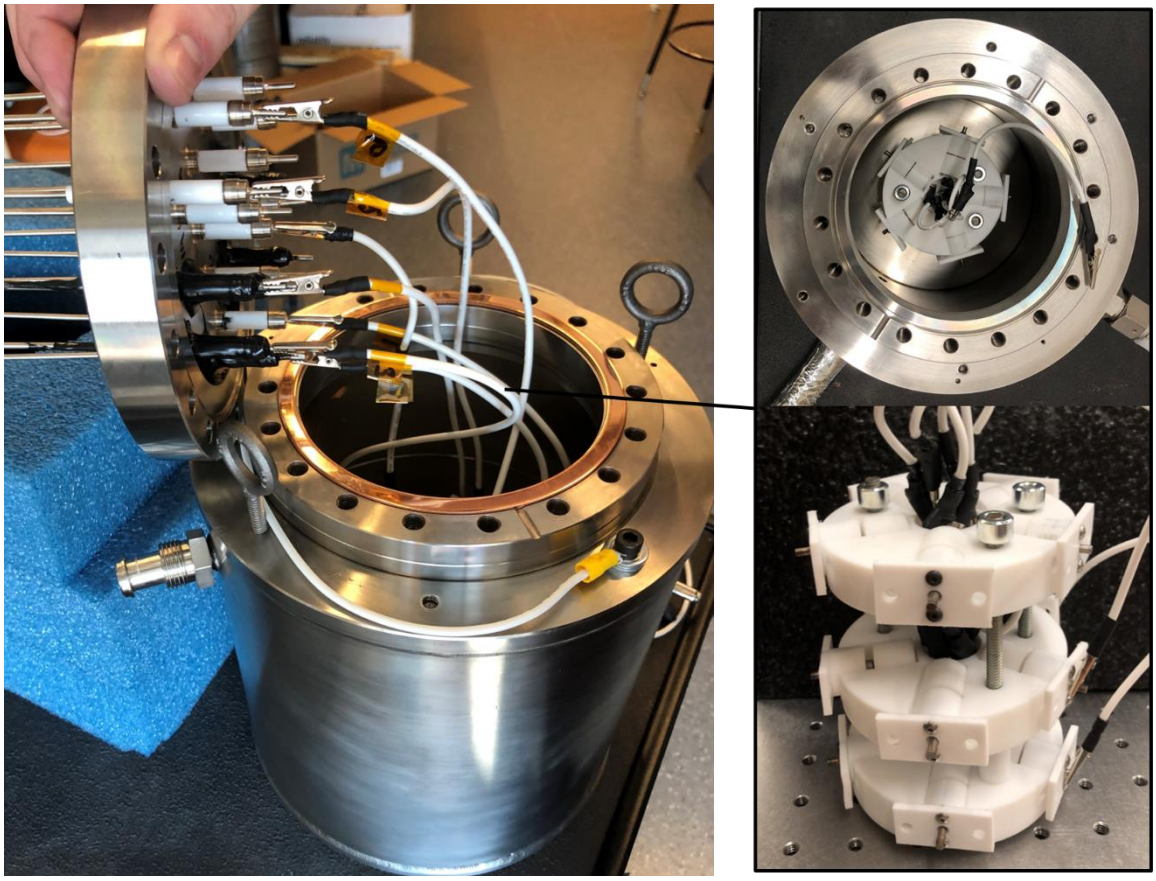

Note. Assembly and wiring of the cryogenic gas helium pressure vessel prior to a dielectric test.

Figure 46

Install and Wiring of Gas Helium Pressure Vessel

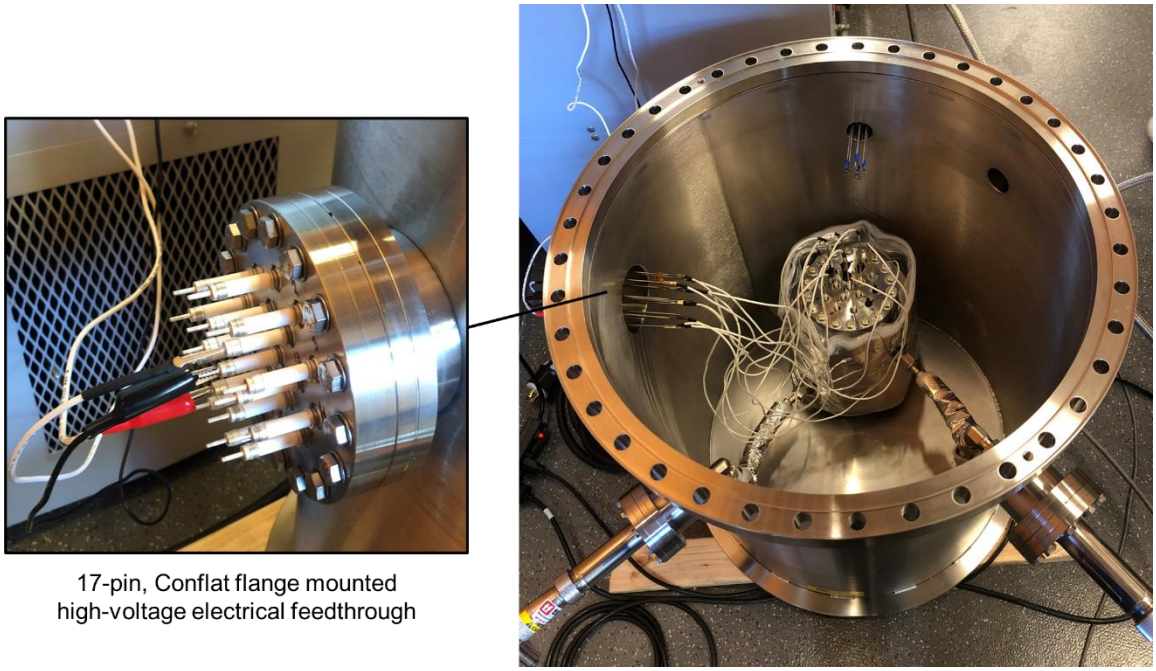

Note. Installation of wiring in the cryogenic dielectric test chamber and connection of hipot tester leads on the outer feedthrough.

4.2 Analysis and Discussion of Results from Dielectric Failure Analyses

The temperature dependent dielectric properties of PA/SiO_2 thin films in both ambient air and pressurized helium gas environments will be studied in this section. Establishing these tunable property relationships is an essential step for verifying this material's effectiveness as a dielectric coating in HTS transmission cable systems. Though the PA/SiO_2 nanocomposite has already demonstrated a level of multifunctionality in its mechanical properties, preventing excessive loss of its dielectric strength due to the introduction of silica nanoparticles is paramount for this application.

In addition, studying the dielectric strength of the coated electrodes adds yet another degree of assessment for the nanocomposite's thin coating application by recreating its mechanical condition in manufactured form on superconductors.

4.2.1 Establishing Tunable Dielectric Property Relationships for Thin Film Samples

The mechanisms of DC conductivity and charge transport in polymer-based nanodielectrics are still far from being completely understood, however, several well-known processes that govern electrical breakdown in most solid insulators can be used to provide insight about the results of dielectric tests conducted for this study [67]. In ideal conditions, the electric strength of a pure and homogeneous dielectric material subject to a DC voltage ramp will increase to an upper limit known as its intrinsic electric strength [153, 158]. From an electronic band structure perspective, the intrinsic strength is generally assumed to be reached when electrons in the insulator gain sufficient energy from an applied field to cross the energy gap from the valence band to the conduction band, in which they become increasingly available to carry current and eventually lead to bulk breakdown [158]. The intrinsic model also permits an electron avalanche phenomenon similar to the breakdown mechanism in gases, where injected electrons in the field with sufficient kinetic energy engage in impact ionization followed by exponential growth of mobile, charge carrying electrons. In reality, though these mechanisms utilize the principles of the electronic band structure in solid dielectrics, the intrinsic strength is only reached under experimental conditions and avalanche breakdown is rarely solely responsible for failure of polymers [153, 158, 182]. This is due to many other factors that can also influence charge transport behaviors in solid materials such as the complex hierarchical structure of amorphous polymers, the

existence of electron traps, nanoparticle interfacial morphology, thermal effects, and point defects in the material [67, 89, 153, 155]. For the purposes of this study, several of these factors known to impact dielectric properties in nanocomposites will be used to hypothesize about their influence on the results of the dielectric breakdown testing conducted here.

The dielectric strengths of PA/SiO_2 thin film samples tested in ambient and LN_2-cooled air environments are plotted in Figure 47. Each concentration averages 3-5 measurements from different samples. At room temperature, the average dielectric breakdown strength of the neat polyamide was 135 kV/mm and then reduced to 90 kV/mm as the nanoparticle concentration increased to 6%. Interfacial regions have repeatedly been demonstrated to significantly influence the macroscale dielectric properties of polymer nanocomposites, but a number of simultaneous phenomena occurring in these regions have been attributed to both improving and reducing the bulk dielectric strength of the material [155, 183, 184]. The reduced breakdown strength at higher SiO_2 loadings can be related to nanoparticles acting as nucleating agents that improve the crystallinity of interfacial polymer [99, 100]. Several other studies have reported that at significantly lower loadings of nanoparticles (< 1 wt. %), the nanocomposites can leverage the boundaries of these crystalline regions to improve dielectric breakdown strength [155, 185, 186]. The crystalline boundary regions contain deep traps where higher energy is required to excite electrons into the conduction band around these local regions [155, 185, 186]. Though the increased SiO_2 loadings have resulted in improved thermomechanical stability for the PA/SiO_2 material, the reduction in radius of curvature and surface area of crystalline boundary regions in the material

could have resulted in decrementing its ability to dissipate charge energies through traps [153, 159, 185, 186]. In addition, depending on the filler and polymer materials selected for a given nanocomposite, impurities or structural defects can also be present at interfaces that may introduce local energy levels (trap levels) inside the forbidden gap, lowering the local required excitation energy and allowing electrons to pass through the insulator by jumping from one trap level to another (hopping effect) [158]. Despite the 33% reduction in dielectric strength at the 6 wt. % concentration of SiO_2 particles, the 90 kV/mm recorded value still makes this material an exceptional dielectric. Furthermore, other studies implementing traditional microcomposites have presented greater reductions in dielectric strength at similar volume percent loadings of silica particles, demonstrating the improved multifunctional characteristics of the PA/SiO_2 nanocomposite material [48, 187].

Figure 47

Air Dielectric Failure Analysis of Thin Films

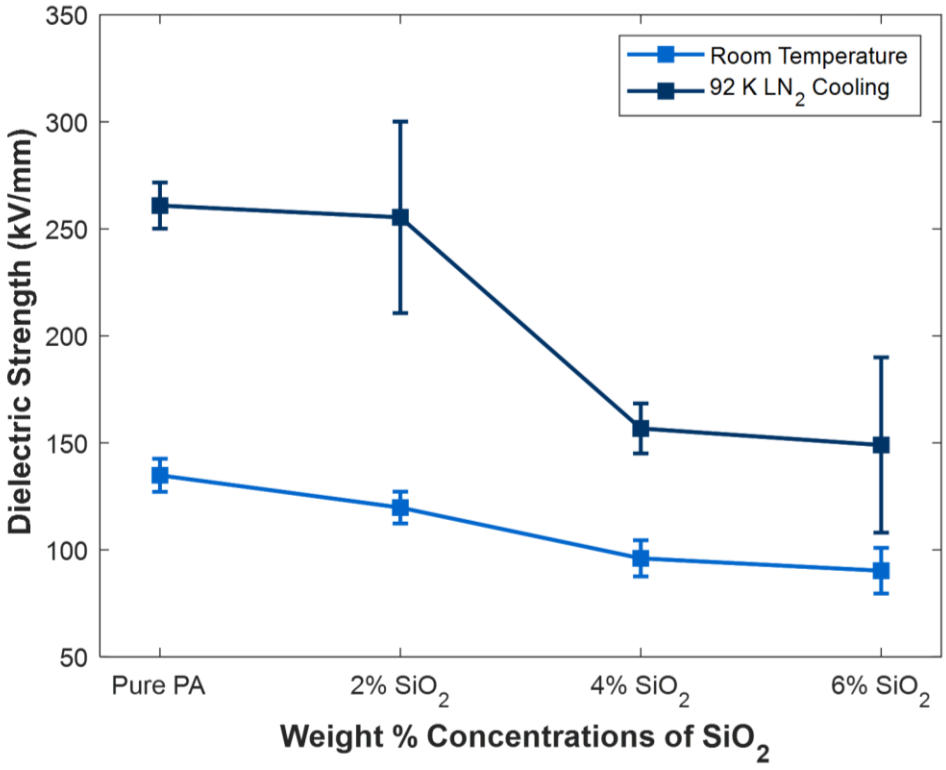

Note. Dielectric breakdown voltage as a function of nanoparticle concentration for PA based thin films at 300 K and 92 K air environments.

The average dielectric strength of neat polyamide in the 92 K LN_2-cooled environment is measured as 261 kV/mm, which is significantly higher than the values from the 300 K testing. The density of free charge carriers in an un-doped material is known to be significantly reduced at low temperatures [188]. This is attributed to the lack of thermal excitation for charge carriers in a cryogenic environment compared to those at room temperature, leading to enhanced dielectric performance [188]. Additionally, the

polymer behaviors at low temperature can contribute to this trend. At room temperature in amorphous polymers, the free volume, defined as inter-molecular distance in the non-crystalline regions of the polymer, can provide a sufficiently large mean free path for charge carriers to maintain the energy required for avalanche breakdown [189]. Temperature dependent increases in the dielectric breakdown strength of polymer-based films at low temperatures can also be attributed to thermal contraction, which not only can densify the material (reducing free volumes), but also can reduce voids and defects that are considered as weak points in the matrix [62, 189]. Therefore, after thermal contraction, carriers may not acquire enough energy to trigger avalanche breakdown at low voltages and low excitation energy traps may be eliminated from the material [182]. The 6 wt. % nanocomposite tested in the 92 K LN_2-cooled environment also showed a reduction in dielectric strength compared to the neat polymer film, but still demonstrates an acceptable 149 kV/mm.

Figure 48 shows the temperature profile measurement taken from the environmental test chamber during a helium cooldown cycle for dielectric testing. During the cryogenic dielectric testing, the environmental chamber reached 50 K in roughly 5 hours and 20 minutes. For comparison, a single vacuum insulated helium transfer hose was connected to both the supply and return connections on the refrigeration box to create the shunted temperature profile shown. In this configuration, the return helium temperature reached 50 K in only 3 hours and 40 minutes. Due to the additional heat loads added when implementing the environmental chamber, the cooling profile for dielectric testing deviates from the shunted configuration, as shown in the figure.

Figure 48

Cryogenic Gas Helium Temperature Profile

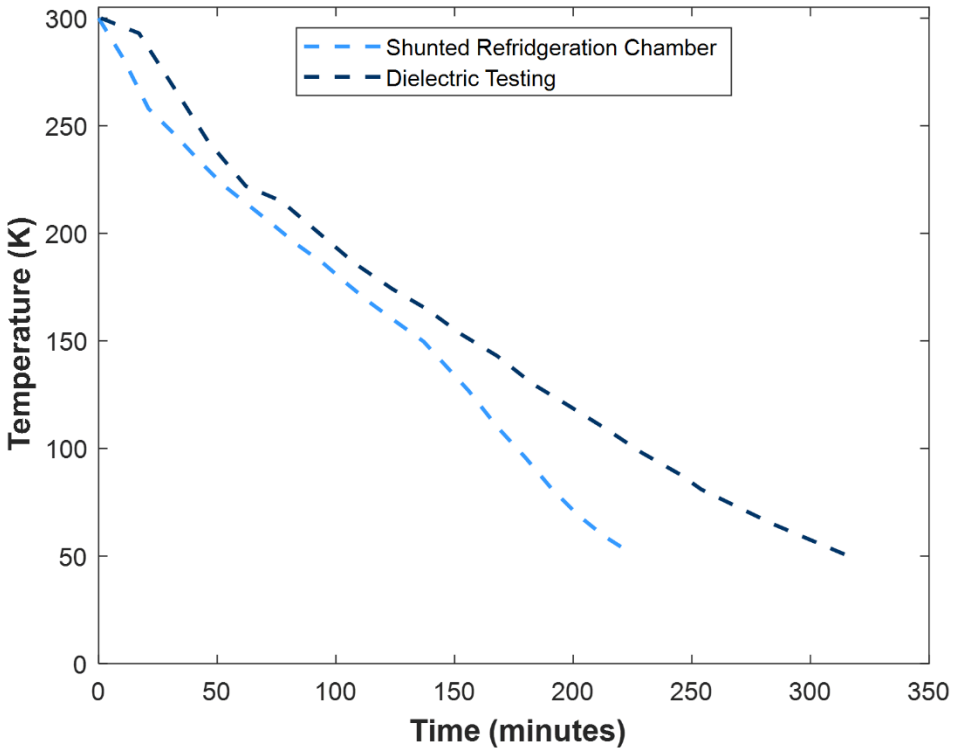

Note. Temperature cooling profile of the cryogenic gas helium dielectric test chamber.

The dielectric strengths of PA/SiO_2 thin film samples tested in the 300 K and 50 K, 100 psi gas helium-cooled environments are plotted in Figure 49. At room temperature, the average dielectric breakdown strength of the neat polyamide was 207 kV/mm and then reduced to 180 kV/mm as the nanoparticle concentration increased to 6 wt. %. The increased dielectric strength in this environment is expected, since the Appendix G calculation demonstrates that the dielectric strength of the 100 psi helium medium is significantly greater than that of the ambient pressure air [164]. The cryogenic temperature results shown here successfully demonstrate that the PA/SiO_2 nanocomposite

material indeed operates as an effective dielectric in the operating environment of HTS power transmission cables. The 285 kV/mm dielectric strength of the 6 wt. % concentration at the cryogenic temperature allows thin nanocomposite coatings to be implemented on superconductors, reducing the likelihood of dielectric failure due to internal point imperfections [67, 153]. When combined with its thermal stability characteristics that significantly reduce the likelihood of mechanical failures, the multifunctional characteristics of the proposed nanocomposite dielectric make it an exceptional candidate for use in HTS systems.

Figure 49

Helium Dielectric Failure Analysis of Thin Films

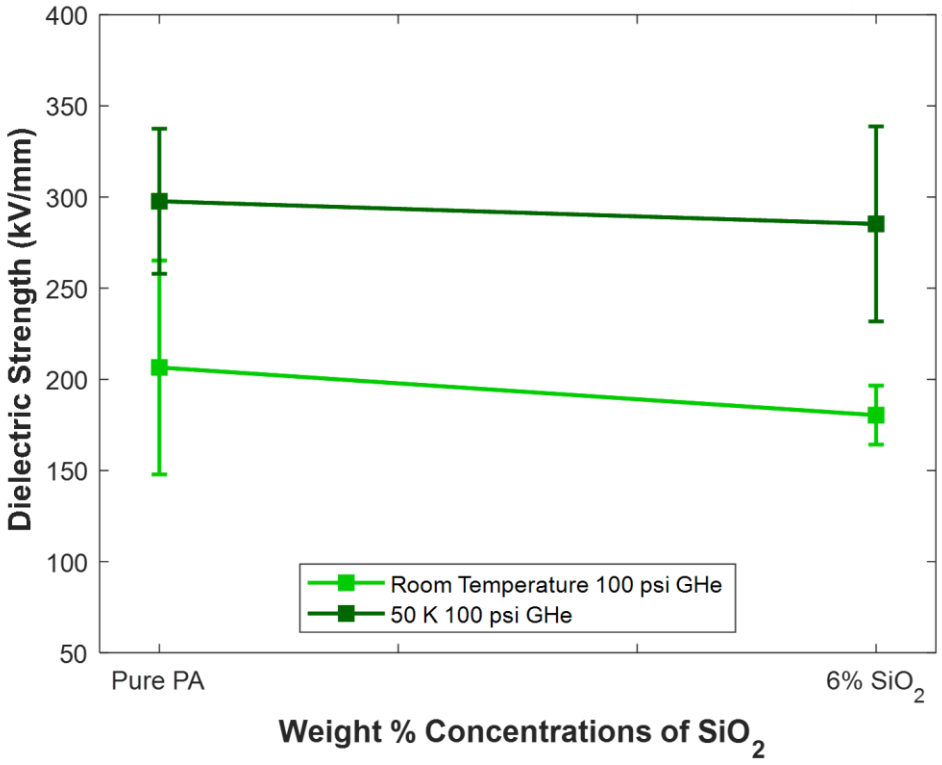

Note. Dielectric breakdown voltage as a function of nanoparticle concentration for PA based thin films at 300 K and 50 K pressurized gas helium environments.

Shown in Figure 50, failed samples from dielectric testing were also inspected with SEM imaging to ensure that the recorded failures were caused by high-voltage dielectric breakdown internally, rather than by arcing through the surrounding medium. Both samples show a circular structure with smaller through holes in their centers. During breakdown, the weak points in the sample experience partial breakdown as well as localized heating in their surrounding areas, likely resulting in the melting, merging, and

formation of larger channels inside the breakdown point [153]. Evidence of the thermal effects of electrical breakdown through the matrix is demonstrated by plastically deformed polymer around the failure holes. In addition, closer inspection of the hole interiors in Figure 50 shows radial striations of plastic deformation where it is suspected that the melting of viscous polymer occurred. Finally, the greater plastic deformation that is visible around dielectric failures from the 100 psi helium environment could have resulted from larger thermal effects due to the higher breakdown voltages of the material.

Figure 50

SEM Imaging of PA/SiO_2 Dielectric Failures

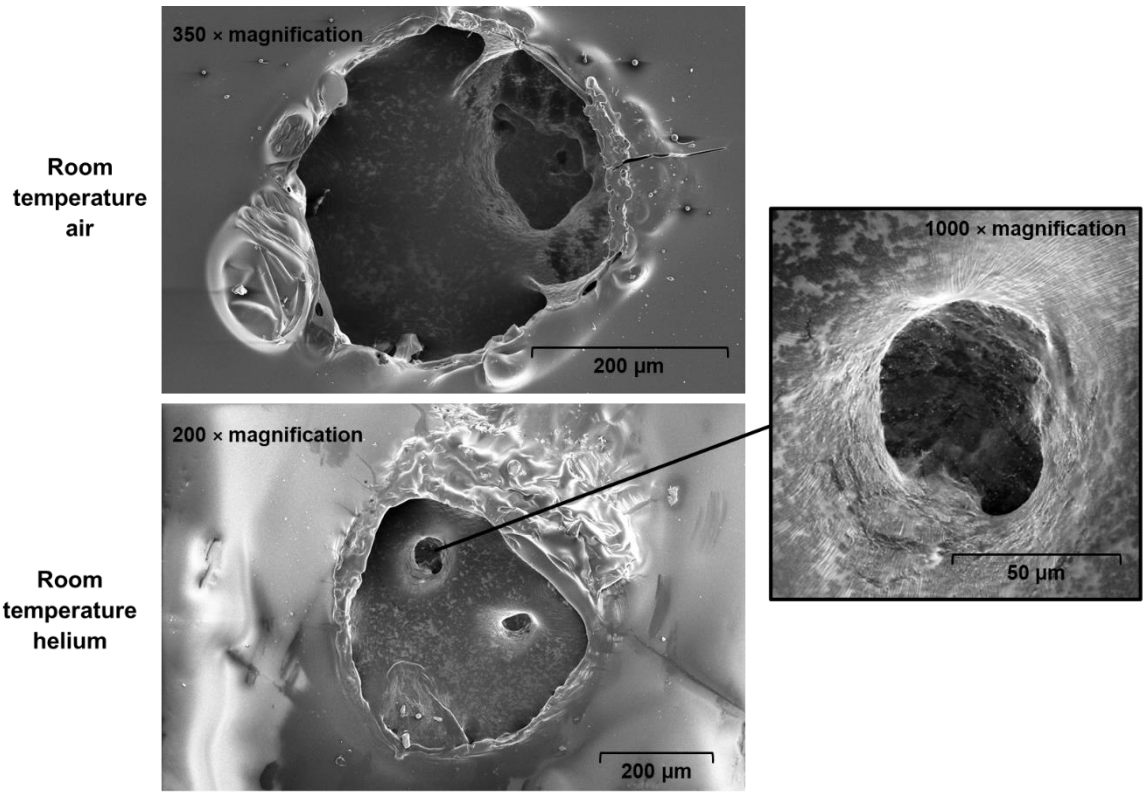

Note. SEM images of 6 wt. % PA/SiO_2 nanocomposite thin film dielectric breakdown in room temperature air (top) and 100 psi helium (bottom) environments.

4.2.2 Evaluating On-Cable Dielectric Performance with Coated Electrodes

Mechanical stress is also known to affect electrical breakdown behavior, since stress can influence molecular chain movement, crystallinity, and free volume, leading to changes in breakdown strength. As nanocomposite coating on a cable may have more internal stresses than its free-standing thin film form, it becomes necessary to conduct breakdown testing on coated samples [153, 159, 190, 191]. The dielectric strengths of

PA/SiO_2 coated electrode samples tested in ambient and LN_2-cooled air environments are plotted in Figure 51. Each concentration averages 5 measurements from different samples. At room temperature, the average dielectric breakdown strength of the neat polyamide coating was 217 kV/mm and slightly increased to 246 kV/mm as the nanoparticle concentration increased to 6%. The trends depicted here are unexpected compared to the thin film samples tested in the previous section. The lack of decremented dielectric strength at the 6 wt. % concentration could be attributed the dip-coating preparation method used for the samples. In general, sol-gel dip-coating processes can greatly alter the structure and properties from the liquid precursor to the microstructure of the corresponding deposited film [84]. After vertically immersing dowels in the polymer nanocomposite precursor suspension during preparation, gravity pulls down on the fluid contained in a viscous boundary layer with the substrate, eventually resulting in a thin, uniform, and repeatable surface coating [84]. The continuous gravity drip process that reduces the thickness of the entrained coating may also assist in reducing voids that act as point imperfections in these coatings. Therefore, removing these structural defects at interfacial regions could reduce the trap levels within the energy gap and result in comparative dielectric strengths between pure and loaded SiO_2 nanocomposite samples [158].

Figure 51

Air Dielectric Failure Analysis of Coated Electrodes

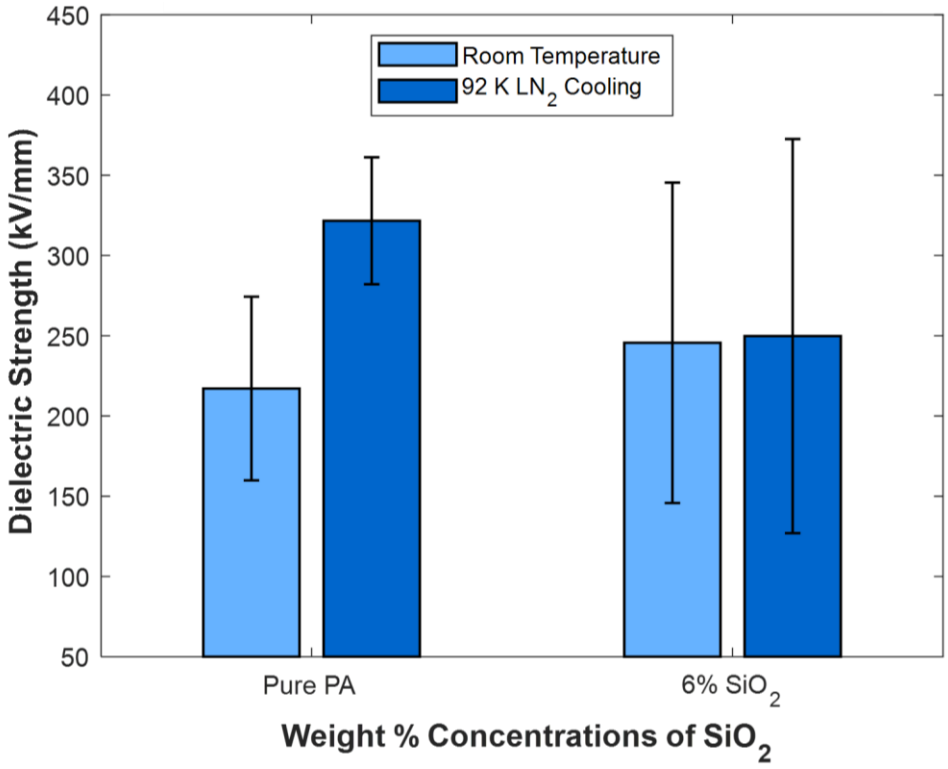

Note. Dielectric breakdown voltage as a function of nanoparticle concentration for PA based coated electrodes at 300 K and 92 K air environments.

The pure polyamide coated samples demonstrate similar temperature dependent behaviors to the films tested in the previous section. However, at the 6 wt. % concentration of SiO_2 particles, the influence of temperature appears to be significantly reduced. As thin film samples with 6 wt. % SiO_2 loadings show a 50% increase in dielectric strength at the two temperatures (90 kV/mm for 300 K and 149 kV/mm for 92 K, shown in Figure 51), the breakdown strength for these dowel-coated 6 wt. %

composite samples is relatively uniform (246 kV/mm for 300 K and 250 kV/mm 92 K). It can be hypothesized that the consistent performance of the dowel-coated composite samples is a result of multiple, and sometimes counteracting factors that can simultaneously contribute improving or reducing to the dielectric strength. The factors that can increase the dielectric strength at a lower temperature include the reduced number of free charge carriers, denser materials, and less voids due to thermal contraction, as discussed earlier. However, thermal contraction introduces additional defects into the dowel-coated composite samples. Once cured films are fixed to the substrate and significantly limited from internal contraction (the contraction of the dowel is minimal compared to that of the polymer), tensile stresses are known to develop in the plane of the substrate [84]. In addition, thermal contraction with respect to individual silica nanoparticles results in compressive stress from the polymer and causes significant additional loading at individual particle interfaces [130]. The heightened pre-stressed condition of low temperature nanoparticle interfacial regions proposed in Chapter 3, when combined with tensile stresses in the coating, could initiate interfacial void growth. These induced defects would significantly diminish the bulk dielectric strength of dowel-coated samples in the low temperature tests.

Potentially, the limited internal contraction of the dowel coatings at low temperature also prevents known stress relaxation via allowed plastic deformation from occurring, resulting in increased defect formation in the matrix. By comparison, thin film samples are detached from the substrate and can contract freely during low temperature testing. The free contraction can reduce the number of stress-induced defects and voids inside the material. Considering all these factors, the thin film composite samples show a

significant temperature dependence while the dowel-coated composite samples show fairly consistent readings at both 300 K and 92 K. With these hypotheses, the larger standard deviations of the 6 wt. % nanocomposite samples are also acknowledged here. The deviations demonstrate that additional studies are required to locate dip-coating methods and parameters for larger scale, higher quality manufacturing of the nanocomposite coatings. These specific challenges will be discussed in the following chapter of this study. However, the ~250 kV/mm strength of the 6 wt. % concentration nanocomposite presented here still lies well within acceptable values as a dielectric and most critically, a significant degradation in average dielectric strength does not occur due to the additional mechanical stresses induced in these thin coatings.

Chapter 5

Experimental Manufacturing of Nanocomposite Dielectric Coatings

5.1 Exploring the Challenges of Nanocomposite Dip-Coating Processes for HTS Systems

Accomplishing liquid deposition through dip-coating is a versatile method for producing homogeneous, repeatable coatings by entraining a solution on a substrate and evaporating volatile compounds [192]. However, time-dependent evaporation-induced concentration and viscosity gradients in coating materials make for a dynamic, complex system that often requires detailed experimental characterization to achieve desired results [192]. In addition, though the nanocomposite dielectric developed here exhibits material processing characteristics that are consistent with those of HTS tapes, the manufacturing process itself must also be compatible with the design parameters of HTS transmission cable systems. This chapter will investigate design considerations for manufacturing PA/SiO_2 nanocomposite coatings and conduct experimental manufacturing efforts towards a transition to large scale processing of this material. Figure 52 shows an overview of the proposed dip-coating process for deposition and curing of the nanocomposite suspension on coaxial HTS transmission cables or individual HTS tapes. In this spool-to-spool format, a system of rollers feeds the substrate through a bath where a thin layer of the suspension is entrained on its surface and then thermally cured into solid enamel through a tunnel furnace. This method has repeatedly been implemented to deposit and cure polyimide precursor solutions into solid dielectric layers for a variety of electronics applications [74, 193-195]. Additionally, efforts in sol-

gel dip coating have successfully realized the formation of functionalized nanocomposite layers for both dielectric and chemical barrier purposes [196, 197].

Figure 52

Overview of Dip Coating Process

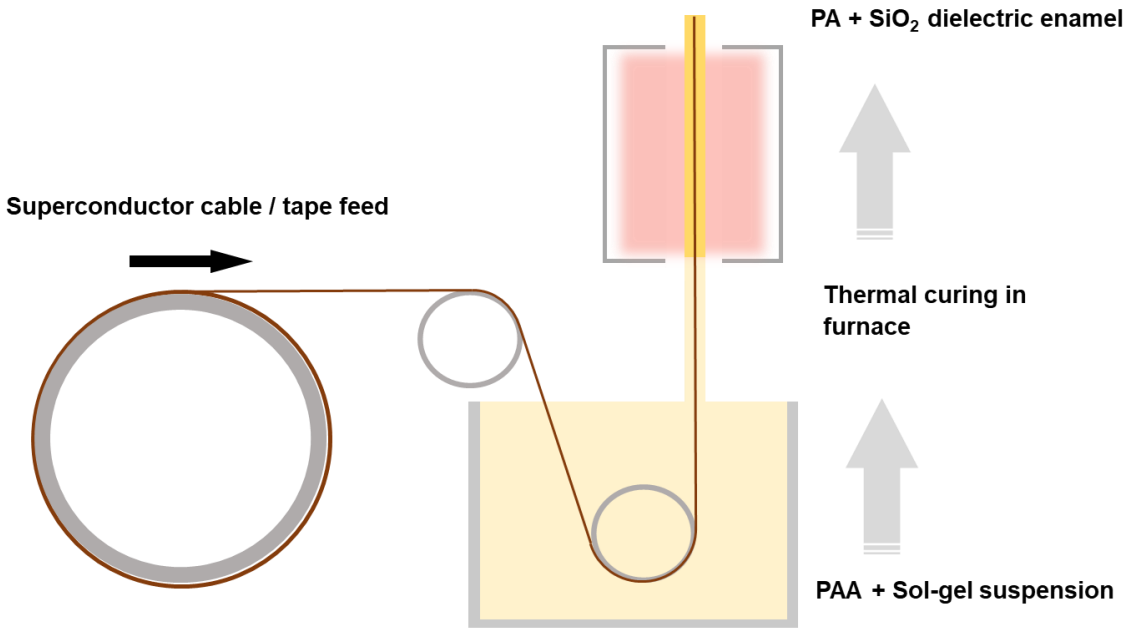

Note. The dip coating process of immersion, beginning, deposition, draining, and evaporation.

The basic model for fluid entrainment on the surface of the HTS substrate is described by an equilibrium state between adhesion of the fluid on the substrate and gravity-induced viscous drag [192, 198]. As shown in Figure 53, the properties of streamline flow patterns during deposition of the nanocomposite coating are primarily

defined by the relationship between withdrawal speed, U_o, of the substrate and the resulting entrained coating thickness, h_o [84]. Fluid above the stagnation point, S, flows toward the direction of withdrawal through capillary action and fluid below the point flows toward the reservoir surface by viscous drag [84]. The coating thickness exists at an equilibrium between density, surface tension, and viscosity of the PAA/sol-gel suspension in a proportional relationship with the substrate withdrawal speed [192, 198]. Additional considerations have been made for non-Newtonian sol-gel precursors like the suspension used here, which account for the concentration of the solution, as well as dynamic viscosity due to changes in density, changes in surface tension and constant solvent evaporation during substrate withdrawal [84, 192]. In order to implement a scalable dip-coating process for the manufacturing of a PA/SiO_2 coating, the influences of each of these factors on nanocomposite deposition should be experimentally determined.

Figure 53

Fluid Element Trajectories During Coating Entrainment

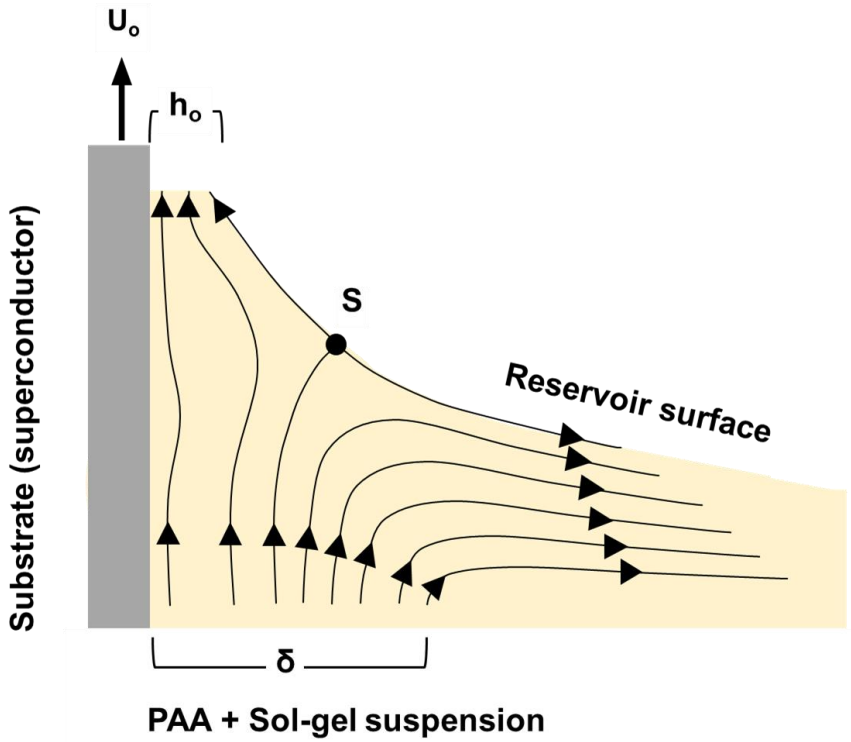

Note. Streamline flow patterns during substrate withdrawal in the dip-coating process. U_o is the withdrawal speed, S is the stagnation point, δ is the boundary layer and h_o is the thickness of the coated fluid on the substrate [84].

The physical design and construction of HTS transmission cables are other factors that will significantly influence development of the nanocomposite dielectric manufacturing process. Shown in Figure 54 A, HTS transmission cables have traditionally been manufactured in a coaxial configuration, where layers of HTS tapes are wound around a central former and fully enveloped by the dielectric layer. A point of

concern in manufacturing dip-coated dielectric layers for this cable configuration is the permanent deformation of thin-walled stainless steel cable formers over rollers. In order to prevent this from occurring, the process must ensure not to exceed minimum former bend radii or cause significant axial stresses along the cable length during withdrawal from the suspension bath. This translates to the requirement of a highly customized manufacturing system for deposition on coaxial HTS cables, which would likely only be capable of coating shorter sections of cable at a time.

Alternative approaches to cable construction have been suggested to reduce the risk and complexity of HTS cable manufacturing, as well as allowing for continuous processes [33]. The individually insulated conductor approach shown in Figure 54 B suggests winding already insulated HTS tapes around the central former, eliminating the coaxial configuration and allowing for simplified spool-to-spool coating operations [33]. However, this method also has drawbacks due to the present-day manufacturing quality of 2G HTS tapes themselves. Existing HTS power transmission systems operate far from their full capability near critical current due to the potential for manufacturing imperfections to create areas of electrical resistance [199]. The systems avoid potentially decremented power transfer in manufactured defects by sharing and redistributing current between many HTS tapes wound in a single coaxial layer [199]. Therefore, the existing state of manufactured quality in HTS power transmission systems may also be a limiting factor in implementing large scale processes for PA/SiO_2 dielectric coatings. The development of this dip-coated manufacturing process must feature a systems-level integration approach that accommodates all of the chemical and mechanical material

properties discussed here, along with the resulting performance of superconducting power transmission in the cable format.

Figure 54

Manufacturing PA/SiO_2 Nanocomposite Coatings

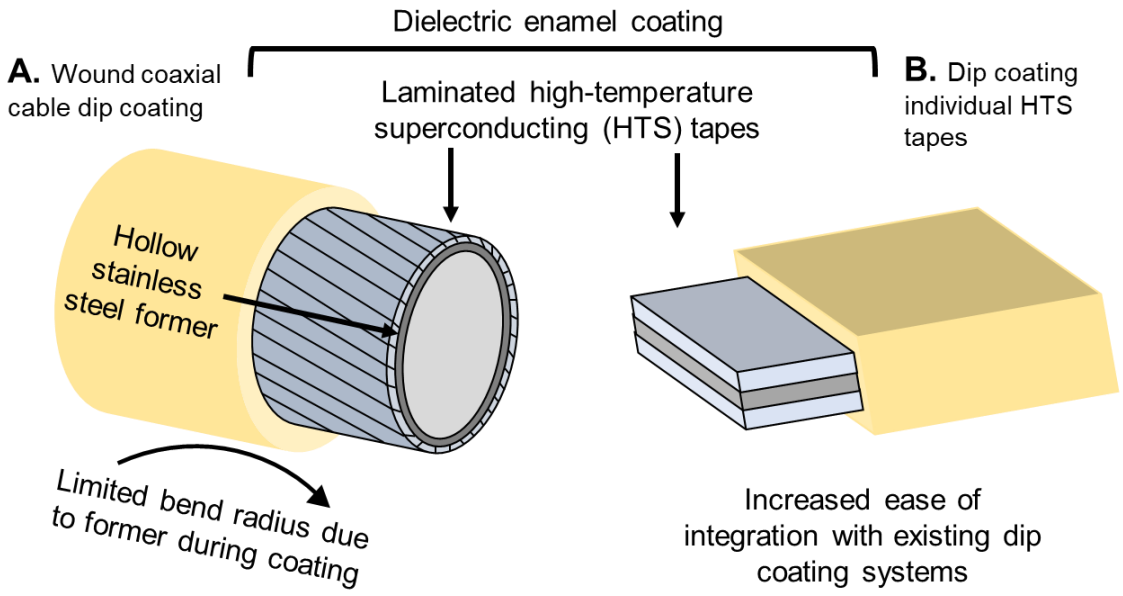

Note. Comparison of dip coated layers in coaxial HTS cables with coating individual HTS tapes.

5.2 Development of a Manufacturing Process for PA/SiO_2 Nanocomposite Coatings

In this study, an experimental system was designed and constructed for dip-coating the PA/SiO_2 nanocomposite on conductive tapes and performing an initial investigation of the parameters influencing the properties of dielectric coatings. Studying the changes in viscosity of the PA/SiO_2 suspension over time was a critical initial step to

verifying that the nanocomposite bath could be exposed to ambient air conditions and maintain its properties for continuous manufacturing processes. Considerable research efforts are devoted to the study of conformal coatings for various electronics applications and the pot-life, or usable working time of the material, is an influential parameter for implementing these viscous solutions [200]. Using Equation 5 and a simple, miniature ball-drop device, the six fluid viscosity measurements of a PA/SiO_2 nanocomposite suspension shown in Figure 55 were taken over a period of 70 minutes [201]. The analysis conducted here demonstrated that the general stability of the nanocomposite's viscosity over this period made it suitable for implementation in a small-scale experimental dip-coat manufacturing system. As the data from this brief experiment was only intended for comparative use within this study, wider analysis of the suspension's rheology should be conducted for an effective characterization.

$$\eta = \frac{d^2\,(\rho_s - \rho_l)gT}{18L} \tag{5}$$

Where:

η = fluid viscosity, Pa·s

d = diameter of sphere, mm

ρ_s = density of sphere, g/mL

ρ_l = density of fluid, g/mL

g = gravitational acceleration, m/s^2

T = time of sphere travel, s

L = distance of sphere travel, mm

Figure 55

Viscosity of PA/SiO_2 Suspension vs. Time

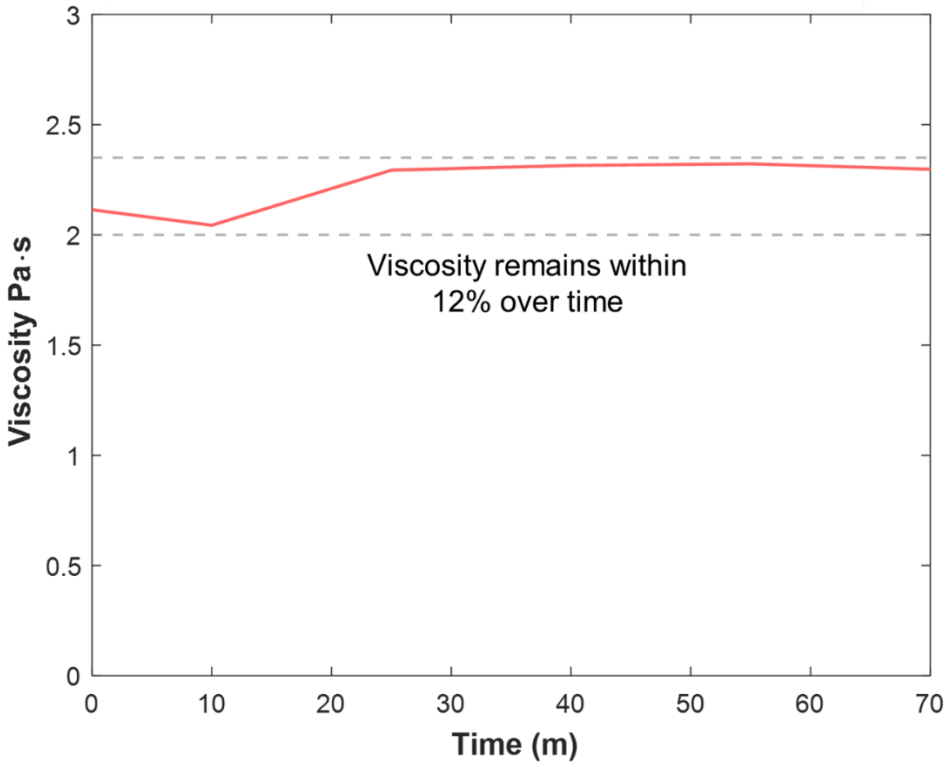

Note. Study of PA/SiO_2 suspension viscosity over time for experimental scale coating processes.

Figure 56 shows the design and assembly of the experimental spool-to-spool manufacturing system for dip-coating the nanocomposite on HTS tapes. The tape substrate is drawn from the uncoated spool, where the first roller immerses it in the nanocomposite solution. Following this, the tape is prebaked for solidification in a 0.3 meter tube furnace, where it is heated at roughly 90 °C for 5 minutes. Full solvent evaporation and curing then occurs in a 1.0 meter tube furnace for 15 minutes at 115 °C. The purpose of the initial prebaking step was to prevent any unwanted dripping of the coatings within the larger horizontal furnace. 8 mm wide × 0.125 mm thick nickel tapes

were utilized as a conductive analog for HTS tapes in evaluating the films deposited in this process. Figure 57 shows pure polyamide that was successfully coated and cured on a section of the nickel tape. The manufacturing system developed here presents a path forward for conducting experiments that study the dynamic factors impacting nanocomposite dielectric film deposition in spool-to-spool dip-coating processes.

Figure 56

Spool-to-Spool System for Coating HTS Tapes

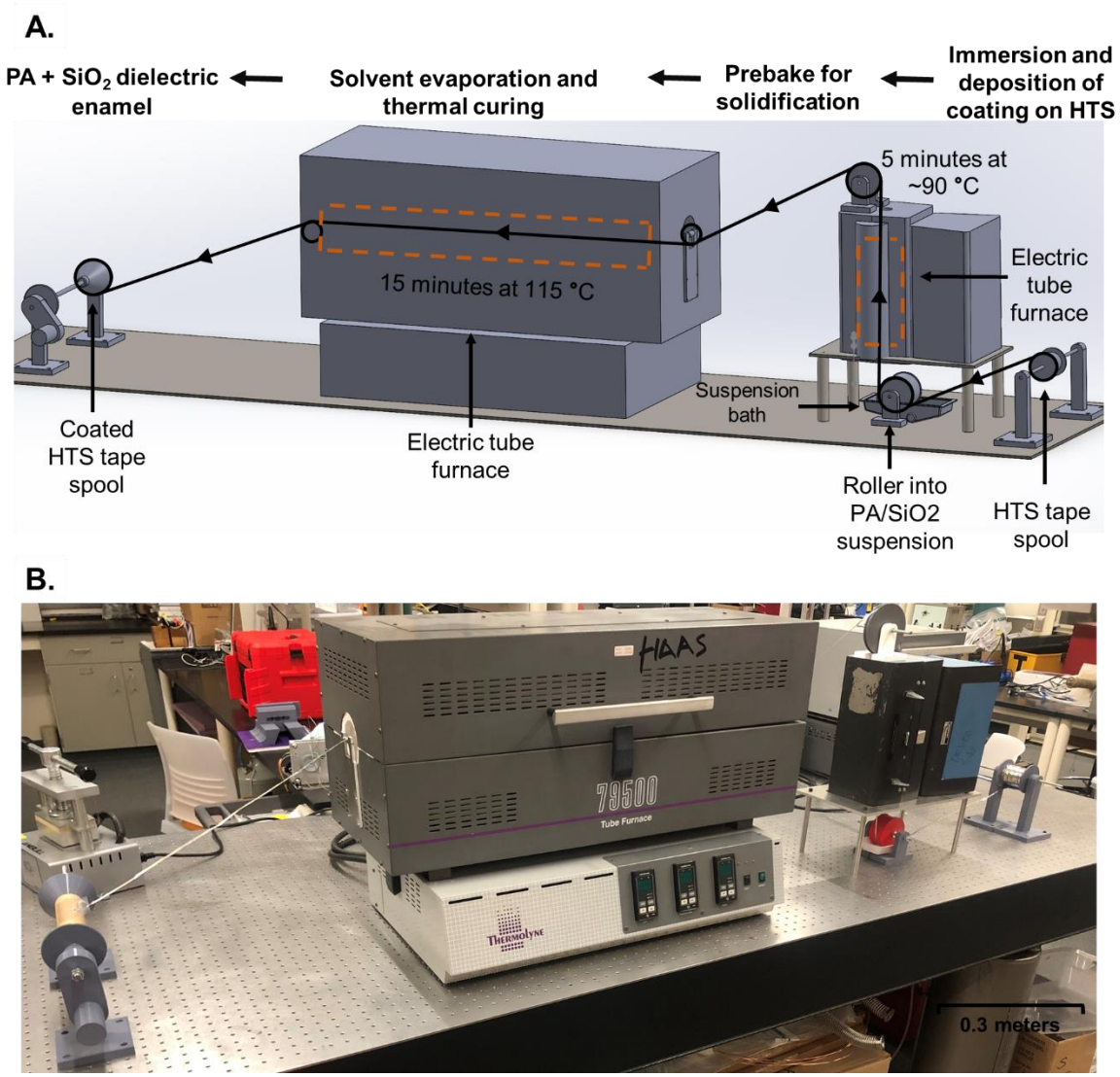

Figure 57

Polyamide Coated HTS Nickel Tape Samples

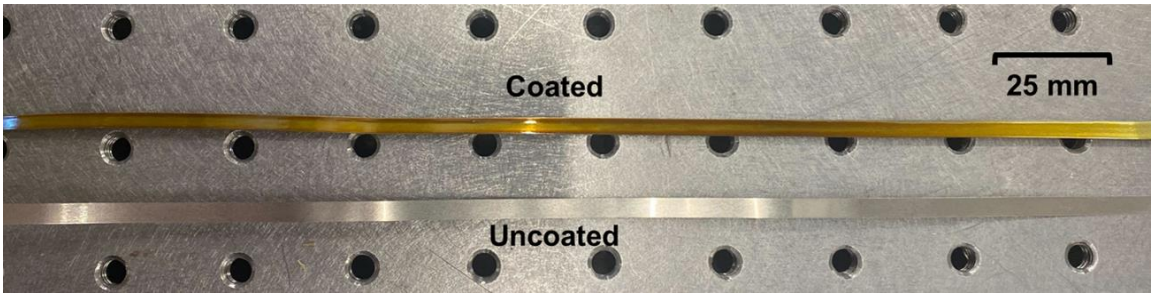

Chapter 6

Conclusion

6.1 Summarizing Experimental Results and Their Significance for HTS Power Transmission

HTS cable systems have demonstrated the potential to revolutionize energy grid power transmission and help unlock a fully electric transportation infrastructure of the future [1, 3, 4]. The development of a rugged dielectric coating material suited to the extreme superconductor operating environment contributes to solving the material challenges associated with increased integration of HTS systems. A PA/SiO_2 nanocomposite was proposed as a dielectric with improved thermal stability for the cryogenic environment, low temperature processing characteristics, and exceptional multifunctionality that reduces material property trade-offs. Extensive mechanical, thermomechanical, and dielectric characterization efforts were completed to establish property relationships between the structure, processing, and performance of the nanocomposite material. Following this, an experimental coating system was developed for future experiments that will enable full scale manufacturing of the nanocomposite dielectric with HTS transmission cables.

During material development, Dupont Pyre-M.L.® thermoset varnish was selected as a commercial polyamic acid precursor for its thermomechanical stability, dielectric strength, solvent resistance, and high mechanical strength [40, 72, 74]. An in-situ sol-gel processing method was used to produce matrices of SiO_2 nanoparticles ranging from 50 nm to 200 nm in diameter that would further reduce the CTE of the bulk nanocomposite material [106]. Additional SEM characterization efforts used high-

resolution imaging and EDS to verify the formation of silica nanoparticle structures within the material. Following this, thermogravimetric analysis was used to develop a low temperature thermal curing process for the PA/SiO_2 coating material that was compatible with HTS tape manufacturing. Finally, SEM imaging was used to explore the sensitivity of several parameters in the sol-gel process that resulted in different nanoparticle structures.

The following section of this study investigated the mechanical properties of the nanocomposite to verify that SiO_2 particle addition effectively reduced the CTE of the bulk material without excessively decrementing the other material properties such that it could not be implemented as a manufactured dielectric coating. Thin film samples of the nanocomposite were utilized for thermomechanical analysis, which demonstrated that increasing SiO_2 nanoparticle loadings to the 6 wt. % concentration resulted in a 30% thermal stability improvement and significantly reduced the CTE of the bulk material. In order to verify that these nanoparticle loadings did not decrement other mechanical properties and to characterize the behaviors of PA/SiO_2 nanocomposite thin films in the cryogenic environment, a novel tensile testing system was developed for this study. This testing found that the PA/SiO_2 nanocomposite's thermomechanical stability exceeded other industry dielectric coating options, while maintaining its mechanical properties in the cryogenic operating conditions of superconductors. Additionally, SEM characterization of plasma etched thin film samples was used to explore the interfacial mechanics and failure mechanisms of the material that granted its exceptional thermomechanical performance. Therefore, these conclusions were used to verify that the

mechanical properties of the proposed nanocomposite dielectric made it well suited for operating in extreme cryogenic temperature conditions.

Despite evidence that the proposed PA/SiO_2 nanocomposite demonstrated exceptional thermomechanical properties, its bulk electrical breakdown characteristics were most critical for implementing the material as an insulator. The objective was to leverage the dominant particle-polymer interfacial properties of the material to enable exceptional multifunctionality and maintain adequate dielectric breakdown performance. Due to the fact that electrical breakdown performance is heavily influenced by factors such as sample dimensions, temperature, pressure, humidity, and mechanical stress, multiple dielectric test systems were implemented to characterize the impacts of these parameters [153, 156]. The most significant of these experiments was the development and implementation of a cryogenic environmental test chamber for conducting dielectric failure analyses of the material in the same 50 K, pressurized gas helium environment in which the HTS transmission cables operate. Thin film samples subject to dielectric failure in room temperature air conditions saw a 33% reduction in their dielectric strength as the 6 wt. % concentration of SiO_2 particles was approached, but the 90 kV/mm dielectric strength of these films was still an exceptional value for implementation as a dielectric coating material. A similar concentration dependent trend was observed in the LN_2-cooled air environment (261 kV/mm at 0% to 150 kV/mm at 6 wt. %), but this testing environment resulted in dielectric strength improvements as high as 93% due to the well reported temperature dependency of electrical breakdown.

In the pressurized gas helium environment, similar concentration dependent reductions in dielectric strength (207 kV/mm at 0% to 180 kV/mm at 6 wt. %) were also

observed, but this environment also resulted in significant increases in dielectric strength due to the improved breakdown characteristics of the room temperature 100 psi helium test medium. Most critical to these results, however, was the ~300 kV/mm dielectric strength of the 6 wt. % concentration in the 50 K cryogenic environment. These results successfully demonstrated that the PA/SiO_2 nanocomposite material could indeed operate as an effective dielectric in the cryogenic GHe-cooled operating environment of HTS power transmission cables. Conductive electrodes coated with the PA/SiO_2 dielectric were also tested to characterize the impact of mechanical stresses induced in coatings on the electrical breakdown behavior. For the neat polyamide film the average dielectric breakdown strength at room temperature was 217 kV/mm and as expected, this increased to 321 kV/mm in the LN_2-cooled air environment. The other trends of dielectric breakdown strength depicted here were unexpected compared to the thin film sample tests. As the nanoparticle concentration increased to 6%, the expected reduction in dielectric strength was not present (246 kV/mm at 6 wt. %). It was hypothesized that this was attributed to a reduction in structural defects due to the preparation of nanocomposite samples that resulted in comparative dielectric strengths. When the 6 wt. % sample was cooled to 92 K in the LN_2 testing environment, its dielectric strength also still remained comparable to this value. The consistent performance of the dowel-coated composite samples was attributed to a complex result of multiple, and sometimes counteracting, factors that influenced the dielectric strength of these samples. In general, the results of this characterization demonstrated that when these dielectric characteristics are combined with a thermal stability that significantly reduces the likelihood of mechanical failure due to cryogenic operation, the multifunctional properties of this PA/SiO_2 nanocomposite

make it an exceptional candidate for dielectric use in HTS systems. Table 3 summarizes all mechanical and dielectric property measurements taken from various nanocomposite concentrations in this study.

Table 3

Summary of Mechanical and Dielectric Properties from Various Concentrations of PA/SiO_2 Nanocomposites

	Weight % SiO_2	Pure PA	2%	4%	6%
Thermomechanical Properties	Linear Thermal Expansion (%), 25 → 125 °C	0.6	0.51	0.39	0.39
Mechanical Properties	Elastic Modulus (MPa), 20 °C	1,839	1,810	2,109	2,141
	Elastic Modulus (MPa), -90 °C	2,707	840	1,021	2,395
	Ultimate Tensile Strength (MPa), 20 °C	58	57	74	78
	Ultimate Tensile Strength (MPa), -90 °C	38	7.7	9.2	37
Dielectric Properties	DC Dielectric Breakdown Strength (kV/mm), 20 °C Air	135	120	96	90
	DC Dielectric Breakdown Strength (kV/mm), -181 °C Air	261	255	157	149
	DC Dielectric Breakdown Strength (kV/mm), 20 °C 100 psi Ghe	207	-	-	180
	DC Dielectric Breakdown Strength (kV/mm), -223 °C 100 psi Ghe	298	-	-	285

The experimental dip-coating system detailed in the following section of the study was developed as a platform for transforming the PA/SiO_2 nanocomposite material into a manufactured coating. This system can be implemented to help understand the time-dependent evaporation-induced concentration and viscosity gradients in coating materials that require detailed experimental characterization to achieve desired results [192]. In order to eliminate cryogenic dielectric material failures in existing HTS power systems and dramatically improve their transmission efficiencies through gas helium cooling techniques, the opportunity existed for this study to development a multifunctional nanocomposite material suited to this unique application. In summary, the characterization studies conducted here have presented a viable option to solve the challenges impeding wider implementation of HTS power transmission and have charted a path forward for its transformation into a manufactured engineering material.

6.2 Addressing Future Works

A number of future research efforts are likely still required to fully realize the PA/SiO_2 nanocomposite developed here as a dielectric coating solution for HTS power transmission systems. An important short-term step to achieving this is the continuation of experimental manufacturing efforts that utilize the system developed in Chapter 5 of this study to fully investigate parameters for large scale processing of the coating. This includes studying the parameters that influence the nanocomposite dip coating quality on individual HTS tapes and establishing additional manufacturing system design requirements for handling coaxially oriented cable sections. A TA Instruments Discovery Series Hybrid Rheometer (DHR) is now available to this study for additional material characterization experiments. A detailed study of the rheological properties of the

nanocomposite suspension would provide valuable insight for using the material in large scale processes. Additionally, a dielectric testing accessory has been installed with the system that enables a study of AC dielectric properties of the material in response to thermal and mechanical loadings. Though the DC testing completed here was valuable for establishing various property relationships for the material, characterizing the material under AC electrical stress will verify its fitness for use in multi-phase power transmission systems and provide greater insight about its intrinsic charge transport mechanisms. A final step in short term experimental efforts would be utilizing the cryogenic gas helium environmental chamber to operate a coated superconducting tape section, studying the longer cycles of HTS operation in this configuration and the potential effects of partial breakdown mechanisms over time.

Successfully implementing a manufactured nanocomposite dielectric is critical to the completion of this study, but additional experimentation will also expand the fundamental understanding of polymer nanocomposite materials. The results of the dielectric and mechanical studies completed here were separately connected to known theoretical properties of nanoparticles. However, deepening the underlying knowledge of nanoparticle interfacial mechanics would allow this study to develop metrics that bridge the gap between electrical and mechanical properties. This could provide a universal understanding of the material which relates its nanoscale structure directly to the performance of various properties. Potentially, this information could then be used to better predict the performance of new multifunctional nanocomposite materials before experimental characterization takes place. In the near future, this study will gain access to an atomic force microscope (AFM), which can closely examine the interactions between

the polymer and nanoparticles at the molecular level. In addition to topographic imaging, the system can use nanoindentation measurements to characterize colloidal interactions, stiffness, and viscoelastic properties of nanoscale structures [202]. Additionally, other studies have implemented AFM techniques to better characterize the electronic band structure of nanomaterials and gain a deep understanding of their intrinsic charge transport mechanisms [203]. To supplement the AFM system, various other methods such as X-ray diffraction (XRD) and Fourier Transform Infrared (FTIR), have also been used to show chemical bonding in semi-crystalline interfacial regions of nanoparticle matrices [67, 204, 205]. These analyses will be significant in understanding the role of nano-mechanical properties in a multifunctional material on the macro scale.

References

[1] R. A. Hawsey and S. Morozumi, "The Energy and Environmental Benefits of Superconducting Power Products," *Mitigation and adaptation strategies for global change,* vol. 10, no. 2, pp. 279-306, 2005, doi: 10.1007/s11027-005-9031-4.

[2] R. Schiferl, A. Flory, W. C. Livoti, and S. D. Umans, "High-Temperature Superconducting Synchronous Motors: Economic Issues for Industrial Applications," *IEEE transactions on industry applications,* vol. 44, no. 5, pp. 1376-1384, 2008, doi: 10.1109/TIA.2008.2002219.

[3] C. Rey, *Superconductors in the Power Grid : Materials and Applications*. Cambridge, United Kingdom: Elsevier Science & Technology, 2015.

[4] T. J. Haugan, J. D. Long, L. A. Hampton, and P. N. Barnes, "Design of Compact, Lightweight Power Transmission Devices for Specialized High Power Applications," *SAE International journal of aerospace,* vol. 1, no. 1, pp. 1088-1094, 2009, doi: 10.4271/2008-01-2930.

[5] M. Tomita *et al.*, "Design and Development of Superconducting Dc Cable for Railway Applications," *IEEE transactions on applied superconductivity,* vol. 23, no. 3, pp. 3601504-3601504, 2013, doi: 10.1109/TASC.2013.2251742.

[6] J. A. Demko *et al.*, "Triaxial Hts Cable for the Aep Bixby Project," *IEEE transactions on applied superconductivity,* vol. 17, no. 2, pp. 2047-2050, 2007, doi: 10.1109/TASC.2007.897842.

[7] J. H. Lim *et al.*, "Performance Test of 100 M Hts Power Cable System," *IEEE transactions on applied superconductivity,* vol. 19, no. 3, pp. 1710-1713, 2009, doi: 10.1109/TASC.2009.2018053.

[8] J. P. Stovall *et al.*, "Installation and Operation of the Southwire 30-Meter High-Temperature Superconducting Power Cable," *IEEE transactions on applied superconductivity,* vol. 11, no. 1, pp. 2467-2472, 2001, doi: 10.1109/77.920363.

[9] M. Robinson, "Advanced Energy Technology of the Week: High Temperature Superconducting (Hts) Transmission."

[10] M. Tomita, Y. Fukumoto, K. Suzuki, and M. Miryala, "Development of Prototype Dc Superconducting Cable for Railway System," *Physica. C, Superconductivity,* vol. 470, no. 1, pp. S1007-S1008, 2010, doi: 10.1016/j.physc.2010.03.014.

[11] F. F. da Silva, J. F. P. Fernandes, and P. J. da Costa Branco, "Barriers and Challenges Going from Conventional to Cryogenic Superconducting Propulsion for Hybrid and All-Electric Aircrafts," *Energies (Basel),* vol. 14, no. 21, p. 6861, 2021, doi: 10.3390/en14216861.

[12] P. J. Masson, G. V. Brown, D. S. Soban, and C. A. Luongo, "Hts Machines as Enabling Technology for All-Electric Airborne Vehicles," *Superconductor science & technology,* vol. 20, no. 8, pp. 748-756, 2007, doi: 10.1088/0953-2048/20/8/005.

[13] J. L. Felder, G. V. Brown, H. DaeKim, and J. Chu, "Turboelectric Distributed Propulsion in a Hybrid Wing Body Aircraft," Hampton, 2011: NASA/Langley Research Center.

[14] K. Nordal, "Yara to Start Operating the World's First Fully Emission-Free Container Ship," ed: Yara International ASA, 2021.

[15] B. K. Fitzpatrick, J. T. Kephartl, and E. M. Golda, "Characterization of Gaseous Helium Flow Cryogen in a Flexible Cryostat for Naval Applications of High Temperature Superconductors," *IEEE transactions on applied superconductivity,* vol. 17, no. 2, pp. 1752-1755, 2007, doi: 10.1109/TASC.2007.897763.

[16] J. T. Kephart, B. K. Fitzpatrick, P. Ferrara, M. Pyryt, J. Pienkos, and E. M. Golda, "High Temperature Superconducting Degaussing from Feasibility Study to Fleet Adoption," *IEEE transactions on applied superconductivity,* vol. 21, no. 3, pp. 2229-2232, 2011, doi: 10.1109/TASC.2010.2092746.

[17] H. Hosono *et al.*, "Exploration of New Superconductors and Functional Materials, and Fabrication of Superconducting Tapes and Wires of Iron Pnictides," *Science and technology of advanced materials,* vol. 16, no. 3, p. 33503, 2015, doi: 10.1088/1468-6996/16/3/033503.

[18] Y. Duan and Y. Gao, "Delamination and Current-Carrying Degradation Behavior of Epoxy-Impregnated Superconducting Coil Winding with 2g Hts Tape Caused by Thermal Stress," *AIP advances,* vol. 10, no. 2, pp. 025320-025320-13, 2020.

[19] V. E. Sytnikov, V. S. Vysotsky, I. P. Radchenko, and N. V. Polyakova, "1g Versus 2g-Comparison from the Practical Standpoint for Hts Power Cables Use," *Journal of physics. Conference series,* vol. 97, no. 1, p. 012058, 2008, doi: 10.1088/1742-6596/97/1/012058.

[20] H. Laquer, J. Dean, and P. Chowdhuri, "Electrical, Cryogenic and Systems Design of a Dc Superconducting Power Transmission Line," *IEEE transactions on magnetics,* vol. 13, no. 1, pp. 182-187, 1977, doi: 10.1109/TMAG.1977.1059388.

[21] J. A. Demko *et al.,* "Cryostat Vacuum Thermal Considerations for Hts Power Transmission Cable Systems," *IEEE transactions on applied superconductivity,* vol. 13, no. 2, pp. 1930-1933, 2003, doi: 10.1109/TASC.2003.812956.

[22] A. Morandi, "Hts Dc Transmission and Distribution: Concepts, Applications and Benefits," *Superconductor science & technology,* vol. 28, no. 12, p. 123001, 2015, doi: 10.1088/0953-2048/28/12/123001.

[23] D. Miyagi *et al.,* "The Shielding Effect of Hts Power Cable Based on E-J Power Law," *IEEE transactions on applied superconductivity,* vol. 14, no. 2, pp. 654-657, 2004, doi: 10.1109/TASC.2004.830019.

[24] D. Evans, "Turn, Layer and Ground Insulation for Superconducting Magnets," *Physica. C, Superconductivity,* vol. 354, no. 1, pp. 136-142, 2001, doi: 10.1016/S0921-4534(01)00135-6.

[25] M. Kosaki, "Research and Development of Electrical Insulation of Superconducting Cables by Extruded Polymers," *IEEE electrical insulation magazine,* vol. 12, no. 5, pp. 17-24, 1996, doi: 10.1109/57.537191.

[26] W. J. Kim, H. J. Kim, J. W. Cho, and S. H. Kim, "The Basic Properties of Pplp for Hts Dc Cable," *Physics procedia,* vol. 45, pp. 293-296, 2013, doi: 10.1016/j.phpro.2013.05.025.

[27] A. Ballarino. "Hts at Cern & Lhc Current Leads." (accessed 2022).

[28] M. E. Baz, "Nexans Installs and Commissions Superconducting Cable for Chicago's Resilient Electric Grid Project," ed: Nexans, 2021.

[29] H. Rodrigo, K. Dongsoon, L. Graber, B. Trociewitz, and S. Pamidi, "Ac Flashover Voltages Along Epoxy Surfaces in Gaseous Helium Compared to Liquid Nitrogen and Transformer Oil," *IEEE transactions on applied superconductivity,* vol. 24, no. 3, pp. 1-6, 2014, doi: 10.1109/TASC.2013.2286744.

[30] S. Pamidi, C. H. Kim, J.-H. Kim, D. Crook, and S. Dale, "Cryogenic Helium Gas Circulation System for Advanced Characterization of Superconducting Cables and Other Devices," *Cryogenics (Guildford),* vol. 52, no. 4-6, pp. 315-320, 2012, doi: 10.1016/j.cryogenics.2011.09.006.

[31] J. Gerhold and T. Tanaka, "Cryogenic Electrical Insulation of Superconducting Power Transmission Lines : Transfer of Experience Learned from Metal Superconductors to High Critical Temperature Superconductors: Electrical Insulation in Superconducting Power Apparatus," *Cryogenics (Guildford),* vol. 38, no. 11, pp. 1173-1188, 1998.

[32] M. Kosaki *et al.*, "Development and Tests of Extruded Ethylenepropylene-Rubber-Insulated Superconducting Cable," *Cryogenics,* vol. 35, no. 11, pp. 805-807, 1995/11/01/ 1995, doi: 10.1016/0011-2275(95)90920-B.

[33] P. Cheetham, J. Viquez, W. Kim, L. Graber, C. H. Kim, and S. V. Pamidi, "High-Temperature Superconducting Cable Design Based on Individual Insulated Conductors," *Advances in Materials Science and Engineering,* vol. 2018, p. 3637873, 2018/11/01 2018.

[34] X. Yang, M. Song, K. N. Cao, D. D. Wang, and B. Wei, "Dielectric Characteristics of Laminated Paper and Polymer Sheets Used for Lapping Dielectric Structure at 77 K," *IEEE transactions on applied superconductivity,* vol. 24, no. 5, pp. 1-4, 2014, doi: 10.1109/TASC.2014.2351259.

[35] M. O. Pace, I. Sauers, D. R. James, and A. R. Ellis, "Aging of Lapped Tape Insulated Model Cables at Cryogenic Temperature," Piscataway NJ, 2002: IEEE, pp. 27-30, doi: 10.1109/CEIDP.2002.1048728.

[36] D. G. Yang *et al.*, "Quench and Recovery Characteristics of the Zr-Doped (Gd,Y) Bco Coated Conductor Pancake Coils Insulated with Copper and Kapton Tapes," *IEEE transactions on applied superconductivity,* vol. 21, no. 3, pp. 2415-2419, 2011, doi: 10.1109/TASC.2010.2090323.

[37] N. Hayakawa, T. Matsuoka, H. Kojima, S. Isojima, and M. Kuwata, "Breakdown Characteristics and Mechanisms of Liquid Nitrogen under Transient Thermal Stress for Superconducting Fault Current Limiters," *IEEE transactions on applied superconductivity,* vol. 27, no. 4, pp. 1-5, 2017, doi: 10.1109/TASC.2017.2651115.

[38] N. Meurice, E. Sandre, A. Aslanides, and D. P. Vercauteren, "Simple Theoretical Estimation of the Dielectric Strength of Gases," *IEEE transactions on dielectrics and electrical insulation,* vol. 11, no. 6, pp. 946-948, 2004, doi: 10.1109/TDEI.2004.1387817.

[39] M. Hara and H. Okubo, "Electrical Insulation Characteristics of Superconducting Power Apparatus: Electrical Insulation in Superconducting Power Apparatus," *Cryogenics (Guildford),* vol. 38, no. 11, pp. 1083-1093, 1998.

[40] "Dupont™ Kapton ® Summary of Properties," Dupont, 2021.

[41] "Technical Bulletin of Pyre-M.L.," I.S.T. Corporation, 2022.

[42] E. Cuninková, M. Pekarčíková, M. Skarba, J. Krajčovič, and M. Pašák, "Experimental and Numerical Analysis of High-Temperature Superconducting Tapes Modified by Composite Thermal Stabilization Subjected to Thermomechanical Loading," *Materials,* vol. 14, no. 13, p. 3579, 2021.

[43] B. A. Glowacki and M. Mosiadz, "The Role of Sol Gel Processing in the Development of High-Temperature Superconductors for Ac Applications," *Journal of sol-gel science and technology,* vol. 51, no. 3, pp. 335-347, 2009, doi: 10.1007/s10971-009-1980-8.

[44] A. C. Balazs, T. Emrick, and T. P. Russell, "Nanoparticle Polymer Composites: Where Two Small Worlds Meet," *Science (American Association for the Advancement of Science),* vol. 314, no. 5802, pp. 1107-1110, 2006, doi: 10.1126/science.1130557.

[45] P. Nguyen-Tri, T. A. Nguyen, P. Carriere, and C. Ngo Xuan, "Nanocomposite Coatings: Preparation, Characterization, Properties, and Applications," *International journal of corrosion,* vol. 2018, pp. 1-19, 2018, doi: 10.1155/2018/4749501.

[46] A. Toor, H. So, and A. P. Pisano, "Improved Dielectric Properties of Polyvinylidene Fluoride Nanocomposite Embedded with Poly(Vinylpyrrolidone)-Coated Gold Nanoparticles," *ACS applied materials & interfaces,* vol. 9, no. 7, pp. 6369-6375, 2017, doi: 10.1021/acsami.6b13900.

[47] M. Sudheer, R. Prabhu, K. Raju, and T. Bhat, "Effect of Filler Content on the Performance of Epoxy/Ptw Composites," *Advances in materials science and engineering,* vol. 2014, pp. 1-11, 2014, doi: 10.1155/2014/970468.

[48] A. Dasari, Z.-Z. Yu, and Y.-W. Mai, *Polymer Nanocomposites: Towards Multi-Functionality* (Engineering Materials and Processes). London: Springer London, Limited, 2016.

[49] X. Shi, T. A. Nguyen, Z. Suo, Y. Liu, and R. Avci, "Effect of Nanoparticles on the Anticorrosion and Mechanical Properties of Epoxy Coating," *Surface & coatings technology,* vol. 204, no. 3, pp. 237-245, 2009, doi: 10.1016/j.surfcoat.2009.06.048.

[50] M. A. Alam, U. A. Samad, M. Alam, A. Anis, and S. M. Al-Zahrani, "Enhancement in Nanomechanical, Thermal, and Abrasion Properties of Sio_2 Nanoparticle-Modified Epoxy Coatings," *Coatings (Basel),* vol. 10, no. 4, p. 310, 2020, doi: 10.3390/coatings10040310.

[51] V. C. Shunmugasamy, C. Xiang, and N. Gupta, "Clay/Polymer Nanocomposites: Processing, Properties, and Applications." Cham: Springer International Publishing, 2015, pp. 161-200.

[52] G. Shi, M. Q. Zhang, M. Z. Rong, B. Wetzel, and K. Friedrich, "Friction and Wear of Low Nanometer Si_3n_4 Filled Epoxy Composites," *Wear,* vol. 254, no. 7-8, pp. 784-796, 2003, doi: 10.1016/S0043-1648(03)00190-X.

[53] Y. Bai, Z. Y. Cheng, V. Bharti, H. S. Xu, and Q. M. Zhang, "High-Dielectric-Constant Ceramic-Powder Polymer Composites," *Applied physics letters,* vol. 76, no. 25, pp. 3804-3806, 2000, doi: 10.1063/1.126787.

[54] X. Huang, P. Jiang, and L. Xie, "Ferroelectric Polymer/Silver Nanocomposites with High Dielectric Constant and High Thermal Conductivity," *Applied physics letters,* vol. 95, no. 24, pp. 242901-242901-3, 2009, doi: 10.1063/1.3273368.

[55] G. M. Ouyang, K. Y. Wang, and X. Y. Chen, "Enhanced Electro-Mechanical Performance of Tio2 Nano-Particle Modified Polydimethylsiloxane (Pdms) as Electroactive Polymers," 2011: IEEE, pp. 614-617, doi: 10.1109/TRANSDUCERS.2011.5969778.

[56] M. Rajib *et al.*, "Enhanced Energy Storage of Dielectric Nanocomposites at Elevated Temperatures," *International journal of applied ceramic technology*, vol. 13, no. 1, pp. 125-132, 2016, doi: 10.1111/ijac.12410.

[57] R. Huang, Z. Chen, X. Chu, Z. Wu, and L. Li, "Preparation and Thermal Properties of Epoxy Composites Filled with Negative Thermal Expansion Nanoparticles Modified by a Plasma Treatment," *Journal of composite materials*, vol. 45, no. 16, pp. 1675-1682, 2011, doi: 10.1177/0021998310385031.

[58] C. J. Huang, S. Y. Fu, Y. H. Zhang, B. Lauke, L. F. Li, and L. Ye, "Cryogenic Properties of Sio_2/Epoxy Nanocomposites," *Cryogenics*, vol. 45, no. 6, pp. 450-454, 2005/06/01/ 2005, doi: 10.1016/j.cryogenics.2005.03.003.

[59] S. Kang, S. I. Hong, C. R. Choe, M. Park, S. Rim, and J. Kim, "Preparation and Characterization of Epoxy Composites Filled with Functionalized Nanosilica Particles Obtained Via Sol-Gel Process," *Polymer (Guilford)*, vol. 42, no. 3, pp. 879-887, 2001, doi: 10.1016/S0032-3861(00)00392-X.

[60] Y.-J. Kim, J.-H. Kim, S.-W. Ha, D. Kwon, and J.-K. Lee, "Polyimide Nanocomposites with Functionalized Sio_2 Nanoparticles: Enhanced Processability, Thermal and Mechanical Properties," *RSC advances*, vol. 4, no. 82, pp. 43371-43377, 2014, doi: 10.1039/c4ra04952g.

[61] J. F. Heacock and C. E. Berr, "Polyimides-New High Temperature Polymers: H-Film, a Polypyromellitimide Film," *Polymer engineering and science*, vol. 5, no. 2, pp. 105-110, 1965, doi: 10.1002/pen.760050207.

[62] S. Diaham, S. Zelmat, M. L. Locatelli, S. Dinculescu, M. Decup, and T. Lebey, "Dielectric Breakdown of Polyimide Films: Area, Thickness and Temperature Dependence," *IEEE transactions on dielectrics and electrical insulation*, vol. 17, no. 1, pp. 18-27, 2010, doi: 10.1109/TDEI.2010.5411997.

[63] M. McCaffrey, H. Hones, J. Cook, R. Krchnavek, and W. Xue, "Geometric Analysis of Dielectric Failures in Polyimide/Silicon Dioxide Nanocomposites," *Polymer engineering and science*, vol. 59, no. 9, pp. 1897-1904, 2019, doi: 10.1002/pen.25190.

[64] J. Cook, H. Hones, J. Mahon, L. Yu, R. Krchnavek, and W. Xue, "Temperature-Dependent Dielectric Properties of Polyimide (Pi) and Polyamide (Pa) Nanocomposites," *IEEE transactions on nanotechnology,* vol. 20, pp. 584-591, 2021.

[65] X. Huang, Y. Zheng, P. Jiang, and Y. Yin, "Influence of Nanoparticle Surface Treatment on the Electrical Properties of Cycloaliphatic Epoxy Nanocomposites," *IEEE transactions on dielectrics and electrical insulation,* vol. 17, no. 2, pp. 635-643, 2010, doi: 10.1109/TDEI.2010.5448121.

[66] K. Woo-Jin *et al.,* "Comparative Study of Cryogenic Dielectric and Mechanical Properties of Insulation Materials for Helium Gas Cooled Hts Power Devices," *IEEE transactions on applied superconductivity,* vol. 27, no. 4, pp. 1-5, 2017, doi: 10.1109/TASC.2016.2642581.

[67] J. K. Nelson, *Dielectric Polymer Nanocomposites,* 1st ed. 2010. ed. New York, NY: Springer US, 2010.

[68] L. S. Schadler, L. C. Brinson, and W. G. Sawyer, "Polymer Nanocomposites: A Small Part of the Story," *JOM (1989),* vol. 59, no. 3, pp. 53-60, 2007, doi: 10.1007/s11837-007-0040-5.

[69] V. I. Vettegren', A. Y. Bashkarev, and M. A. Suslov, "Effect of the Shape and Concentration of Filler Particles on the Thermal Expansion of Polymer Composites," *Technical physics,* vol. 52, no. 10, pp. 1383-1386, 2007, doi: 10.1134/S1063784207100246.

[70] L. S. Schadler, S. K. Kumar, B. C. Benicewicz, S. L. Lewis, and S. E. Harton, "Designed Interfaces in Polymer Nanocomposites: A Fundamental Viewpoint," *MRS Bulletin,* vol. 32, no. 4, pp. 335-340, 2007/04/01 2007, doi: 10.1557/mrs2007.232.

[71] T. Tanaka, Y. Ohki, M. Ochi, M. Harada, and T. Imai, "Enhanced Partial Discharge Resistance of Epoxy/Clay Nanocomposite Prepared by Newly Developed Organic Modification and Solubilization Methods," *IEEE transactions on dielectrics and electrical insulation,* vol. 15, no. 1, pp. 81-89, 2008, doi: 10.1109/T-DEI.2008.4446739.

[72] D.-J. Liaw, K.-L. Wang, Y.-C. Huang, K.-R. Lee, J.-Y. Lai, and C.-S. Ha, "Advanced Polyimide Materials: Syntheses, Physical Properties and

Applications," *Progress in polymer science,* vol. 37, no. 7, pp. 907-974, 2012, doi: 10.1016/j.progpolymsci.2012.02.005.

[73] J. W. Ekin, *Experimental Techniques for Low-Temperature Measurements Cryostat Design, Material Properties, and Superconductor Critical-Current Testing*. Oxford: Oxford University Press, 2006.

[74] "Pyre-M.L.® Polyimide Varnish for Heat-Resistant Insulation Coating." I.S.T Corporation. (accessed.

[75] "Poly(Pyromellitic Dianhydride-Co-4,4′-Oxydianiline), Amic Acid Solution." Sigma-Aldrich. (accessed.

[76] P. J. Yoon, T. D. Fornes, and D. R. Paul, "Thermal Expansion Behavior of Nylon 6 Nanocomposites," *Polymer (Guilford),* vol. 43, no. 25, pp. 6727-6741, 2002, doi: 10.1016/S0032-3861(02)00638-9.

[77] E. Manias, "Nanocomposites Stiffer by Design," *Nature materials,* vol. 6, no. 1, pp. 9-11, 2007, doi: 10.1038/nmat1812.

[78] "Loctite Stycast 2850ft Technical Data Sheet," Henkel Corporation, 2015.

[79] H. Mahfuz *et al.,* "Reinforcement of Nylon 6 with Functionalized Silica Nanoparticles for Enhanced Tensile Strength and Modulus," *Nanotechnology,* vol. 19, no. 44, pp. 445702-445702, 2008, doi: 10.1088/0957-4484/19/44/445702.

[80] H. Zhang, Z. Zhang, K. Friedrich, and C. Eger, "Property Improvements of in Situ Epoxy Nanocomposites with Reduced Interparticle Distance at High Nanosilica Content," *Acta materialia,* vol. 54, no. 7, pp. 1833-1842, 2006, doi: 10.1016/j.actamat.2005.12.009.

[81] G. M. Odegard, T. C. Clancy, and T. S. Gates, "Modeling of the Mechanical Properties of Nanoparticle/Polymer Composites," *Polymer (Guilford),* vol. 46, no. 2, pp. 553-562, 2005, doi: 10.1016/j.polymer.2004.11.022.

[82] F.-A. Zhang, D.-K. Lee, and T. J. Pinnavaia, "Pmma/Mesoporous Silica Nanocomposites: Effect of Framework Structure and Pore Size on Thermomechanical Properties," *Polymer chemistry,* vol. 1, no. 1, pp. 107-113, 2010, doi: 10.1039/b9py00232d.

[83] O. Becker, R. J. Varley, and G. P. Simon, "Thermal Stability and Water Uptake of High Performance Epoxy Layered Silicate Nanocomposites," *European polymer journal*, vol. 40, no. 1, pp. 187-195, 2004, doi: 10.1016/j.eurpolymj.2003.09.008.

[84] C. J. Brinker, G. C. Frye, A. J. Hurd, and C. S. Ashley, "Fundamentals of Sol-Gel Dip Coating," *Thin Solid Films*, vol. 201, no. 1, pp. 97-108, 1991/06/05/ 1991, doi: 10.1016/0040-6090(91)90158-T.

[85] S. Tabatabaei, A. Shukohfar, R. Aghababazadeh, and A. Mirhabibi, "Experimental Study of the Synthesis and Characterisation of Silica Nanoparticles Via the Sol-Gel Method," *Journal of physics. Conference series*, vol. 26, no. 1, pp. 371-374, 2006, doi: 10.1088/1742-6596/26/1/090.

[86] "Zytel® 101 Nc010 Nylon Resin Pa66 Datasheet," DuPont de Nemours, Inc., 2022.

[87] "Fused Silica, Sio_2 Glass Properties," Accuratus Corporation, 2013.

[88] T. Tanaka, "Dielectric Nanocomposites with Insulating Properties," *IEEE transactions on dielectrics and electrical insulation*, vol. 12, no. 5, pp. 914-928, 2005, doi: 10.1109/TDEI.2005.1522186.

[89] T. Tanaka, G. C. Montanari, and R. Mulhaupt, "Polymer Nanocomposites as Dielectrics and Electrical Insulation-Perspectives for Processing Technologies, Material Characterization and Future Applications," *IEEE transactions on dielectrics and electrical insulation*, vol. 11, no. 5, pp. 763-784, 2004, doi: 10.1109/TDEI.2004.1349782.

[90] H. Liu and L. C. Brinson, "Reinforcing Efficiency of Nanoparticles: A Simple Comparison for Polymer Nanocomposites," *Composites science and technology*, vol. 68, no. 6, pp. 1502-1512, 2008, doi: 10.1016/j.compscitech.2007.10.033.

[91] L. Liu, A. H. Barber, S. Nuriel, and H. D. Wagner, "Mechanical Properties of Functionalized Single-Walled Carbon-Nanotube/Poly(Vinyl Alcohol) Nanocomposites," *Advanced Functional Materials*, vol. 15, no. 6, pp. 975-980, 2005, doi: 10.1002/adfm.200400525.

[92] P. O. Henk, T. W. Kortsen, and T. Kvarts, "Increasing the Electrical Discharge Endurance of Acid Anhydride Cured Dgeba Epoxy Resin by Dispersion of

Nanoparticle Silica," *High performance polymers,* vol. 11, no. 3, pp. 281-296, 1999, doi: 10.1088/0954-0083/11/3/304.

[93] L. Schadler, "Nanocomposites Model Interfaces," *Nature materials,* vol. 6, no. 4, pp. 257-258, 2007, doi: 10.1038/nmat1873.

[94] T. J. Lewis, "Interfaces Are the Dominant Feature of Dielectrics at the Nanometric Level," *IEEE transactions on dielectrics and electrical insulation,* vol. 11, no. 5, pp. 739-753, 2004, doi: 10.1109/TDEI.2004.1349779.

[95] H. Shi, T. Lan, and T. J. Pinnavaia, "Interfacial Effects on the Reinforcement Properties of Polymer−Organoclay Nanocomposites," *Chemistry of materials,* vol. 8, no. 8, pp. 1584-1587, 1996, doi: 10.1021/cm960227m.

[96] A. Dasari, Z.-Z. Yu, and Y.-W. Mai, "Effect of Blending Sequence on Microstructure of Ternary Nanocomposites," *Polymer (Guilford),* vol. 46, no. 16, pp. 5986-5991, 2005, doi: 10.1016/j.polymer.2005.05.145.

[97] S. Li, G. Yin, S. Bai, and J. Li, "A New Potential Barrier Model in Epoxy Resin Nanodielectrics," *IEEE transactions on dielectrics and electrical insulation,* vol. 18, no. 5, pp. 1535-1543, 2011, doi: 10.1109/TDEI.2011.6032822.

[98] S. Raetzke and J. Kindersberger, "The Effect of Interphase Structures in Nanodielectrics," *IEEJ Transactions on Fundamentals and Materials,* vol. 126, pp. 1044-1049, January 01, 2006 2006, doi: 10.1541/ieejfms.126.1044.

[99] T. Tanaka, M. Kozako, N. Fuse, and Y. Ohki, "Proposal of a Multi-Core Model for Polymer Nanocomposite Dielectrics," *IEEE transactions on dielectrics and electrical insulation,* vol. 12, no. 4, pp. 669-681, 2005, doi: 10.1109/TDEI.2005.1511092.

[100] N. Shi and R. Ramprasad, "Local Properties at Interfaces in Nanodielectrics: An Ab Initio Computational Study," *IEEE transactions on dielectrics and electrical insulation,* vol. 15, no. 1, pp. 170-177, 2008, doi: 10.1109/T-DEI.2008.4446748.

[101] D. Min *et al.,* "Carrier Transport and Molecular Displacement Modulated Dc Electrical Breakdown of Polypropylene Nanocomposites," *Polymers,* vol. 10, no. 11, p. 1207, 2018, doi: 10.3390/polym10111207.

[102] P. B. Messersmith and E. P. Giannelis, "Synthesis and Barrier Properties of Poly(E-Caprolactone)-Layered Silicate Nanocomposites," *Journal of polymer science. Part A, Polymer chemistry*, vol. 33, no. 7, pp. 1047-1057, 1995, doi: 10.1002/pola.1995.080330707.

[103] T. Schneller, R. Waser, M. Kosec, and D. Payne, *Chemical Solution Deposition of Functional Oxide Thin Films*, 1st ed. 2013. ed. Vienna: Springer Vienna, 2013.

[104] X.-D. Wang *et al.*, "Preparation of Spherical Silica Particles by Stöber Process with High Concentration of Tetra-Ethyl-Orthosilicate," *Journal of colloid and interface science*, vol. 341, no. 1, pp. 23-29, 2010, doi: 10.1016/j.jcis.2009.09.018.

[105] I. A. M. Ibrahim, A. A. F. Zikry, and M. A. Sharaf, "Preparation of Spherical Silica Nanoparticles: Stober Silica," *Journal of American Science*, 2010.

[106] W. Stöber, A. Fink, and E. Bohn, "Controlled Growth of Monodisperse Silica Spheres in the Micron Size Range," *Journal of Colloid and Interface Science*, vol. 26, no. 1, pp. 62-69, 1968/01/01/ 1968, doi: 10.1016/0021-9797(68)90272-5.

[107] R. Aelion, A. Loebel, and F. Eirich, "The Hydrolysis and Polycondensation of Tetra Alkoxysilanes," *Recueil des Travaux Chimiques des Pays-Bas*, vol. 69, no. 1, pp. 61-75, 1950, doi: 10.1002/recl.19500690109.

[108] M. H. Hones, "Polyimide / Silicon Dioxide Nanocomposites as Dielectrics for Helium-Cooled High-Temperature Superconducting Cables," Rowan University, Glassboro, N.J, 2020.

[109] W. Chen, W. Chen, B. Zhang, S. Yang, and C.-Y. Liu, "Thermal Imidization Process of Polyimide Film: Interplay between Solvent Evaporation and Imidization," *Polymer (Guilford)*, vol. 109, pp. 205-215, 2017, doi: 10.1016/j.polymer.2016.12.037.

[110] W. Chen, W. Chen, B. Zhang, S. Yang, and C.-Y. Liu, "Thermal Imidization Process of Polyimide Film: Interplay between Solvent Evaporation and Imidization," *Polymer*, vol. 109, pp. 205-215, 2017/01/27/ 2017, doi: 10.1016/j.polymer.2016.12.037.

[111] J. I. Goldstein, D. E. Newbury, J. R. Michael, N. W. M. Ritchie, J. H. J. Scott, and D. C. Joy, *Scanning Electron Microscopy and X-Ray Microanalysis*, 4th ed. 2018. ed. New York, NY: Springer New York, 2018.

[112] W. N. Sharpe, B. Yuan, and R. L. Edwards, "A New Technique for Measuring the Mechanical Properties of Thin Films," *Journal of microelectromechanical systems*, vol. 6, no. 3, pp. 193-199, 1997.

[113] O. Kraft and C. A. Volkert, "Mechanical Testing of Thin Films and Small Structures," *Advanced engineering materials*, vol. 3, no. 3, pp. 99-110, 2001.

[114] W. P. Vellinga, M. Van den Bosch, and M. G. D. Geers, "Interaction between Cracking, Delamination and Buckling in Brittle Elastic Thin Films," *International journal of fracture*, vol. 154, no. 1-2, pp. 195-209, 2008.

[115] S. Mandal, D. Roy, N. E. Prasad, and M. Joshi, "Interfacial Interactions and Properties of Cellular Structured Polyurethane Nanocomposite Based on Carbonaceous Nano-Fillers," *Journal of applied polymer science*, vol. 138, no. 2, p. n/a, 2021.

[116] *Standard Test Method for Tensile Properties of Thin Plastic Sheeting*, ASTM, ASTM Standard D882-18, 2018.

[117] J. James, "Chapter 7 - Thermomechanical Analysis and Its Applications," in *Thermal and Rheological Measurement Techniques for Nanomaterials Characterization*, S. Thomas, R. Thomas, A. K. Zachariah, and R. K. Mishra Eds.: Elsevier, 2017, pp. 159-171.

[118] L. B. Chen, S. X. Liu, K. X. Gu, Y. Zhou, and J. J. Wang, "A Cryogenic Tensile Testing Apparatus for Micro-Samples Cooled by Miniature Pulse Tube Cryocooler," *IOP conference series. Materials Science and Engineering*, vol. 102, no. 1, p. 12011, 2015.

[119] C. Compton, S. K. Chandrasekaran, D. Baars, T. Bieler, P. Darbandi, and N. Wright, "Development of a Cryogenic Mechanical Property Testing Station for Superconducting Rf Cavity Material," *AIP Conference Proceedings*, vol. 1218, no. 1, pp. 587-594, 2010/04/09 2010.

[120] P. Cruz, E. D. Shoemake, P. Adam, and J. Leachman, "Tensile Strengths of Polyamide Based 3d Printed Polymers in Liquid Nitrogen," *IOP conference series. Materials Science and Engineering,* vol. 102, no. 1, p. 12020, 2015.

[121] A. Díaz-Parralejo, M. Á. Díaz-Díez, J. Sánchez-González, A. Macías-García, and J. P. Carrasco-Amador, "Mechanical Properties and Thermal Shock in Thin Zro2–Y2o3–Al2o3 Films Obtained by the Sol-Gel Method," *Ceramics international,* vol. 47, no. 1, pp. 80-86, 2021.

[122] M. Hunt, K. Salmon, J. Haney, C. Evans, A. Gozen, and J. Leachman, "Ultimate Tensile Strengths of 3d Printed Carbon-Fiber Reinforced Thermoplastics in Liquid Nitrogen," *IOP conference series. Materials Science and Engineering,* vol. 755, no. 1, p. 12118, 2020.

[123] J. Lepetit, R. Favier, A. Grajales, and P. O. Skjervold, "A Simple Cryogenic Holder for Tensile Testing of Soft Biological Tissues," *Journal of biomechanics,* vol. 37, no. 4, pp. 557-562, 2004.

[124] K. Kasaba *et al.,* "Advanced Tensile Testing Methods for Bulk Superconductors at Cryogenic Temperatures," *Physica. C, Superconductivity,* vol. 445-448, pp. 427-430, 2006.

[125] M. O. Riekerink, "Structural and Chemical Modification of Polymer Surfaces by Gas Plasma Etching," PhD Thesis, Universiteit Twente, 2001.

[126] H. Puliyalil and U. Cvelbar, "Selective Plasma Etching of Polymeric Substrates for Advanced Applications," *Nanomaterials (Basel, Switzerland),* vol. 6, no. 6, p. 108, 2016, doi: 10.3390/nano6060108.

[127] F. D. Egitto, "Plasma Etching and Modification of Organic Polymers," *Pure and applied chemistry,* vol. 62, no. 9, pp. 1699-1708, 1990, doi: 10.1351/pac199062091699.

[128] "Plasma Prep Iii™ Solid State Low Temperature Asher/Etcher Operation Manual," Structure Probe, Inc. / SPI Supplies, 2022.

[129] G. N. Taylor and T. M. Wolf, "Oxygen Plasma Removal of Thin Polymer Films," *Polymer engineering and science,* vol. 20, no. 16, pp. 1087-1092, 1980, doi: 10.1002/pen.760201610.

[130] C. J. Huang, S. Y. Fu, Y. H. Zhang, B. Lauke, L. F. Li, and L. Ye, "Cryogenic Properties of Sio2/Epoxy Nanocomposites," *Cryogenics (Guildford)*, vol. 45, no. 6, pp. 450-454, 2005, doi: 10.1016/j.cryogenics.2005.03.003.

[131] J. E. Campbell, E. A. Eldridge, and J. K. Thompson, "Handbook on Materials for Superconducting Machinery," 1974.

[132] Y. Zare and H. Garmabi, "Analysis of Tensile Modulus of Pp/Nanoclay/Caco3 Ternary Nanocomposite Using Composite Theories," *Journal of applied polymer science*, vol. 123, no. 4, pp. 2309-2319, 2012, doi: 10.1002/app.34741.

[133] L. E. Nielsen, "Modern Composite Materials," *Journal of Polymer Science Part A-2: Polymer Physics*, vol. 7, no. 12, pp. 2140-2141, 1969/12/01 1969, doi: 10.1002/pol.1969.160071214.

[134] E. Sparks, "High-Performance Ballistic Protection Using Polymer Nanocomposites," Woodhead Publishing, 2012, pp. 1-1.

[135] C.-L. Chiang, C.-C. M. Ma, D.-L. Wu, and H.-C. Kuan, "Preparation, Characterization, and Properties of Novolac-Type Phenolic/Sio2 Hybrid Organic-Inorganic Nanocomposite Materials by Sol-Gel Method," *Journal of polymer science. Part A, Polymer chemistry*, vol. 41, no. 7, pp. 905-913, 2003, doi: 10.1002/pola.10624.

[136] G. Ragosta, M. Abbate, P. Musto, G. Scarinzi, and L. Mascia, "Epoxy-Silica Particulate Nanocomposites: Chemical Interactions, Reinforcement and Fracture Toughness," *Polymer (Guilford)*, vol. 46, no. 23, pp. 10506-10516, 2005, doi: 10.1016/j.polymer.2005.08.028.

[137] K. Tanaka and H. Kozuka, "Sol–Gel Preparation and Mechanical Properties of Machinable Cellulose/Silica and Polyvinylpyrrolidone/Silica Composites," *Journal of sol-gel science and technology*, vol. 32, no. 1, pp. 73-77, 2004, doi: 10.1007/s10971-004-5768-6.

[138] W. Naous, X.-Y. Yu, Q.-X. Zhang, K. Naito, and Y. Kagawa, "Morphology, Tensile Properties, and Fracture Toughness of Epoxy/Al2o3 Nanocomposites," *Journal of polymer science. Part B, Polymer physics*, vol. 44, no. 10, pp. 1466-1473, 2006, doi: 10.1002/polb.20800.

[139] S. Deng, L. Ye, and K. Friedrich, "Fracture Behaviours of Epoxy Nanocomposites with Nano-Silica at Low and Elevated Temperatures," *Journal of materials science,* vol. 42, no. 8, pp. 2766-2774, 2007, doi: 10.1007/s10853-006-1420-x.

[140] D. Eiras and L. A. Pessan, "Mechanical Properties of Polypropylene/Calcium Carbonate Nanocomposites," *Materials research (São Carlos, São Paulo, Brazil),* vol. 12, no. 4, pp. 517-522, 2009, doi: 10.1590/S1516-14392009000400023.

[141] J. W. Cho and S. H. Lee, "Influence of Silica on Shape Memory Effect and Mechanical Properties of Polyurethane–Silica Hybrids," *European polymer journal,* vol. 40, no. 7, pp. 1343-1348, 2004, doi: 10.1016/j.eurpolymj.2004.01.041.

[142] D. Shah *et al.*, "Dramatic Enhancements in Toughness of Polyvinylidene Fluoride Nanocomposites Via Nanoclay-Directed Crystal Structure and Morphology," *Advanced materials (Weinheim),* vol. 16, no. 14, pp. 1173-1177, 2004, doi: 10.1002/adma.200306355.

[143] X. Duan, H. Yuan, W. Tang, J. He, and X. Guan, "A General Temperature-Dependent Stress-Strain Constitutive Model for Polymer-Bonded Composite Materials," (in eng), *Polymers,* vol. 13, no. 9, p. 1393, 2021, doi: 10.3390/polym13091393.

[144] G. Bao and Z. Suo, "Remarks on Crack-Bridging Concepts," *Applied Mechanics Reviews,* vol. 45, no. 8, pp. 355-366, 1992, doi: 10.1115/1.3119764.

[145] B. B. Johnsen, A. J. Kinloch, R. D. Mohammed, A. C. Taylor, and S. Sprenger, "Toughening Mechanisms of Nanoparticle-Modified Epoxy Polymers," *Polymer (Guilford),* vol. 48, no. 2, pp. 530-541, 2007, doi: 10.1016/j.polymer.2006.11.038.

[146] A. A. Abdel-Wahab, S. Ataya, and V. V. Silberschmidt, "Temperature-Dependent Mechanical Behaviour of Pmma: Experimental Analysis and Modelling," *Polymer testing,* vol. 58, pp. 86-95, 2017, doi: 10.1016/j.polymertesting.2016.12.016.

[147] R. Li, Z. Shi, D. Kuang, and J. Pei, "The Electrical Performance of Polyamide 66/Poly(Vinylidene Fluoride) with Vinyl Acetate-Maleic Anhydride Copolymer," *International journal of polymer science,* vol. 2016, pp. 1-5, 2016, doi: 10.1155/2016/3580820.

[148] R. H. Hansen, J. V. Pascale, T. De Benedictis, and P. M. Rentzepis, "Effect of Atomic Oxygen on Polymers," *Journal of Polymer Science Part A: General Papers,* vol. 3, no. 6, pp. 2205-2214, 1965/06/01 1965, doi: 10.1002/pol.1965.100030609.

[149] A. G. Evans, S. Williams, and P. W. R. Beaumont, "On the Toughness of Particulate Filled Polymers," *Journal of Materials Science,* vol. 20, no. 10, pp. 3668-3674, 1985/10/01 1985, doi: 10.1007/BF01113774.

[150] K. Wang, L. Chen, J. Wu, M. L. Toh, C. He, and A. F. Yee, "Epoxy Nanocomposites with Highly Exfoliated Clay: Mechanical Properties and Fracture Mechanisms," *Macromolecules,* vol. 38, no. 3, pp. 788-800, 2005/02/01 2005, doi: 10.1021/ma048465n.

[151] R. Livingston and B. Koohbor, "Characterizing Fiber-Matrix Debond and Fiber Interaction Mechanisms by Full-Field Measurements," *Composites Part C: Open Access,* vol. 7, p. 100229, 2022, doi: 10.1016/j.jcomc.2022.100229.

[152] S. S. Shishvan and A. H. Asghari, "Effects of Particle Shape and Size Distribution on Particle Size-Dependent Flow Strengthening in Metal Matrix Composites," *Scientia Iranica. Transaction B, Mechanical engineering,* vol. 24, no. 3, p. 1091, 2017.

[153] T. Tanaka and A. S. Vaughan, *Tailoring of Nanocomposite Dielectrics : From Fundamentals to Devices and Applications*. Singapore: Pan Stanford Publishing, 2017.

[154] R. C. Smith, "Mechanistic Electrical Behavior of Crosslinked Polyethylene/Silica Nanocomposites," Ph.D., Rensselaer Polytechnic Institute, Ann Arbor, 3385669, 2009.

[155] M. Roy, J. K. Nelson, R. K. MacCrone, and L. S. Schadler, "Candidate Mechanisms Controlling the Electrical Characteristics of Silica/Xlpe Nanodielectrics," *Journal of materials science,* vol. 42, no. 11, pp. 3789-3799, 2007, doi: 10.1007/s10853-006-0413-0.

[156] *Standard Test Method for Dielectric Breakdown Voltage and Dielectric Strength of Solid Electrical Insulating Materials under Direct-Voltage Stress,* ASTM, ASTM D3755-20, 2020.

[157] J. K. Seong, I. J. Seo, J. S. Hwang, and B. W. Lee, "Comparative Evaluation between Dc and Ac Breakdown Characteristic of Dielectric Insulating Materials in Liquid Nitrogen," *IEEE transactions on applied superconductivity*, vol. 22, no. 3, pp. 7701504-7701504, 2012, doi: 10.1109/TASC.2011.2178222.

[158] E. Kuffel, W. S. Zaengl, and J. Kuffel, *High Voltage Engineering Fundamentals*, 2nd ed. ed. Boston: Butterworth-Heinemann, 2000.

[159] S. Li, W. Wang, S. Yu, and H. Sun, "Influence of Hydrostatic Pressure on Dielectric Properties of Polyethylene/Aluminum Oxide Nanocomposites," *IEEE transactions on dielectrics and electrical insulation*, vol. 21, no. 2, pp. 519-528, 2014, doi: 10.1109/TDEI.2013.004131.

[160] M. Tefferi, M. A. Baferani, H. Uehara, and Y. Cao, "The Correlation and Balance of Material Properties for Dc Cable Insulation at Design Field," *IEEE access*, vol. 8, pp. 187840-187847, 2020, doi: 10.1109/ACCESS.2020.3030005.

[161] V. Parma, "Cryostat Design," CERN, 2015.

[162] J. G. Weisend Ii, *Cryostat Design Case Studies, Principles and Engineering*, 1st ed. 2016. ed. (International Cryogenics Monograph Series). Cham: Springer International Publishing, 2016.

[163] J. Gerhold, "Properties of Cryogenic Insulants," *Cryogenics (Guildford)*, vol. 38, no. 11, pp. 1063-1081, 1998, doi: 10.1016/S0011-2275(98)00094-0.

[164] M. Lieberman and A. Lichtenberg, "Principles of Plasma Discharges and Materials Processing: Second Edition," *Principles of Plasma Discharges and Materials Processing, 2nd Edition, by Michael A. Lieberman, Alan J. Lichtenberg, pp. 800. ISBN 0-471-72001-1. Wiley-VCH , September 2003.*, vol. 30, 09/01 2003, doi: 10.1002/0471724254.

[165] W. E. Gifford, "The Gifford-Mcmahon Cycle," in *Advances in Cryogenic Engineering*, Boston, MA, K. D. Timmerhaus, Ed., 1966// 1966: Springer US, pp. 152-159.

[166] "Al330 Cryocoolers." Cryomech, Inc. (accessed 2022).

[167] "Cryofans Datasheet," Sterling Cryogenics, 2014.

[168] P. Danielson, "Vacuum Requirements for Cryogenic Vessels," Normandale Community College, 2020.

[169] G. Behrens, W. Campbell, D. Williams, and S. White, "Guidelines for the Design of Cryogenic Systems," National Radio Astronomy Observatory, Electronics Division Internal Report No. 306, 1997.

[170] G. Ventura and M. Perfetti, *Thermal Properties of Solids at Room and Cryogenic Temperatures*, 1st ed. 2014. ed. (International Cryogenics Monograph Series). Dordrecht: Springer Netherlands, 2014.

[171] R. G. Ross, "Quantifying Mli Thermal Conduction in Cryogenic Applications from Experimental Data," *IOP Conference Series: Materials Science and Engineering*, vol. 101, no. 1, p. 12017, 2015, doi: 10.1088/1757-899X/101/1/012017.

[172] C. W. Keller, G. R. Cunnington, and A. P. Glassford, "Thermal Performance of Multilayer Insulations," National Aeronautics and Space Administration, NASA Lewis Research Center, 1974.

[173] S. Kulsa, "How to Make Cryogenic Multi-Layer Insulation (Mli) Shields," Washington State University, Hydrogen Properties for Energy Research Laboratory, 2020.

[174] G. K. Stefansson, "Mli Blankets," Penn State University, The Habitable Zone Planetary Finder, 2014.

[175] N. G. Wilson, C. Bridgman, and R. J. Grieggs, "Cryogenic Gas Disconnect Joints Used in Cryogenic Accelerator Cold-Gas Distribution Systems," 1991: IEEE, pp. 2459-2461 vol.4, doi: 10.1109/PAC.1991.164999.

[176] W. Umrath, "Fundamentals of Vacuum Technology," Leybold GmbH, 2016.

[177] "Materials for Cryogenic Service: Engineering Properties of Austenitic Stainless Steels," Internation Nickel Limited, Nickel Development Institute, 1974.

[178] R. C. Hibbeler, *Mechanics of Materials*, Third edition. ed. Upper Saddle River, N.J: Prentice Hall, 1997.

[179] "Approval for Use of Conflat (Cf) Flanged Fittings in Pressure Systems under Certain Applications and Conditions Based Upon Analysis, Testing, and Successful Service Experience," Los Alamos National Laboratory, Conduct of Engineering Request for Variance or Alternate Method, 2015.

[180] *Rules for Construction of Pressure Vessels Division 2: Alternative Rules*, T. A. S. o. M. Engineers, Boiler and Pressure Vessel Code-VIII-2, 2021.

[181] "Sensor Packaging and Installation," Lake Shore Cryotronics, Inc., 2021.

[182] J. Artbauer, "Electric Strength of Polymers," *Journal of Physics D Applied Physics,* 1996.

[183] S. Singha and M. J. Thomas, "Dielectric Properties of Epoxy Nanocomposites," *IEEE transactions on dielectrics and electrical insulation,* vol. 15, no. 1, pp. 12-23, 2008, doi: 10.1109/T-DEI.2008.4446732.

[184] S. Li *et al.*, "Short-Term Breakdown and Long-Term Failure in Nanodielectrics: A Review," *IEEE transactions on dielectrics and electrical insulation,* vol. 17, no. 5, pp. 1523-1535, 2010, doi: 10.1109/TDEI.2010.5595554.

[185] M. Ieda, M. Nagao, and M. Hikita, "High-Field Conduction and Breakdown in Insulating Polymers. Present Situation and Future Prospects," *IEEE transactions on dielectrics and electrical insulation,* vol. 1, no. 5, pp. 934-945, 1994, doi: 10.1109/94.326660.

[186] M. F. Frechette *et al.*, "Nanostructured Polymer Microcomposites: A Distinct Class of Insulating Materials," *IEEE transactions on dielectrics and electrical insulation,* vol. 15, no. 1, pp. 90-105, 2008, doi: 10.1109/T-DEI.2008.4446740.

[187] Y. Okubo, M. Kozako, M. Hikita, and N. Kamei, "Evaluation of Dielectric Strength of Tricyclopentadiene / Silica Microcomposites," in *2018 IEEE Conference on Electrical Insulation and Dielectric Phenomena (CEIDP)*, 21-24 Oct. 2018 2018, pp. 594-597, doi: 10.1109/CEIDP.2018.8544821.

[188] W. F. Pasveer *et al.*, "Unified Description of Charge-Carrier Mobilities in Disordered Semiconducting Polymers," *Physical review letters,* vol. 94, no. 20, pp. art.-206601, 2005, doi: 10.1103/PhysRevLett.94.206601.

[189] L. A. Dissado, "Electrical Degradation and Breakdown in Polymers," J. C. Fothergill, Ed., ed. London :: P. Peregrinus, 1992.

[190] C. H. Park, K. Okajima, M. Hara, and M. Akazaki, "Effect of Heat Treatment on Dielectric Strength of Polyethylene Terephthalate under Compressive Stress," *IEEE Transactions on Electrical Insulation,* vol. EI-18, no. 4, pp. 380-389, 1983, doi: 10.1109/TEI.1983.298676.

[191] L. A. Utracki, R. Simha, and A. Garcia-Rejon, "Pressure−Volume−Temperature Dependence of Poly-E-Caprolactam/Clay Nanocomposites," *Macromolecules,* vol. 36, no. 6, pp. 2114-2121, 2003/03/01 2003, doi: 10.1021/ma0215464.

[192] M. Faustini, B. Louis, P. A. Albouy, M. Kuemmel, and D. Grosso, "Preparation of Sol−Gel Films by Dip-Coating in Extreme Conditions," *Journal of physical chemistry. C,* vol. 114, no. 17, pp. 7637-7645, 2010, doi: 10.1021/jp9114755.

[193] B. Van Genabet, A. Schwarz, E. Bruneel, L. Rambausek, I. Van Driessche, and L. Van Langenhove, "Synthesis and Characterization of Copper, Polyimide and Tips-Pentacene Layers for the Development of a Solution Processed Fibrous Transistor," *AIP advances,* vol. 1, no. 4, pp. 42119-042119-10, 2011, doi: 10.1063/1.3656743.

[194] L. Rambausek, E. Bruneel, I. Van Driessche, and L. Van Langenhove, "Surface Morphology of Polyimide Thin Film Dip-Coated on Polyester Filament for Dielectric Layer in Fibrous Organic Field Effect Transistor," *AUTEX Research Journal,* vol. 14, no. 3, pp. 152-160, 2014, doi: 10.2478/aut-2014-0012.

[195] M.-G. Huangfu *et al.*, "Preparation and Thermal Evaluation of Novel Polyimide Protective Coatings for Quartz Capillary Chromatographic Columns Operated over 320 °C for High-Temperature Gas Chromatography Analysis," *Polymers,* vol. 11, no. 6, p. 946, 2019, doi: 10.3390/polym11060946.

[196] A. K. Riau *et al.*, "Functionalization of the Polymeric Surface with Bioceramic Nanoparticles Via a Novel, Nonthermal Dip Coating Method," *ACS applied materials & interfaces,* vol. 8, no. 51, pp. 35565-35577, 2016, doi: 10.1021/acsami.6b12371.

[197] F. Ben Dhieb, S. H. Tabatabaei, F. Mighri, and A. Ajji, "Comparison of Crosslinking Efficiency in Dip and Roll-Deposited Coatings on Their Oxygen Barrier," *ACS omega,* vol. 4, no. 14, pp. 15772-15779, 2019, doi: 10.1021/acsomega.9b00950.

[198] B. Levich and L. Landau, "Dragging of a Liquid by a Moving Plate," *Acta Physicochim. URSS,* vol. 17, p. 42, 1942.

[199] L. Bromberg, M. Takayasu, P. Michael, J. V. Minervini, and A. Dietz, "Current Distribution and Re-Distribution in Hts Cables Made from 2nd Generation Tapes," *AIP Conference Proceedings,* vol. 1434, no. 1, pp. 1001-1008, 2012, doi: 10.1063/1.4707018.

[200] H. Dodiuk and S. H. Goodman, *Handbook of Thermoset Plastics*, Third edition. ed. (Pdl Handbook Series). San Diego: William Andrew, 2014.

[201] J. X. Tang, "Measurements of Fluid Viscosity Using a Miniature Ball Drop Device," *Review of Scientific Instruments,* vol. 87, no. 5, p. 054301, 2016, doi: 10.1063/1.4948314.

[202] "Measuring and Understanding Force Distance Curves," AFM Workshop, 2022.

[203] J. L. Tedesco, J. E. Rowe, and R. J. Nemanich, "Conducting Atomic Force Microscopy Studies of Nanoscale Cobalt Silicide Schottky Barriers on Si(111) and Si(100)," *Journal of applied physics,* vol. 105, no. 8, pp. 083721-083721-7, 2009, doi: 10.1063/1.3100212.

[204] J. K. Nelson and Y. Hu, "Nanocomposite Dielectrics—Properties and Implications," *Journal of physics. D, Applied physics,* vol. 38, no. 2, pp. 213-222, 2005, doi: 10.1088/0022-3727/38/2/005.

[205] N. Fuse, Y. Ohki, M. Kozako, and T. Tanaka, "Possible Mechanisms of Superior Resistance of Polyamide Nanocomposites to Partial Discharges and Plasmas," *IEEE transactions on dielectrics and electrical insulation,* vol. 15, no. 1, pp. 161-169, 2008, doi: 10.1109/T-DEI.2008.4446747.

[206] B. Koohbor, S. Ravindran, and A. Kidane, "Experimental Determination of Representative Volume Element (Rve) Size in Woven Composites," *Optics and lasers in engineering,* vol. 90, pp. 59-71, 2017.

[207] W. N. Sharpe Jr, J. Pulskamp, D. S. Gianola, C. Eberl, R. G. Polcawich, and R. J. Thompson, "Strain Measurements of Silicon Dioxide Microspecimens by Digital Imaging Processing," *Experimental mechanics,* vol. 47, no. 5, pp. 649-658, 2007, doi: 10.1007/s11340-006-9010-z.

Appendix A

2D Digital Image Correlation (DIC) Study of Tensile Testing Fixture

To further demonstrate the viability of the tensile test frame for experimental characterization of thin films and to validate the FE results, image correlation analyses were performed. As a first step, the strain noise floor associated with the utilized DIC analyses was first characterized using the approach presented in [206]. As such, the strain noise floor associated with the utilized DIC parameters were characterized by considering the spatial standard deviation of a series of static images acquired in a strain-free condition. In these analyses, a strain filter size of 9 was used and the mean strain noise floor is determined as 215 $\mu\epsilon$.

DIC analyses were performed to study the full-field deformation response of the fixture at room temperature conditions and to check for slippage at the top sample grip. The objective is to confirm that the proposed apparatus experiences negligible slip or local bending while testing is being conducted. The comparatively low modulus of the Kapton tape (~1.8 GPa) compared to the stainless steel (~215 GPa) indicates that the deflections of the fixture should have an insignificant effect on the properties of the material of interest, tested via the proposed custom fixture. The latter was justified through the full-field measurement of strain developed in the frame during mechanical tests at room temperature. Contours from image correlation analyses of the main test fixture are presented in Figure A1. The results show that the transverse strain is dominant in the fixture, with a peak at the top of the frame. Similarly, it is observed that small strain accumulation in the axial direction is present at the top inner edges of the fixture.

In all strain components, small islands of observable strain are present throughout the contour maps, showing that small deformations may be present. This is reasonable as some small motions are to be expected. Experimentally recorded strains are largely negligible, excluding the bands at the top edges of the fixture, which are greater than 0.001. The variation, in terms of large differences in order of magnitude, is consistent with the results of the finite element analyses presented in Appendix B.]

Figure A1

2D DIC Analysis of Tensile Testing Fixture

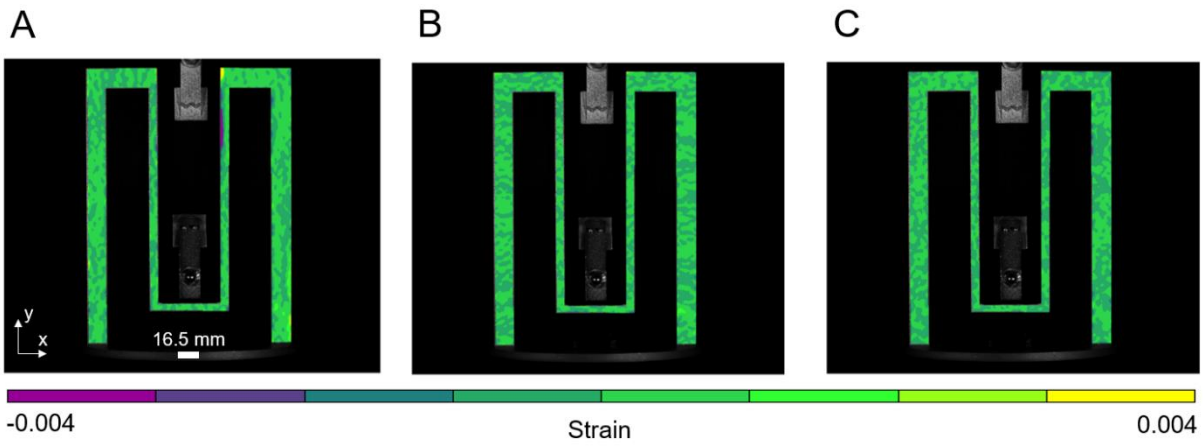

Note. 2D DIC analysis of the main fixture at room temperature with (A) transverse strain, ϵ_{xx}, (B) axial strain, ϵ_{yy}, and (C) shear strain, ϵ_{xy}. All images are obtained at a sample strain of ~0.4, i.e., near the failure strain of the sample.

DIC analyses are also performed on the top gripper as previously shown in Figure 17A. While no discernable slippage is present on the bottom portion of the apparatus in

room temperature conditions, it is important to also characterize slippage at the top. Slippage can either occur in the form of the fixture slipping from the wedge grip on the load frame, or by a sudden change in displacement where the sample may slip from the grips. In either case, the measured load curve is expected to show a sudden drop, indicative of a partial unloading occurred in response to the slippage. In addition, in the event of a slippage from the wedge grip, the top fixture is also expected to show displacement anomalies, observable through DIC measurements.

Figure A2 shows a comparison of the two simultaneously measured displacements for all room temperature tests. We observe that the displacements measured by both contact (via load frame measurement) and noncontact (via DIC) methods are highly correlated, and the results indicate that any slip from the top grip is negligible.

Figure A2

Comparison of Measured Displacements During Tensile Testing

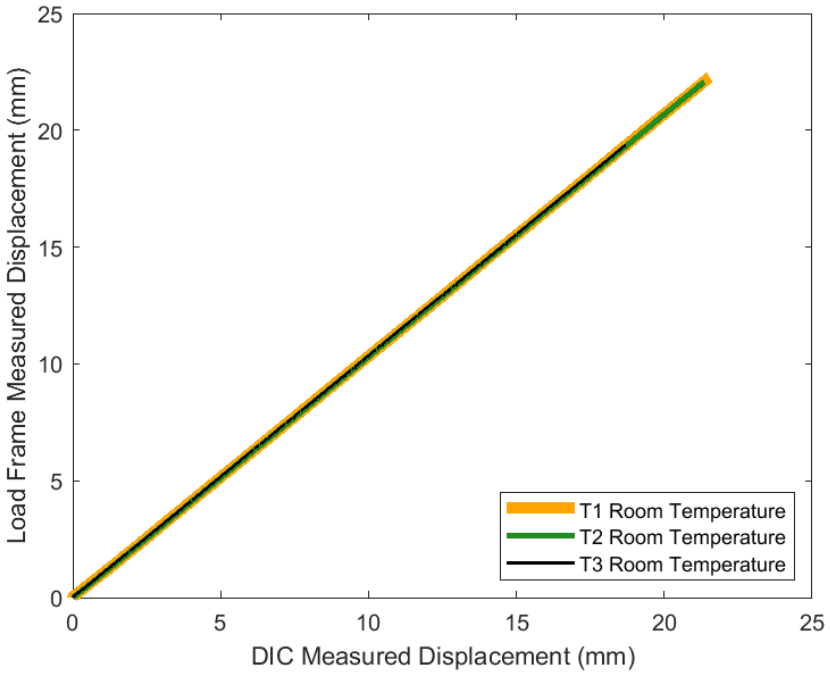

Note. Comparison of crosshead displacement measured by both the contact load frame and noncontact 2D DIC methods.

Appendix B

Finite Element Analysis of Tensile Testing Fixture

To quantify the limits of the proposed tensile testing apparatus, finite element models were constructed using the static structural module in ANSYS™ workbench from the assembly shown in Figure 17. Environmental temperature and elastic modulus of the sample are varied to identify expected stiffness and temperature pairs at which the apparatus should be modified for mechanical testing. It is assumed that the fixture will not slip at the grips of the load frame and apply fixed boundary conditions at its base. It is also assumed that all parts in the assembly are perfectly joined (i.e., no slip from fasteners). A displacement boundary condition is used for all simulations. The displacement boundary is determined from the examined material's mechanical response, as discussed in detail in the following sections. Therefore, the simulations aim to provide insight into the role of material stiffness and temperature on the apparatus strain, establishing limitations for testing of materials with higher yield points or ultimate tensile strength. Temperature is varied from -200 ℃ to 25 ℃ and elastic modulus is varied from 0.1 to 25 GPa. The model is constructed with 63,420 elements and 17,116 nodes, with a hex dominant mesh. The displacement condition is chosen for the subzero temperature tests because it is a good indicator of the compliance of the frame for the experimental data.

Figure B1

Finite Element Analysis of Tensile Testing Fixture

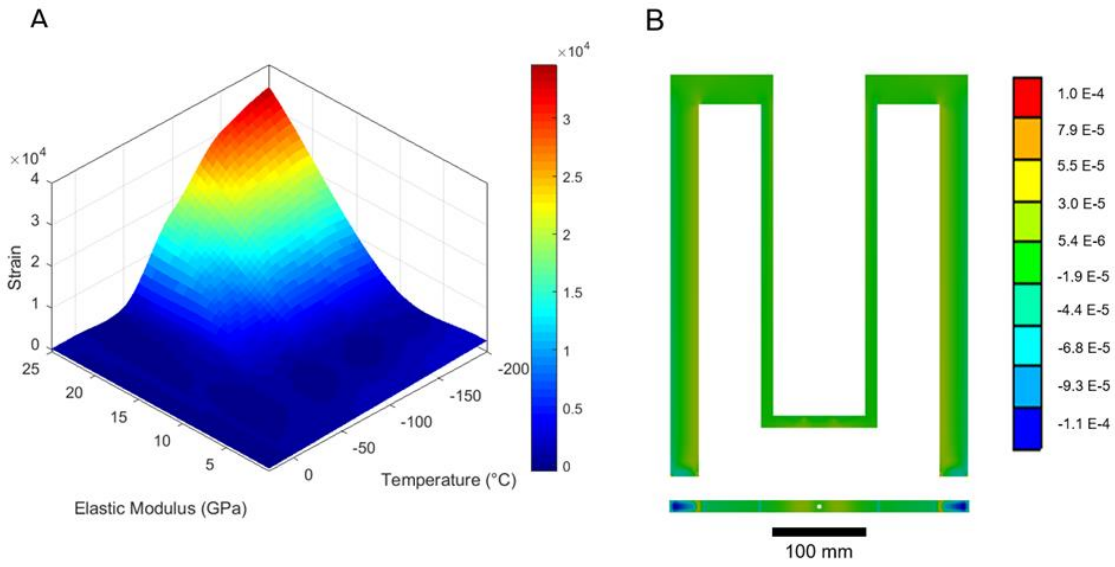

Note. Finite element analysis to determine the maximum operating characteristics of the developed apparatus. (A) Contour map showing maximum frame strain (axial strain, ϵ_{yy}) as a function of elastic modulus and temperature. (B) FE simulation results of the equivalent strain for the room temperature test for a sample with an elastic modulus of 1.8 GPa (i.e., the polymer used in this work) showing a front and bottom view of the apparatus.

Figure B1 shows that thin polymeric films are well suited for use in this test apparatus due to the negligible strains in the fixture during the test. It is shown that samples with a lower elastic modulus tested at higher temperatures have an insignificant effect on the fixture deformation while stiffer samples tested in cryogenic conditions lead

to larger strains. Furthermore, based on the results obtained herein, the test fixture is unlikely to experience yielding, and is thus, useful for repeated testing of polymer thin films over the range of the temperature-stiffness highlighted in the figure. To be specific, the tensile yield stress and the elastic modulus for 304 stainless steel are ~215 MPa and ~200 GPa, respectively. Simplified calculations using the Hooke's law estimate that the frame would yield at an axial strain of ~0.001. Upon examining Figure B1 it is observed that the maximum strain developed in the frame (achieved at the extreme conditions of T=-200 °C and E=25 GPa) is at least one order of magnitude lower than the yielding threshold for the full temperature range (25 to -200 °C), ensuring that the frame remains plastically undeformed, and thus, reusable for multiple tests.

Results for the axial strain subject to room temperature conditions with the experimentally determined elastic modulus are also presented in Figure B1. Maximum strains are developed at the grip and where the frame is fixed to the tensile tester. Frame stresses are well below the yield stress of 304 stainless steel, as also discussed earlier. In addition, the maximum frame strain (~0.0001) is orders of magnitude lower than the sample strain (~0.1) in the axial direction at this time step.

Appendix C

Rule of Mixtures Estimate of Elastic Modulus for Nanocomposite

The value of elastic modulus for the SiO_2 nanoparticle reinforcement was obtained from [207] and the experimentally measured elastic modulus for neat polyamide was used for this calculation. The calculation in Appendix D was used to determine the volume fractions of silica and polymer at the 6 wt. % concentration.

$$E_c = E_m \Phi_m + E_f \Phi_f \quad (2)$$

where:

$E_c =$ Elastic modulus of nanocomposite, MPa

$E_m , E_f =$ Elastic moduli of matrix and filler, MPa

$\Phi_m , \Phi_f =$ Volume fractions of matrix and filler

The SiO2 elastic modulus = 57 GPa, the polyamide elastic modulus = 1839 MPa, the volume fraction of SiO2 = 0.0268, and the volume fraction of polyamide = 0.9732.

$$E_c = (1839\ MPa)(0.9732) + (57{,}000\ MPa)(0.0268)$$

$$E_c = 3317\ MPa$$

Appendix D

Estimating the Number and Interfacial Volume of Nanoparticles by Concentration

Converting weight fraction to volume fraction in the nanocomposite:

SiO_2 density = 2.648 g/cm^3, PA6 density = 1.14 g/cm^3, V_{model} = 20 μm^3

$$V_{f\ SiO_2} = \frac{W_{f\ SiO_2}}{W_{f\ SiO_2} + (1 - W_{f\ SiO_2})(\frac{\rho_{SiO_2}}{\rho_{PA6}})} = \frac{0.06}{0.06 + (1 - 0.06)(\frac{2.648\ \mathrm{g}/cm^3}{1.14\ \mathrm{g}/cm^3})} = 0.0268$$

Calculating the # of particles and interfacial volume:

$$V\ SiO_2\ for\ 6\ wt.\% = (V_{f\ SiO_2})(V_{model}) = (0.0268)(2 \times 10^{-11} cm^3)$$

$$= 5.36 \times 10^{-13} cm^3$$

$V\ particle = \frac{4}{3}\pi(62.5 \times 10^{-7} cm)^3 = 1.023 \times 10^{-15} cm^3$ (Assumes 125 nm dia.)

$$\#\ particles\ in\ 20\mu m^3 = \frac{5.36 \times 10^{-13} cm^3}{1.023 \times 10^{-15} cm^3} = 524\ particles$$

Assuming a 40 nm interfacial region radial thickness:

$$Single\ particle + interface\ volume = \frac{4}{3}\pi(102.5 \times 10^{-7} cm)^3 = 4.511 \times 10^{-15} cm^3$$

$$Total\ particle + interface\ volume = (4.511 \times 10^{-14} cm^3) \times\ 524$$

$$=\ 2.36 \times 10^{-12} cm^3$$

$$Ratio\ to\ total\ model\ volume = 11.8\ \%$$

This calculation was then repeated for the 2 and 4 wt. % nanoparticle loadings.

Appendix E

Calculation of Conductive Heat Loads on Cryogenic Dielectric Test Chamber

Equation 2 is used to determine conductive heat load, a function of cross-sectional area, length, and material thermal conductivity, was calculated using Equation 2 for various connections [169]. The integrals of thermal conductivity over the operational temperature gradient of the environment test chamber were determined by plotting experimental values from [73] and estimating the resulting area graphically.

$$H = \frac{A}{L}\int_{T_1}^{T_2} k\, dt \tag{3}$$

where:

$H =$ conductive heat load (W)

$A =$ cross sectional area of the conducting element, cm^2

$L =$ length of the conducting element, cm

$k =$ thermal conductivity, W/cm K

$T_1 =$ the colder temperature, K

$T_2 =$ the warmer temperature, K

Heat load due to 3, 3.0 inch long × 1.0 inch diameter G10 fiberglass supports in warp direction:

$$H = \frac{5.06\ cm^2}{7.62\ cm}\int_{40}^{300} 0.0004x^{0.5491}\, dx$$

$$H = 1.127\ W\ per\ support\ \times 3 = 3.381\ W$$

Heat load due to 17, 24 inch long, 18 AWG copper wires:

$$H = \frac{0.00813\ cm^2}{60.96\ cm} \int_{40}^{300} 774.42x^{-1.007}\ dx$$

$$H = 0.201\ W\ per\ wire\ \times 17 = 3.42\ W$$

Heat load due to 2, 304 stainless steel bayonet connectors:

$$H = \frac{6.451\ cm^2}{12.70\ cm} \int_{40}^{300} -0.000002x^2 + 0.001x + 0.0024\ dx$$

$$H = 11.37\ W\ per\ bayonet\ connection\ \times 4 = 45.48\ W$$

Appendix F

Pressure Vessel Design Calculations

This calculation determined the hoop and longitudinal stresses in the chamber wall, as well as the average shear stress along the gas tungsten arc welds (GTAW) for the flat end plates, based on the dimensions in Figure F1.

Figure F1

Free-body Diagram of Pressure Vessel End Plate

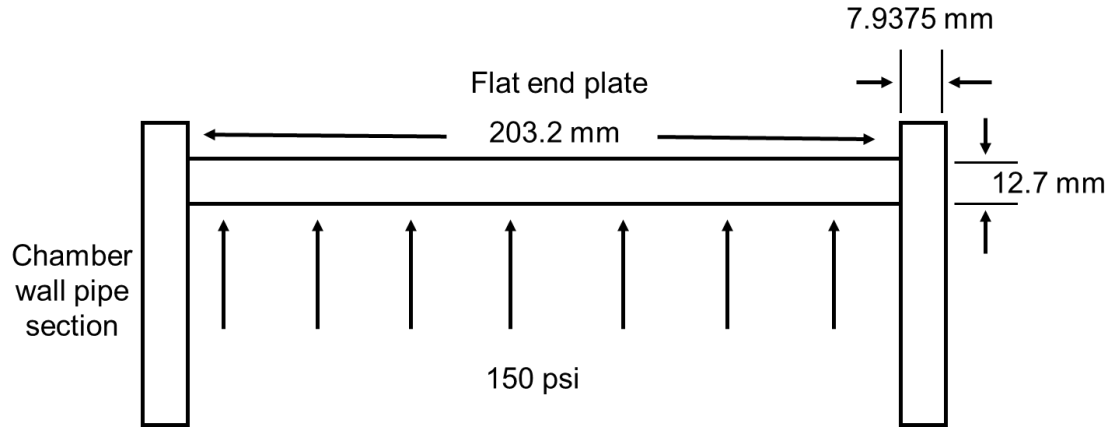

Note. Cross section drawing of cryogenic pressure vessel endplate.

Calculating average shear stress, $\tau_{average}$, along end plate weldment:

$$Endplate\ dia. = 203.2\ mm, Endplate\ area = 0.324\ m^2$$

$$Shear\ surface\ area\ of\ weld = 2\pi\ (Endplate\ radius)(Endplate\ thickness)$$

$$= 2\pi\left(\frac{0.2032\ m}{2}\right)(0.0127m) = 0.00811m^2$$

$$Longitudinal\ F = P \times A = (1034.21\ kPA)(0.324\ m^2) = 335.08\ kN$$

$$F_{average} = \tau_{average} \times Shear\ surface\ area\ of\ weld$$

$$\sum Fy = 0, \qquad P - F_{average} = 0$$

$$\therefore\ 335.08\ kN - \left(\tau_{average}(0.00811m^2)\right) = 0$$

$$\tau_{average} = 41.3\ MPa$$

Circumferential (hoop) stress in wall:

$$\sigma_1 = \frac{P \times r}{wall\ thickness} = \frac{(1034.21\ kPa)(\frac{0.2032\ m}{2})}{0.0079375\ m} = 13.24\ MPa$$

Longitudinal stress in wall:

$$\sigma_2 = \frac{P \times r}{2(wall\ thickness)} = \frac{(1034.21\ kPa)(\frac{0.2032\ m}{2})}{2(0.0079375\ m)} = 6.62\ MPa$$

Appendix G

Calculating Breakdown Voltage of the Fluid Medium in Dielectric Tests

This calculation determined the breakdown voltages of ambient air (nitrogen) and 100 psi helium to justify the improved dielectric performance of the nanocomposite in the helium tests. The data in Figure G1 was selected from [164].

Figure G1

Paschen's Curve for Dielectric Breakdown of Nitrogen and Helium Gases

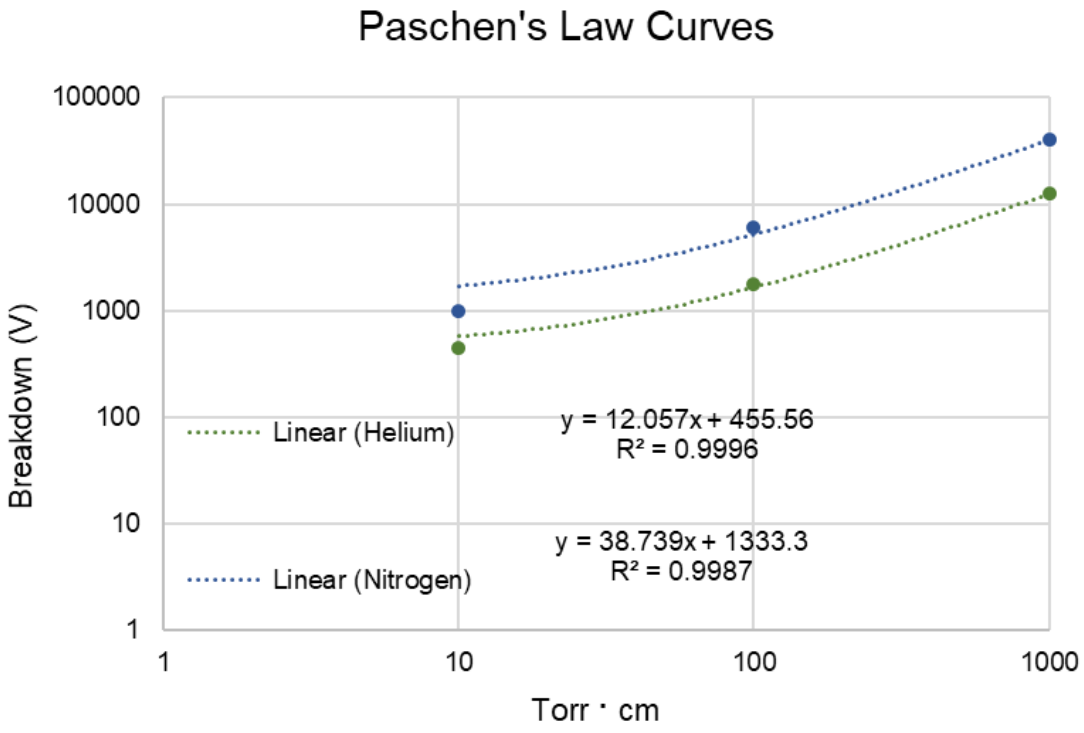

Assuming electrodes are spaced 1 cm apart:

$$torr \cdot cm_{\ Helium} = 5171\ torr\ (1\ cm), \qquad torr\ \cdot cm_{\ Nitrogen} = 760\ torr\ (1\ cm)$$

Based on the best fit curves that were generated from [164]:

$$BDV_{Helium} = 12.057(5171\ torr \cdot cm) + 455.56 = 62.35\ kV$$

$$BDV_{Nitrogen} = 38.739(760\ torr \cdot cm) + 1333.3 = 30.77\ kV$$